

# POLITECNICO DI TORINO

Corso di Laurea Magistrale

in Ingegneria Aerospaziale

Tesi di Laurea Magistrale

## **Air segment guidance and control for the Bi-Modal Unmanned Underwater/Air System**



Relatore/i  
prof. Battipede Manuela  
prof. Marzocca Piergiovanni

Candidato  
Tito Tomassi

Anno Accademico 2018/2019





# Table of Contents

<b>Table of Contents</b> .....	i
<b>List of Figures</b> .....	iii
<b>List of Tables</b> .....	vi
<b>List of Abbreviations</b> .....	vii
<b>List of Symbols</b> .....	viii
<b>Chapter 1: Introduction</b> .....	1
<b>Chapter 2: Bi-Modal Unmanned Underwater/Air System</b> .....	2
2.1 Bi-Modal Unmanned Underwater/Air System overview .....	2
2.2 BUUAS Aerodynamic.....	5
2.3 Longitudinal Dynamic.....	6
2.4 Lateral Directional Dynamic .....	9
2.5 Thrust and Torque .....	14
<b>Chapter 3: Simulator Implementation</b> .....	15
3.1 Flight Dynamics and Control toolbox .....	15
3.2 Dimensions, Weights and Inertia.....	16
3.3 Aerodynamic Model.....	17
3.4 Propulsion System Model.....	22
3.5 Trimmed Flight Condition.....	23
3.6 Model Validation.....	26
<b>Chapter 4: Autopilot</b> .....	28
4.1 Flying Qualities .....	28
4.2 Actuator .....	31
4.3 Motor Dynamic .....	31
4.4 Roll Attitude Hold (RAH).....	32
4.5 Pitch Attitude Hold (PAH) .....	34
4.6 Non-Linear Simulation.....	35
4.7 Altitude Hold/Altitude Select .....	40
4.8 IAS Hold.....	43
4.9 Heading Angle Hold System .....	44
<b>Chapter 5: Tail Issue</b> .....	46
5.1 Geometric Derivatives.....	46
5.2 Wind Tunnel Test.....	49

5.3	Results of the Wind Tunnel Test .....	51
<b>Chapter 6:</b>	<b>Deploying of wings.....</b>	<b>55</b>
6.1	Dynamic of Deploying .....	55
<b>Chapter 7:</b>	<b>Results of Simulation for different aerodynamic model .....</b>	<b>63</b>
7.1	New aerodynamic model.....	63
7.2	Results RAH Autopilots .....	67
7.3	Results PAH Autopilot .....	68
7.4	Flight Control-Waypoint-Results .....	69
7.4.1	Wind Simulation.....	70
7.5	Sensor .....	71
7.5.1	Inertial Measurement Unit.....	71
7.5.2	Global Position System .....	72
7.6	Waypoint Definition.....	73
7.6.1	Waypoint Switch .....	74
7.7	Autopilot Switch.....	75
7.8	Guidance Control.....	76
7.9	Results .....	77
<b>Chapter 8:</b>	<b>Conclusion and Future Work.....</b>	<b>81</b>
<b>References</b>	<b>.....</b>	<b>84</b>
<b>Appendices</b>	<b>.....</b>	<b>87</b>

# List of Figures

Figure 2.1-1: BUUAS Mission Profile representation .....	2
Figure 2.1-2: Deploying of the wing .....	3
Figure 2.1-3: Hybrid propeller configuration .....	3
Figure 2.1-4: Propulsion system integration.....	4
Figure 2.2-1 Lift, Drag and Pitch Moment coefficients .....	5
Figure 2.2-2 Side Force, Yaw and Roll Moment coefficients .....	5
Figure 2.3-1: Root Loci Longitudinal Dynamic.....	9
Figure 2.4-1 Root Loci Lateral Directional Dynamic .....	13
Figure 2.5-1 Rotor Thrust for different RPM .....	14
Figure 2.5-2 Rotor Torque for different RPM.....	14
Figure 3.1-1 Folder FDC toolbox .....	15
Figure 3.2-1 Geometric Dimension of BUUAS .....	16
Figure 3.3-1 X-Force wind tunnel result and approximation .....	17
Figure 3.3-2 Y-Force wind tunnel result and approximation .....	18
Figure 3.3-3 Z-Force wind tunnel result and approximation.....	18
Figure 3.3-4:Yaw Moment wind tunnel result and approximation .....	18
Figure 3.3-5 Roll Moment wind tunnel and approximation .....	19
Figure 3.3-6 Pitch Moment wind tunnel results and approximation .....	19
Figure 3.3-7 Wind tunnel (black lines) and Simulator (red lines) Reference system.....	20
Figure 3.4-1 Thrust experimental results and approximation.....	22
Figure 3.4-2 Torque experimental results and approximation.....	22
Figure 3.5-1 Simulink Model BUUAS Dynamic .....	24
Figure 3.5-2 Trimmed Condition: Angle of attack.....	24
Figure 3.5-3 Trimmed Condition: Side Slip Angle .....	24
Figure 3.5-4 Trimmed Condition: Angular Velocity $p$ .....	25
Figure 3.5-5: Trimmed Condition: Angular Velocity $q$ .....	25
Figure 3.5-6: Trimmed Condition: Angular Velocity $r$ .....	25
Figure 3.5-7 Trimmed Condition: Bank Angle .....	25
Figure 3.5-8: Trimmed Condition: Yaw Angle .....	25
Figure 3.5-9 Trimmed Condition: Pitch Angle .....	25
Figure 3.6-1 Root Loci Longitudinal dynamic: Wind tunnel and Simulator dynamic.....	26

Figure 3.6-2 Root Loci Lateral-Directional dynamic: Wind tunnel and Simulator dynamic .....	27
Figure 4.1-1: PID controller representation.....	30
Figure 4.3-1: Scheme of Rotor .....	32
Figure 4.4-1: Model of the Roll Attitude Hold.....	32
Figure 4.4-2: Roll Attitude Hold: input (t = 5 sec) and response of the system .....	33
Figure 4.4-3: Roll Attitude Hold: input (t = 2,5 sec) and response of the system .....	33
Figure 4.5-1: Pitch Attitude Hold: scheme of autopilot .....	34
Figure 4.5-2 Pitch Attitude Hold: input and response .....	35
Figure 4.6-1: PAH and RAH model .....	36
Figure 4.6-2: Trim Condition: results comparison between simulation with(right) and without(left) autopilots .....	38
Figure 4.6-3: Non-linear simulation: Roll velocity response .....	39
Figure 4.6-4: Non-linear simulation: Theta response .....	39
Figure 4.7-1: Altitude Hold's Simulink scheme.....	40
Figure 4.7-2: Altitude Hold response .....	41
Figure 4.7-3: Altitude Select's Simulink scheme.....	42
Figure 4.7-4: Altitude Select response .....	42
Figure 4.8-1: Speed Hold's Simulink scheme.....	43
Figure 4.8-2: Speed Hold results .....	44
Figure 4.9-1: Heading Hold System's Simulink scheme .....	44
Figure 4.9-2: Heading Angle Hold response: $\psi$ .....	45
Figure 4.9-3: Heading Angle Hold: $\phi$ .....	45
Figure 5.1-1: Lateral Force on the Horizontal Tail of the F-4 associated with $\beta$ .....	46
Figure 5.1-2: dihedral Effect for the Vertical Tail.....	47
Figure 5.2-1: Wind Tunnel set up.....	49
Figure 5.2-2: Detail of Wind tunnel set up .....	49
Figure 5.2-3: Wind tunnel set up: cylinder insede the fuselage .....	50
Figure 5.3-1: Distribution and Approximation of $Cl$ for different Equilibrator's angles .....	51
Figure 5.3-2: Distribution and Approximation of $CN$ for different Equilibrator's angles .....	51
Figure 5.3-3: Distribution and Approximation of $CY$ for different Equilibrator's angles .....	52
Figure 5.3-4: Distribution and Approximation of $Cl\beta$ for different Equilibrator's angles.....	53
Figure 5.3-5: Distribution and Approximation of $CN\beta$ for different Equilibrator's angles .....	53
Figure 5.3-6: Distribution and Approximation of $CY\beta$ for different Equilibrator's angles.....	54
Figure 6.1-1: Root Loci Longitudinal dynamic for different sweep angle .....	55
Figure 6.1-2: Root Loci Lateral-Directional dynamic for different sweep angle .....	56

Figure 6.1-3: Simulink scheme to change dynamic for different sweep angle.....	57
Figure 6.1-4: Deploying of the wing: Angle of attack with and without autopilots.....	57
Figure 6.1-5: Deploying of the wing: Side Slip Angle with and without autopilots .....	58
Figure 6.1-6: Deploying of the wing: Altitude with and without autopilots .....	58
Figure 6.1-7: Deploying of the wing: Roll velocity with and without autopilots.....	58
Figure 6.1-8:Deploying of the wing: Pitch velocity with and without autopilots .....	59
Figure 6.1-9:Deploying of the wing: Yaw velocity with and without autopilots .....	59
Figure 6.1-10: Deploying of the wing: $\phi$ Angle with and without autopilots .....	59
Figure 6.1-11:Deploying of the wing: $\psi$ Angle with and without autopilots.....	60
Figure 6.1-12:Deploying of the wing: $\theta$ Angle with and without autopilots .....	60
Figure 6.1-13:Deploying of the wing: Simulation for different initial altitude .....	61
Figure 6.1-14: Deploying of the wing: Simulation for different initial velocity .....	62
Figure 7.1-1: Trimmed Condition: Comparison between Old(left) and New(right) aerodynamic model.....	65
Figure 7.1-2: Later-Directional root loci: comparison between results of different aerodynamic model .....	66
Figure 7.1-3: Detail of root loci for lateral directional motion.....	66
Figure 7.1-4: Longitudinal root loci: comparison between results of different aerodynamic model .....	67
Figure 7.2-1: Roll Attitude Hold: input (t = 2,5 sec) and response of the system: comparison two aerodynamic model.....	68
Figure 7.2-2: Roll Attitude Hold: input (t = 5 sec) and response of the system: comparison between two aerodynamic model.....	68
Figure 7.3-1: Pitch Attitude Hold input and response: comparison between two aerodynamic model.....	69
Figure 7.4-1: Simulink model of BUUAS' Simulator .....	70
Figure 7.4-2: Simulink model of wind profile take by FDC-toolbox.....	70
Figure 7.4-3: Inside wind profile mask .....	70
Figure 7.5-1: Simulink scheme of IMU took by Aerospace toolbox.....	71
Figure 7.5-2: Detail of IMU parameters: Accelerometer .....	72
Figure 7.5-3: Detail of IMU parameters: Gyroscope.....	72
Figure 7.5-4: Detail of IMU parameters: Noise.....	72
Figure 7.5-5: GPS' Simulink Model.....	73
Figure 7.6-1: Detail of callback button to chose Waypoints of trajectory.....	74
Figure 7.6-2: Detail of scheme for the switch of waypoint .....	74
Figure 7.7-1: Detail of autopilots' switch .....	75
Figure 7.9-1: Trajectory 2 3D graphics: details of waypoints .....	78
Figure 7.9-2: Trajectory example: comparison between two aerodynamic model.....	80
Figure 7.9-3: Trajectory 2: 3D graphics .....	80



# List of Tables

Table 2.3-1 Longitudinal derivaties coefficients .....	8
Table 2.4-1 Lateral-Directional derivaties coefficients .....	11
Table 3.2-1 Buuas: geometric dimension, weights and inertia.....	16
Table 3.3-1: Force coefficients .....	21
Table 3.3-2: Moment coefficients .....	21
Table 3.4-1: Rotor Coefficients .....	22
Table 3.5-1: Trimmed Condition.....	23
Table 3.6-1 Wind tunnel and Simulator eigenvalues.....	26
Table 3.6-2 Wind tunnel and Simulator eigenvalues.....	27
Table 4.1-1: Class, Category and Phase definition MIL-HDBK-1797.....	29
Table 4.2-1: Specification Aileron and Tail servo.....	31
Table 4.3-1: Gain values of Roll Attitude Hold .....	33
Table 4.4-1: Pitch Attitude Hold: Gain values .....	34
Table 4.5-1: Non-linear simulation: RAH and PAH gains.....	39
Table 4.6-1: Altitude Hold's gain .....	41
Table 4.6-2: Altitude Select gain.....	42
Table 4.7-1: Speed Hold gain .....	43
Table 4.8-1: Heading Angle Hold gain .....	45
Table 5.2-1: Velocity, Pitch Angle and Sweep Angle tested during the wind tunnel tests .....	50

# List of Abbreviations

BUUAS	Bi-modal Unmanned Underwater/Air System
IMU	Three-axis Inertial Measurement Unit
RPM	Revolution Per Minutes
FDC	Flight Dynamic and Control
PAH	Pitch Attitude Hold
RAH	Roll Attitude Hold
AS	Altitude Select
AH	Altitude Hold
GPS	Global Position System
CG	Center of Gravity
FMS	Flight Management System

# List of Symbols

$A$	Matrix of variables states
$b$	Wingspan [m]
$B$	Matrix of control
$C$	Matrix of outputs states
$C_{T_V}, C_{T_q}, C_{T_{\dot{\alpha}}}, C_{T_{\delta_e}}$	Thrust Force coefficients derivatives $\left(\frac{\delta C_T}{\delta_V}, \frac{\delta C_T}{\delta_q}, \frac{\delta C_T}{\delta_{\dot{\alpha}}}, \frac{\delta C_T}{\delta_{\delta_e}}\right)$
$C_{D_V}, C_{D_q}, C_{D_{\dot{\alpha}}}, C_{D_{\delta_e}}$	Drag Force coefficients derivatives $\left(\frac{\delta C_D}{\delta_V}, \frac{\delta C_D}{\delta_q}, \frac{\delta C_D}{\delta_{\dot{\alpha}}}, \frac{\delta C_D}{\delta_{\delta_e}}\right)$
$C_{L_V}, C_{L_q}, C_{L_{\dot{\alpha}}}, C_{L_{\delta_e}}$	Lift Force coefficients derivatives $\left(\frac{\delta C_L}{\delta_V}, \frac{\delta C_L}{\delta_q}, \frac{\delta C_L}{\delta_{\dot{\alpha}}}, \frac{\delta C_L}{\delta_{\delta_e}}\right)$
$C_{M_V}, C_{M_q}, C_{M_{\dot{\alpha}}}, C_{M_{\delta_e}}$	Pitch Moment coefficients derivatives $\left(\frac{\delta C_M}{\delta_V}, \frac{\delta C_M}{\delta_q}, \frac{\delta C_M}{\delta_{\dot{\alpha}}}, \frac{\delta C_M}{\delta_{\delta_e}}\right)$
$C_{l_{\beta}}, C_{l_p}, C_{l_r}, C_{l_{\delta_a}}, C_{l_{\delta_r}}$	Roll Moment coefficients derivatives $\left(\frac{\delta C_l}{\delta_{\beta}}, \frac{\delta C_l}{\delta_p}, \frac{\delta C_l}{\delta_r}, \frac{\delta C_l}{\delta_{\delta_a}}, \frac{\delta C_l}{\delta_{\delta_r}}\right)$
$C_{n_{\beta}}, C_{n_p}, C_{n_r}, C_{n_{\delta_a}}, C_{n_{\delta_r}}$	Yaw Moment coefficients derivatives $\left(\frac{\delta C_n}{\delta_{\beta}}, \frac{\delta C_n}{\delta_p}, \frac{\delta C_n}{\delta_r}, \frac{\delta C_n}{\delta_{\delta_a}}, \frac{\delta C_n}{\delta_{\delta_r}}\right)$
$C_{Y_{\beta}}, C_{Y_p}, C_{Y_r}, C_{Y_{\delta_a}}, C_{Y_{\delta_r}}$	Side Force coefficients derivatives $\left(\frac{\delta C_Y}{\delta_{\beta}}, \frac{\delta C_Y}{\delta_p}, \frac{\delta C_Y}{\delta_r}, \frac{\delta C_Y}{\delta_{\delta_a}}, \frac{\delta C_Y}{\delta_{\delta_r}}\right)$
$C_{L_{\alpha}}$	Lift coefficient slope
$C_{Leq}$	Lift coefficient for equilibrium-angle of attack
$C_{L0}$	Lift coefficient for zero-angle of attack
$c$	Mean cord wing [m]
$C_D$	Drag coefficient
$C_L$	Lift coefficient
$C_M$	Pitch Moment coefficient
$C_Y$	Side-Force coefficient
$C_l$	Roll Moment coefficient
$C_n$	Yaw Moment coefficient
$C_{L_{\alpha_t}}$	Tail lift-curve slope
$C_{Y\beta_H}$	
$C_{l\beta_H}$	
$\left(\frac{C_{l\beta}}{C_{L1}}\right)_{AR}$	contribution associated with the wing aspect ratio
$\frac{C_{l\beta}}{\Gamma_W}$	contribution associated with the wing dihedral angle
$\frac{\Delta C_{l\beta}}{\Gamma_W}$	correction factor associated with the size of the fuselage modeled
$K_{M_{\Lambda}}$	correction factor associated with the Mach number and the wing sweep angle
$K_f$	correction factor associated with the length of the forward portion of the fuselage
$K_{M_{\Gamma}}$	correction factor associated with the Mach number and the wing dihedral angle
$n$	Number of revolution of motor

$l_t$	Distance between CG and horizontal tail aerodynamic center [m]
$l_v$	Distance between CG and vertical tail aerodynamic center [m]
$I_{xx}, I_{yy}, I_{zz}$	Principal Inertial Moments
$I_{xy}, I_{xz}, I_{yz}$	Composed Inertial Moments
$d$	Distance between waypoint [km]
$\Gamma_H$	Anhedral angle of the tail
$S_H$	surface of the tail
$S_{ref}$	reference surface of the wing
$\frac{d\sigma}{d\beta}$	Down-wash factor
$\frac{d\epsilon}{d\alpha}$	Down-wash factor
$xinco$	Vector of initial condition of simulation variables
$xdot0$	Vector of initial derivatives condition of simulation variables
$uaero0$	Vector of initial condition of simulation deflection
$V_t$	
$x_{cg}$	Location of CG from nose [m]
$x_{ac_w}$	Location of aerodynamic center of the wing from nose [m]
$\tau$	Constant time [s]
$\tau_s$	Spiral Mode constant time [s]
$W$	Weight [kg]
$J$	Cost-function
$t_r$	Time to rise [s]
$M_p$	Peak of overshoot [%]
$TF_{rudder}$	Transfer function rudder's servo
$TF_{tail}$	Transfer function tail's servo
$TF_{ailero}$	Transfer function aileron's servo
$R$	Radius of Earth [km]
$\theta_{tr}$	Heading reference for the next waypoint [°]
$\theta$	Pitch angle [°]
$\psi$	Yaw angle [°]
$\phi$	Roll angle [°]
$M$	Mach number
$\delta_a$	Aileron deflection [°]
$\delta_e$	Equilibrator deflection [°]
$\delta_r$	Rudder deflection [°]
$(u, v, w)$	Scalar component of V in the $F_B$ [ $ms^{-1}$ ]
$\dot{x}$	States derivatives vector
$x$	States vector
$y$	Controlled variables vector
$u$	Control vector



# Chapter 1: Introduction

In the last twenty years the development of the Unmanned Aerial Vehicle (UAV) is increase thanks to the improve of technology. They are use more and more in different sectors. UAVs are very important in the military sector. They can carry out work of surveillance and reconnaissance safeguarding life of many soldiers, the project of Bi-modal unmanned underwater/air system (BUUAS) born with these purposes.

The Bi-modal unmanned Underwater/Air System (BUUAS) is a vehicle designed in the RMIT University and able to perform a particular Underwater/Airborne mission profile, with the purpose to carrying airborne surveillance mission with reduced exposure risk with respect to its submarine mothership. The vehicle assumes a dual aerodynamic configuration for the two different phases of the mission. In order to investigate the guidance and control characteristics of the vehicle, a simulator has been implemented. Particular attention has been given to the presence of the Y-tail configuration, featuring an anhedral angle, and to the water-to-air transition phase, where the wing is deployed by changing its sweep angle.

The FDC simulator structure is employed and correlated to data of the BUUAS vehicle and with two different aerodynamic models. The first one uses data of preliminary wind tunnel tests, performed on a previous BUUAS version. Further investigation and wind tunnel tests have been performed in order to obtain a second and more accurate aerodynamic model, where the influence of the tail on other volumes is taken into consideration. The simulator is tested for the two different aerodynamic models and for different trajectories. In order to investigate the dynamics of the wing deployment and to test the robustness of the control system during this phase, the simulation is run using six different intermediate aerodynamic models for the different weep angle ranges. Autopilots, necessary for the unmanned flight, are implemented and integrated in the simulator.

# Chapter 2: Bi-Modal Unmanned Underwater/Air System

## 2.1 Bi-Modal Unmanned Underwater/Air System overview

The Bi-modal unmanned underwater/air system (BUUAS) is an innovative vehicle built by a RMIT University student Dian Guo [1], for a very specific mission profile. The purpose of the vehicle is to carry airborne surveillance mission with reduced exposure risk of its submarine mothership. In the mission profile, the vehicle will cruise underwater to stay away from submarine, then it is launched out of water by the transition propulsion system and changed the water configuration to air configuration to carry its surveillance mission. After its airborne mission, it will dive into the water and cruise back to the submarine (Figure 2.1-1).

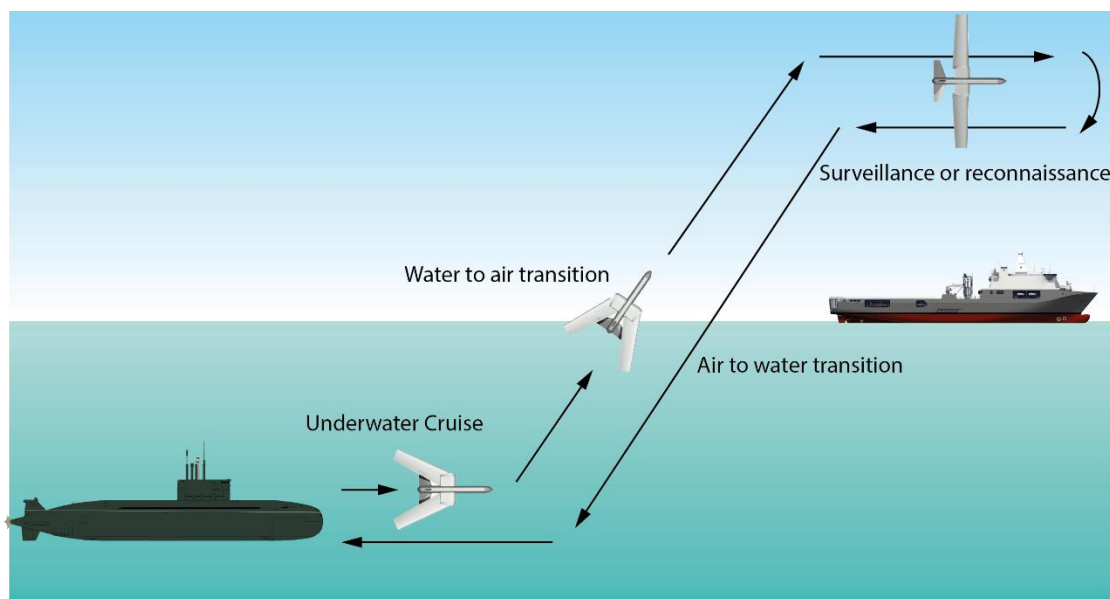


*Figure 2.1-1: BUUAS Mission Profile representation [1]*

The critical phase of the mission profile is the transition water/air and air/water. The innovative vehicle adopts the variable sweep wing configuration to compromise the different configuration design requirement for air (Figure 2.1-2: sweep angle  $0^\circ$ ) and water (Figure 2.1-2: sweep angle  $65^\circ$ ). Different sweep angles are driven by two linear actuators.

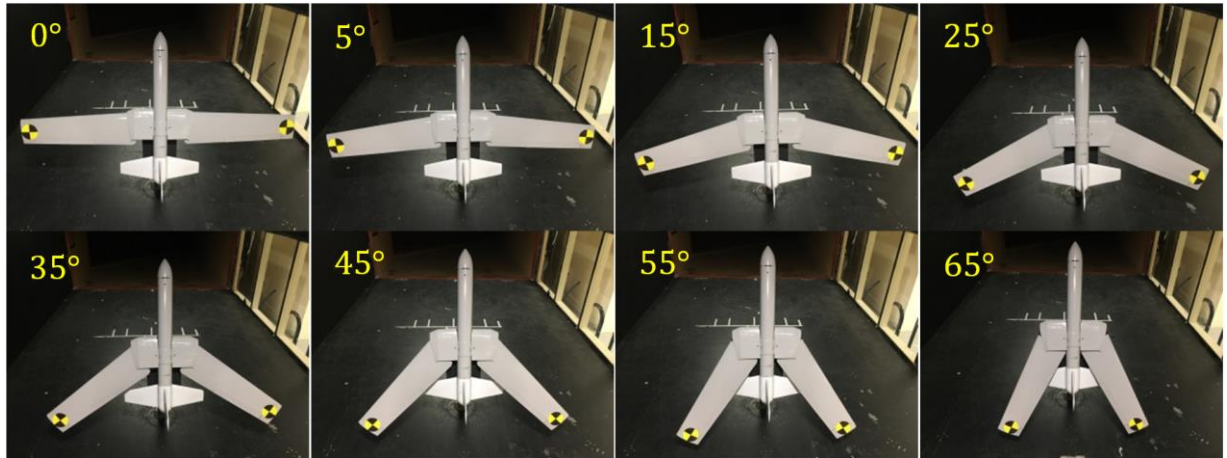


*Figure 2.1-2: Deploying of the wing [1]*

Further, a hybrid propulsion system is conceived for the BUUAS to realize the capability of cruising in air and water [2]. The hybrid propulsion system is composed by the transmission system and a hybrid propeller. As shown in Figure 2.1-3 the air and water propeller are connected by the middle hub that gives the possibility at the air propeller to be folded back by the pressure of air or water flow. This action avoids its damage during the transition phase and reduces the drag during the underwater cruise. With the rotation of the motor the propellers will spin fold outward to function as a normal air propeller thanks to the centrifugal and aerodynamic force.

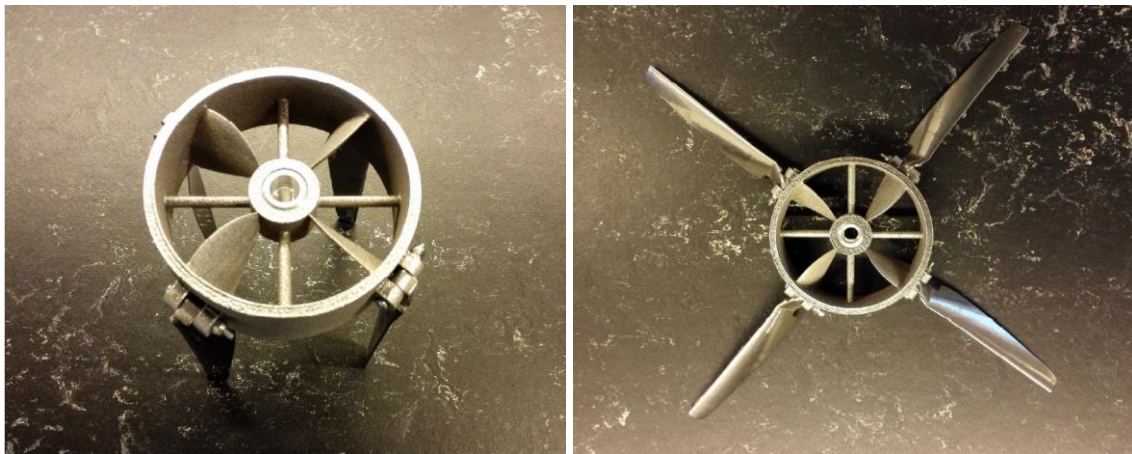


*Figure 2.1-3: Hybrid propeller configuration [1]*

To realize the water to air transition the BUUAS uses a water jet transition propulsion. The transition propulsion system employs high pressure gas from the CO<sub>2</sub> cartridge to expel the water out of chamber. This high velocity and mass flow rate fluid can produce significant thrust, which can easily propel the vehicle out of water like a rocket.



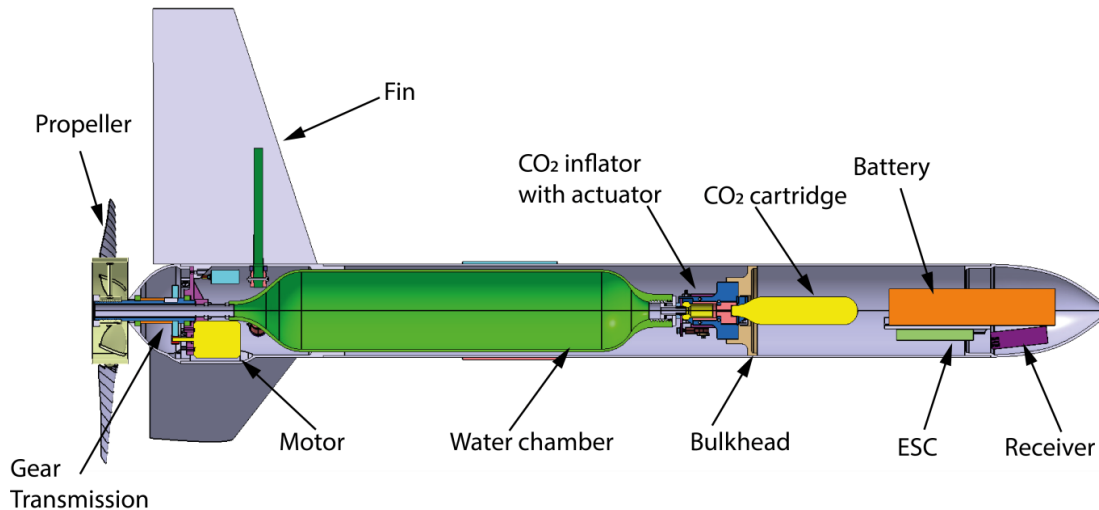


*Figure 2.1-4: Propulsion system integration [1]*

The goal of this research is to build a simulator to examine the dynamic of the vehicle. Particular attention will put on the air phase and on the deploying of the wing after the transition water to air.

As shown in Figure 1.1 the mission profile of BUUAS is composed of six main phases.

- 1) **CRUISE UNDERWATER:** After being released from the submarine, the first phase is cruise underwater. During this phase, the wing of the vehicle is fully stowed like the configuration 65° wing sweep (Figure 2.1-2). regarding to the propulsion, the vehicle uses a specific propeller designed for both the air and the water;
- 2) **TRANSITION WATER/AIR:** arrived at a necessary distance to be to sure that the position of submarine is not identified, the vehicle jumps out of the water whit a particular propulsion system that used pressurized gas to push out water from the water camber (Figure 2.1-3);
- 3) **CLIMB/SURVEILLANCE/DESCENT:** after deploying of wings there is a phase of climb in which the vehicle arrives at the right height to do surveillance or reconnaissance; at the end of this phase the vehicle starts a descendent;
- 4) **TANSITION AIR/WATER:** before going another time in the water the vehicle changes again configuration from number 6 to number 1, and it will try to have a correct path and velocity to be sure that the impact with the water doesn't destroy the vehicle;

- 5) CRUISE BACK: this is the last phase in which the BUUAS came back in the submarine after an underwater cruise.

## 2.2 BUUAS Aerodynamic

The aerodynamic of the vehicle was first obtained by a numerical simulation and then verified by wind tunnel test. The results are shown below.

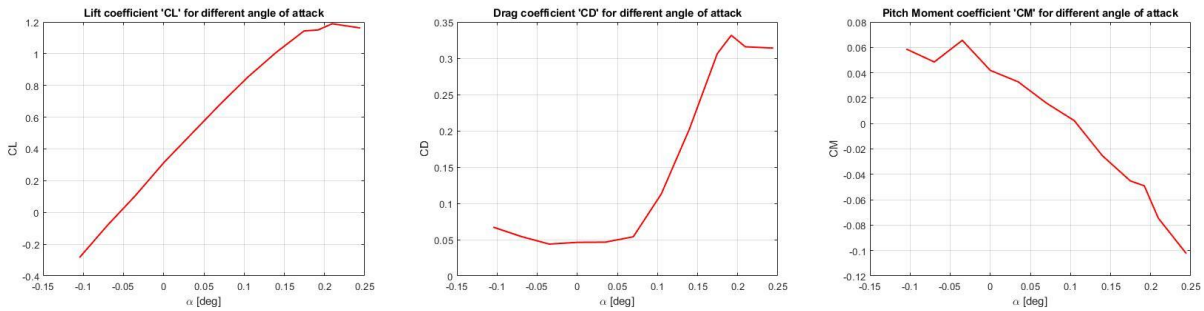


*Figure 2.2-1 Lift, Drag and Pitch Moment coefficients*

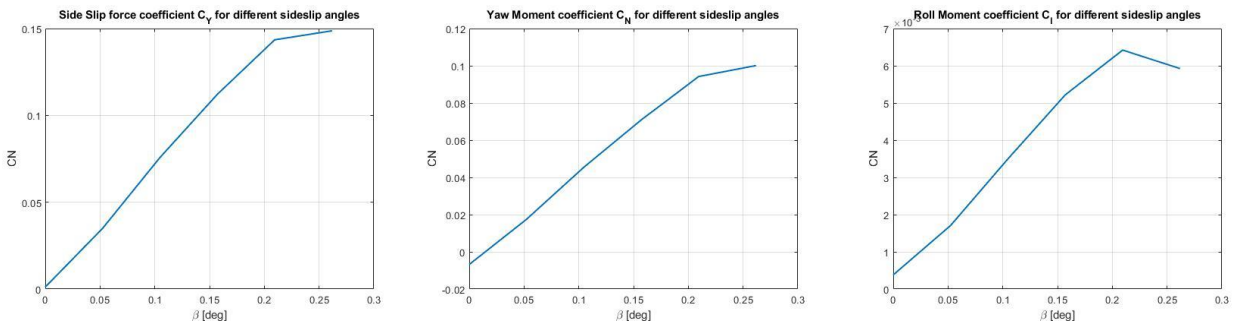


*Figure 2.2-2 Side Force, Yaw and Roll Moment coefficients*

From the wind tunnel results aerodynamic derivatives are obtained and employed to study the stability analysis of the vehicle. The analysis was done around the steady flight condition at for a velocity equal of  $V = 20 \text{ m/s}$ . With this consideration, the Taylor approximation of forces and moments could be considered linear and the dynamic equation can be linearized using the small disturbance theory. The usual separation between the longitudinal and lateral directional dynamic was done. Some static stability coefficients are not obtained by the results of the wind tunnel test, so the formulation reported by Nelson is followed.

### 2.3 Longitudinal Dynamic

Below is presented the system of kinematic and dynamic equations for the longitudinal motion (Eq. (1)).

$$\begin{aligned}
 \left(\frac{d}{dt} - X_u\right)\Delta u - X_w\Delta w + (g \cos\theta_0)\Delta\theta &= X_{\delta_e}\Delta\delta_e + X_{\delta_r}\Delta\delta_r \\
 -Z_u\Delta u + \left[(1 - Z_w)\frac{d}{dt} - Z_w\right]\Delta w - \left[(u_0 + Z_q)\frac{d}{dt} - g \sin\theta_0\right]\Delta\theta &= Z_{\delta_r}\Delta\delta_r + Z_{\delta_e}\Delta\delta_e \\
 -M_u\Delta u + \left(M_w\frac{d}{dt} + M_w\right)\Delta w + \left(\frac{d^2}{dt^2} - M_q\frac{d}{dt}\right)\Delta\theta &= M_{\delta_e}\Delta\delta_e + M_{\delta_r}\Delta\delta_r
 \end{aligned} \tag{1}$$

In the equation is possible to see that there are derivatives due to the change of velocity, pitching velocity, time rate of change of the angle of attack and angle of elevator. Bellow are presented the formula of this derivatives taken from the book of NELSON [3].

Derivatives due to the change of velocity (Eq. (2))

$$\begin{aligned}
 C_{T_v} &= -2 * C_{T_{eq}} \\
 C_{D_v} &= \frac{\delta C_D}{\delta V} \\
 C_{L_v} &= \frac{\delta C_L}{\delta V} \\
 C_{M_v} &= \frac{\delta C_M}{\delta V}
 \end{aligned} \tag{2}$$

The variation of coefficients of drag, lift and pitch moment is very small that be considered negligible.

Derivatives Due to the Pitching Velocity (Eq. (3))

$$\begin{aligned}
 C_{T_q} &= \frac{\delta C_T}{\delta q} \\
 C_{D_q} &= \frac{\delta C_D}{\delta q} \\
 C_{L_q} &= \frac{\delta C_L}{\delta q} = 2 C_{L_{\alpha_t}} V_t
 \end{aligned} \tag{3}$$

$$C_{Mq} = \frac{\delta C_M}{\delta q} = -2 C_{L\alpha_t} \frac{l_t}{c} V_t$$

In this case the derivatives of Thrust and Drag due to the change of the pitch velocity are considered negligible.

Derivatives due to the time rate of change of the angle of attack (Eq. (4))

$$\begin{aligned} C_{T\dot{\alpha}} &= \frac{\delta C_T}{\delta \dot{\alpha}} \\ C_{D\dot{\alpha}} &= \frac{\delta C_D}{\delta \dot{\alpha}} \\ C_{L\dot{\alpha}} &= \frac{\delta C_L}{\delta \dot{\alpha}} \\ C_{M\dot{\alpha}} &= \frac{\delta C_M}{\delta \dot{\alpha}} = -2 C_{L\alpha_t} V_t \frac{l_t}{c} \frac{\delta \epsilon}{\delta \alpha} \end{aligned} \quad (4)$$

The coefficients of Drag and Lift are considered negligible. As concern the Lift coefficient the variation of the Lift due to the change of the angle of attack is considered very small and without effects of hysteresis, so also this coefficient is considered negligible.

Derivatives due to the change of the angle of elevator (Eq. (5))

$$\begin{aligned} C_{T\delta_e} &= \frac{\delta C_T}{\delta \delta_e} \\ C_{D\delta_e} &= \frac{\delta C_D}{\delta \delta_e} \\ C_{L\delta_e} &= \frac{\delta C_L}{\delta \delta_e} = \frac{S_t}{S_{ref}} C_{L\alpha_t} \\ C_{M\delta_e} &= \frac{\delta C_M}{\delta \delta_e} = \frac{S_t}{S_{ref}} C_{L\alpha_t} (x_{cg} - x_{acw}) c - C_{L\alpha_t} V_{wt} \end{aligned} \quad (5)$$

In this case, also, the variation of the drag and thrust is considered negligible.

In Table 2.3-1 values of aerodynamic coefficients are presented:

	$\delta C_T$	$\delta C_D$	$\delta C_L$	$\delta C_M$
$\delta V$	-0,1018	0	0	0
$\delta q$	0	0	0	-2,6412
$\delta \dot{\alpha}$	0	0	0	-0,7705
$\delta d_e$	0	0	0,3984	-1,2794

Table 2.3-1 Longitudinal derivatives coefficients values

With these values of the coefficients a steady state matrix is building.

$$\begin{cases} \dot{x} = A x + B u \\ y = C x + D u \end{cases} \quad (6)$$

In which,  $x$  represents the state vector  $x = \{ V \ \alpha \ \theta \ q \}^T$ ,  $u$  the control vector,  $u = \{ d_e \ n \}^T$  and  $y$  the vector of controlled variables, in this case  $y = \{ \alpha \ \theta \ n \}^T$ . For this analysis a dimensional system is considered. In this condition the matrix A (matrix of state variables  $\mathbb{R}^{4 \times 4}$ ) is composed of the follow terms:

$a_{1,1} = \frac{1}{m} (T_v * \cos \alpha_t - D_v)$	$a_{1,2} = \frac{1}{m} (mg - D_\alpha - T_{eq} \sin \alpha_t)$	$a_{1,3} = -g$	$a_{1,4} = 0$
$a_{2,1} = \frac{L_v + T_v \sin \alpha_t}{m V + \dot{L}_\alpha}$	$a_{2,2} = \frac{L_\alpha + T_{eq} \cos \alpha_t}{m V + L_{\dot{\alpha}}}$	$a_{2,3} = 0$	$a_{2,4} = \frac{m V - L_q}{m V + L_{\dot{\alpha}}}$
$a_{3,1} = 0$	$a_{3,2} = 0$	$a_{3,3} = 0$	$a_{3,4} = 1$
$a_{4,1} = \frac{1}{I_{yy}} \frac{M_v - M_{\dot{\alpha}}(L_v + T_v \sin \alpha_t)}{m V + L_{\dot{\alpha}}}$	$a_{4,2} = \frac{1}{I_{yy}} \frac{M_\alpha - M_{\dot{\alpha}}(L_\alpha + T_{eq} \cos \alpha_t)}{m V + L_{\dot{\alpha}}}$	$a_{4,3} = 0$	$a_{4,4} = \frac{1}{I_{yy}} \frac{M_q - M_{\dot{\alpha}}(m V - L_q)}{m V + L_{\dot{\alpha}}}$

Table 2.3-2: Detail of matrix of state variables for longitudinal dynamic

Results found are presents in the Figure 2.3-1 in which it is possible to see eigenvalues represent on the root loci graphic. Both, Phugoid and Short Period, are stable but, the imaginary part of short period is very high that means that the mode of the short period will be very dampened.

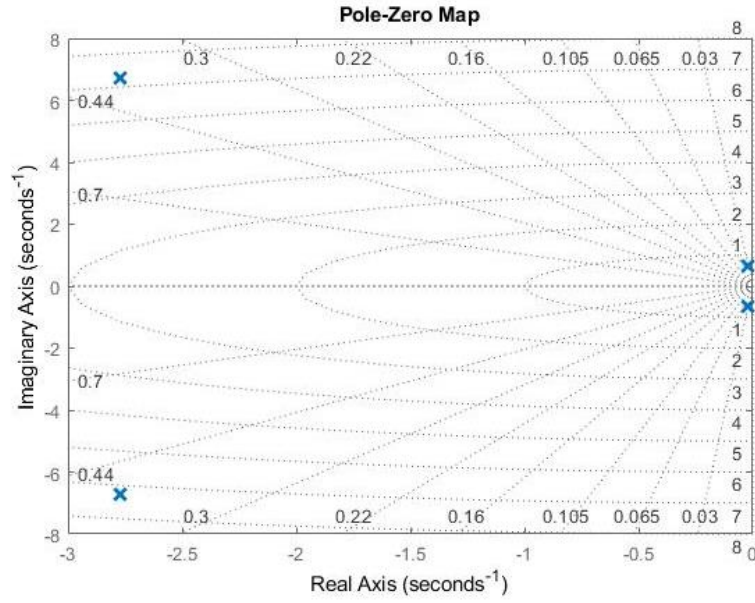


Figure 2.3-1: Root Loci Longitudinal Dynamic

$$\lambda_{1,2} = -2,7727 \pm i 6,70$$

$$\lambda_{3,4} = -0,021 \pm i 0,6677 \quad (7)$$

## 2.4 Lateral Directional Dynamic

Below is presented the system of kinematic and dynamic equations for the lateral directional motion (Eq. (8)).

$$\begin{aligned} \left(\frac{d}{dt} - Y_v\right)\Delta v - Y_p\Delta p + (u_0 - Y_r)\Delta r - (g \cos \theta_0)\Delta\Phi &= Y_{\delta_r}\Delta\delta_r \\ -L_v\Delta v + \left(\frac{d}{dt} - L_p\right)\Delta p - \left(\frac{I_{yz}}{I_x}\frac{d}{dt} + L_r\right)\Delta r &= L_{\delta_a}\Delta\delta_a + L_{\delta_r}\Delta\delta_r \\ -N_v\Delta v - \left(\frac{I_{xz}}{I_z}\frac{d}{dt} + N_p\right)\Delta p + \left(\frac{d}{dt} - N_r\right)\Delta r &= N_{\delta_a}\Delta\delta_a + N_{\delta_r}\Delta\delta_r \end{aligned} \quad (8)$$

As the longitudinal motion also in this situation the derivatives are dependent to the change of different volumes: rolling rate, yawing rate, deflection angle of aileron and rudder.

Derivatives due to the side-slip angle (Eq. (9)):

$$C_{l\beta} = -0,0306$$

$$C_{n\beta} = 0,4924 \quad (9)$$

$$C_{Y\beta} = -0,7005$$

Derivative due to the rolling rate, p (Eq. (10)):

$$\begin{aligned} C_{lp} &= -\frac{C_{L\alpha}}{12} \left( \frac{1-3\lambda}{1+\lambda} \right) \\ C_{Np} &= -\frac{C_{Leq}}{8} \\ C_{Yp} &= 0 \end{aligned} \quad (10)$$

Derivative due to the Yawing rate, r (Eq. (11)):

$$\begin{aligned} C_{lr} &= \frac{C_{Leq}}{4} + \frac{z_v}{b} C_{Yr} \\ C_{Nr} &= -2 C_{Y\beta} \left( \frac{l_v}{b} \right)^2 \\ C_{Yr} &= -2 \left( \frac{l_v}{b} \right) C_{Y\beta} \end{aligned} \quad (11)$$

Derivative due to the change of deflection angle of Aileron (Eq. (12)):

$$\begin{aligned} C_{l\delta_a} &= \frac{2 C_{L\alpha} \tau \int_{y_1}^{y_2} c \, dy}{S_{ref} b} \\ C_{N\delta_a} &= 2 (-0,1) C_{L0} C_{l\delta_a} \\ C_{Y\delta_a} &= 0 \end{aligned} \quad (12)$$

Derivative due to the change of deflection angle of Rudder (Eq. (13)):

$$\begin{aligned} C_{l\delta_r} &= \frac{S_r}{S_{ref}} \left( \frac{z_v}{b} \right) C_{L\alpha_w} \\ C_{N\delta_r} &= -V_{wv} C_{L\alpha_t} \\ C_{Y\delta_r} &= \frac{S_v}{S_{ref}} C_{L\alpha_t} \end{aligned} \quad (13)$$

In Table 2.4.1 the values of aerodynamic coefficients are presented:

	$\delta C_l$	$\delta C_N$	$\delta C_Y$
$\delta p$	-0,8142	-0,0755	0
$\delta r$	0,1280	-0,0526	-0,2714
$\delta d_r$	0,0348	-0,1362	0,3984
$\delta d_a$	0,1681	-0,0105	0
$\delta \beta$	-0,0306	0,4924	-0,7005

Table 2.4-1 Lateral-Directional derivatives coefficients

With these values of the coefficients a steady state matrix is building.

$$\begin{cases} \dot{x} = A x + B u \\ y = C x + D u \end{cases} \quad (14)$$

In which  $x$  represents the state vector  $x = \{ \beta \ p \ r \ \phi \ \psi \}^T$ ,  $u$  the control vector,  $u = \{ d_a \ d_r \}^T$  and  $y$  the vector of controlled variables  $y = \{ p \ r \}^T$ . For this analysis, dimensional system is considered. In this condition the matrix A (matrix of state variables  $\mathbb{R}^{5 \times 5}$ ) is composed of the follow terms:

$a_{1,1} = Y_v/m$	$a_{1,2} = Y_p/m$	$a_{1,3} = \frac{Y_r}{m} - V$	$a_{1,4} = g$	$a_{1,5} = 0$
$a_{2,1} = \frac{L_v}{I_{xx}} + N_v I_{xz}$	$a_{2,2} = \frac{L_p}{I_{xx}} + N_p I_{xz}$	$a_{2,3} = \frac{L_r}{I_{xx}} + N_r I_{xz}$	$a_{2,4} = 0$	$a_{2,5} = 0$
$a_{3,1} = L_v I_{xz} + \frac{N_v}{I_{zz}}$	$a_{3,2} = L_p I_{xz} + \frac{N_p}{I_{zz}}$	$a_{3,3} = L_r I_{xz} + \frac{N_r}{I_{zz}}$	$a_{3,4} = 0$	$a_{3,5} = 0$
$a_{4,1} = 0$	$a_{4,2} = 1$	$a_{4,3} = 0$	$a_{4,4} = 0$	$a_{4,5} = 0$
$a_{5,1} = 0$	$a_{5,2} = 0$	$a_{5,3} = 1$	$a_{5,4} = 0$	$a_{5,5} = 0$

Table 2.4-2: Detail of matrix of state variables for lateral-directional dynamic

Figure 2.4-1 shows the graphic representation of the eigenvalues of the lateral directional motion. All the modes are stable whit the only exception of the spiral mode that is unstable. In a normal vehicle the spiral mode could be unstable, but the value of damping should be minor than 0.01 to have a minimum time to double amplitude  $T_2 > 70 \text{ sec}$ . In this case the value of the damping is equal  $\zeta =$



0,0787 and the value of the time to double is  $T_2 = 8,8075 \text{ sec}$ . The minimum time to double amplitude is very low, so a controller is necessary to have a stable dynamic. The spiral mode consists of yawing motion with some roll. It is common for the spiral mode to be unstable and the motion then consists of increasing yaw and roll angles in a tightening downward spiral. These facts allow approximations to be devised by modifying the  $\dot{\beta}$  equations and leaving the moment equations unchanged. Side-force due to sideslip is eliminated from the equation,  $\dot{\beta}$  is neglected, and the gravity force is balanced against the force component associated with yaw rate. Because the gravity force is intimately involved in the spiral mode the mode is dependent on flight-path angle. For the analysis a level flight assumption has been done. When the simplified determinant is expanded, the following second order characteristic equation is obtained (Eq. (15)) [4]:

$$N'_\beta s^2 + (L'_\beta N'_p - L'_p N'_\beta - L'_\beta g_D / V_{T_e})s + (L'_\beta N'_r - N'_\beta L'_r)g_D / V_{T_e} = 0 \quad (15)$$

The quadratic constant term divided by the roll root gives the reciprocal of the spiral time constant  $\tau_S$  (Eq. (16))

$$\tau_S \approx \frac{L'_\beta N'_p - L'_p N'_\beta - L'_\beta g_D / V_{T_e}}{(L'_\beta N'_r - N'_\beta L'_r)g_D / V_{T_e}} \quad (16)$$

Note that a negative value for the rime constant will simply mean an unstable exponential mode.

The numerator of the spiral equation is the same as the denominator of the roll equation, and making the same approximation as show in Eq. (17)

$$\tau_S \approx \frac{-L'_p N'_\beta}{(L'_\beta N'_r - L'_r N'_\beta)} = \frac{-C_{\ell_p} C_{n_\beta}}{(C_{\ell_\beta} C_{n_r} - C_{\ell_r} C_{n_\beta})} \frac{V_{T_e}}{g_D} \quad (17)$$

$$\begin{aligned}
C_{lp} &< 0 \\
C_{n\beta} &< 0 \\
(C_{l\beta}C_{nr} - C_{lr}C_{n\beta}) &< 0
\end{aligned} \tag{18}$$

This equation indicates that the spiral time constant is proportional to speed, given the earlier approximations, and that the stability derivatives remain constant.

The condition for a pole at the origin is given by  $|A| = 0$ , and in the case for the lateral dynamic this normally represents the spiral pole becoming neutrally stable.

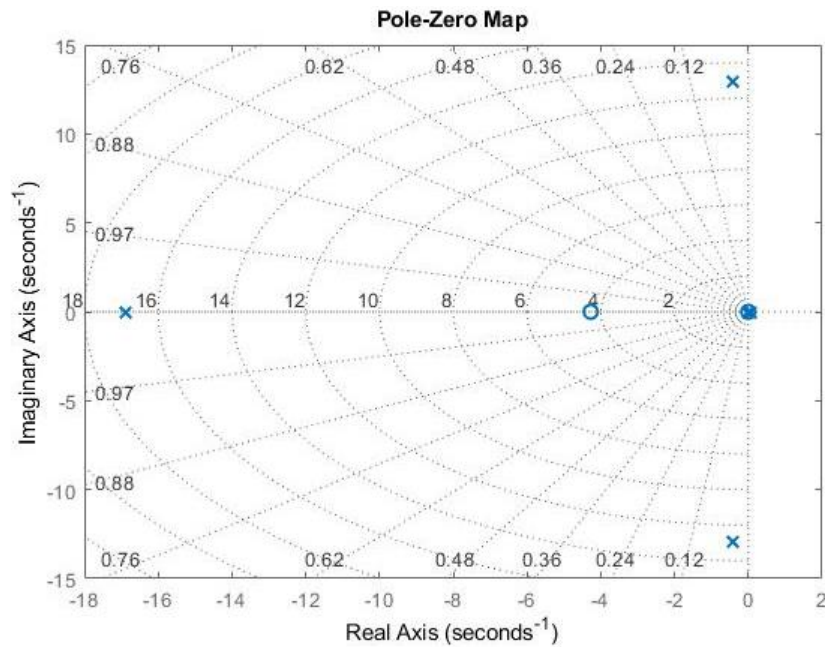


*Figure 2.4-1 Root Loci Lateral Directional Dynamic*

The values of the eigenvalues are:

$$\begin{aligned}
\lambda_1 &= -16,8708 \\
\lambda_2 &= 0,0787 \\
\lambda_{3,4} &= -0,4051 \pm 12,9478i
\end{aligned} \tag{19}$$

## 2.5 Thrust and Torque

The propulsion system has a very particular configuration. The hybrid propeller (see Figure 2.1-3), designed by the Bologna university student Antonio Bacciaglia [5], and the rotor was tested on a test bench and in a water tank to verify the numerical results obtained by the fluid dynamic simulation. In Figure 2.5-1 and Figure 2.5-2, the evolution of thrust and torque is diagrammed for different revolutions per minute (RPM).

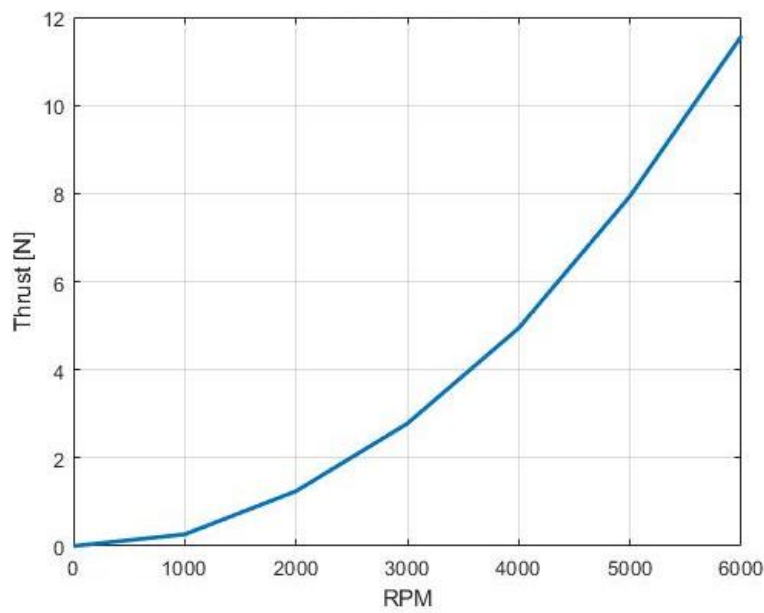


*Figure 2.5-1 Rotor Thrust for different RPM*

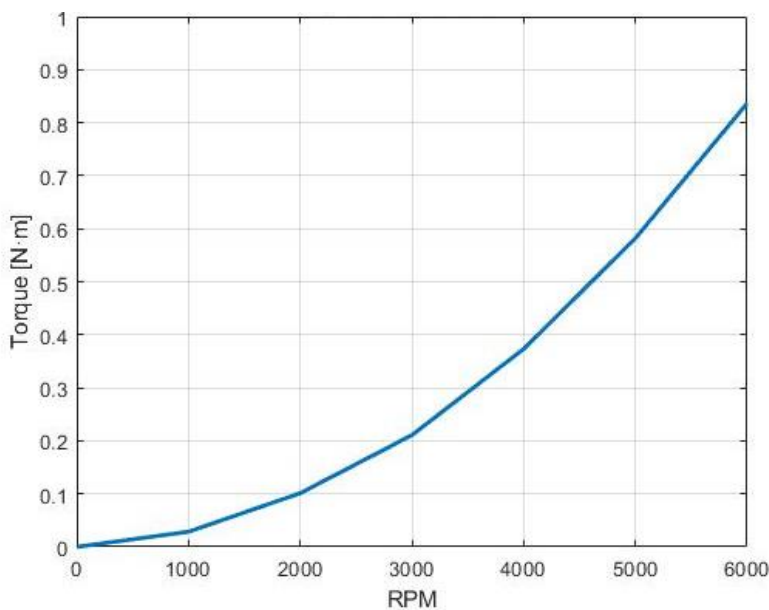


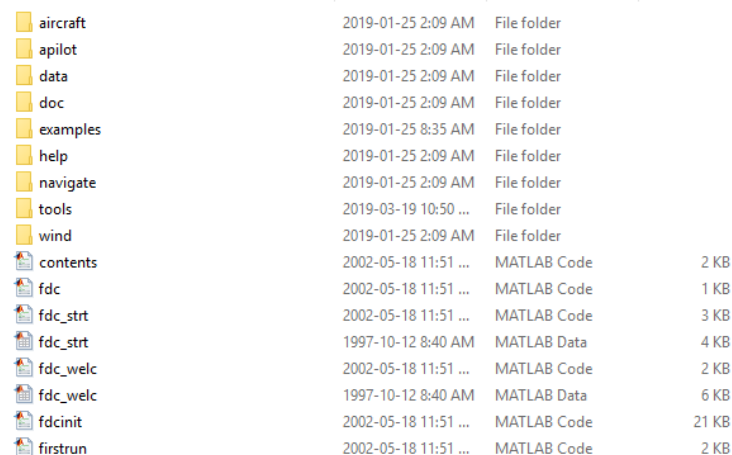
*Figure 2.5-2 Rotor Torque for different RPM*

# Chapter 3: Simulator Implementation

---

## 3.1 Flight Dynamics and Control toolbox

The study of the BUUAS' dynamic is made considering two different aerodynamic model. In order to study the dynamic a Simulator has been implemented. As simulator model the Flight Dynamics and Control (FDC toolbox) toolbox has been taken in consideration. The FDC toolbox is a toolbox developed in the MATLAB® and SIMULINK environment. At the beginning it has been utilised to implement the autopilot for the De Havilland 'Beaver' aircraft. (For more information read the FDC12\_report.pdf [6]). The FDC toolbox is composed by the follow folders as shown in the Figure 3.1-1.



aircraft	2019-01-25 2:09 AM	File folder	
apilot	2019-01-25 2:09 AM	File folder	
data	2019-01-25 2:09 AM	File folder	
doc	2019-01-25 2:09 AM	File folder	
examples	2019-01-25 8:35 AM	File folder	
help	2019-01-25 2:09 AM	File folder	
navigate	2019-01-25 2:09 AM	File folder	
tools	2019-03-19 10:50 ...	File folder	
wind	2019-01-25 2:09 AM	File folder	
contents	2002-05-18 11:51 ...	MATLAB Code	2 KB
fdc	2002-05-18 11:51 ...	MATLAB Code	1 KB
fdc_strt	2002-05-18 11:51 ...	MATLAB Code	3 KB
fdc_strt	1997-10-12 8:40 AM	MATLAB Data	4 KB
fdc_welc	2002-05-18 11:51 ...	MATLAB Code	2 KB
fdc_welc	1997-10-12 8:40 AM	MATLAB Data	6 KB
fdcinit	2002-05-18 11:51 ...	MATLAB Code	21 KB
firstrun	2002-05-18 11:51 ...	MATLAB Code	2 KB

*Figure 3.1-1 Folder FDC toolbox*

In each folder there are MATLAB® function and SIMULINK model that could be modified to build, step by step, a simulator for different vehicle. The follow modifies have been done to adapt the FDC toolbox of 'Beaver' aircraft to the BUUAS vehicle:

- Aircraft dimensions, weight and inertial;
- Aerodynamic model;
- Propulsion system model.

All these volumes are collected in a MATLAB® functions 'modbuild.m', that is positioned in the folder 'aircraft' of the FDC toolbox.

### 3.2 Dimensions, Weights and Inertia

The FDC toolbox require the fundamental dimensions and data of the aircraft (see Table 3.2-1). All dimensions and inertia come from the CAD project develop by Dian Guo [7] (see Figure3.2-1). The weight considered is that the BUUAS would have after the transition: the water and CO2 volumes are not considered because, for hypothesis, all these volumes are used during the transition phase.

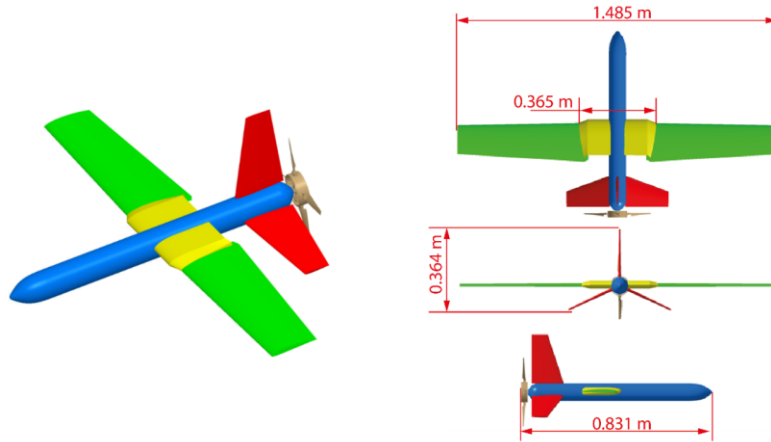


Figure 3.2-1 Geometric Dimension of BUUAS

BUUAS DATA	
$W$ [kg]	3,59
$S_{ref}$ [m <sup>2</sup> ]	0,238
$b$ [m]	1,485
$c_{bar}$ [m]	0,158
$I_{xx}$ [kg m <sup>2</sup> ]	0,154
$I_{yy}$ [kg m <sup>2</sup> ]	0,107
$I_{zz}$ [kg m <sup>2</sup> ]	0,257
$I_{xy}$ [kg m <sup>2</sup> ]	0
$I_{xz}$ [kg m <sup>2</sup> ]	$2,669 \cdot 10^{-4}$
$I_{yz}$ [kg m <sup>2</sup> ]	0

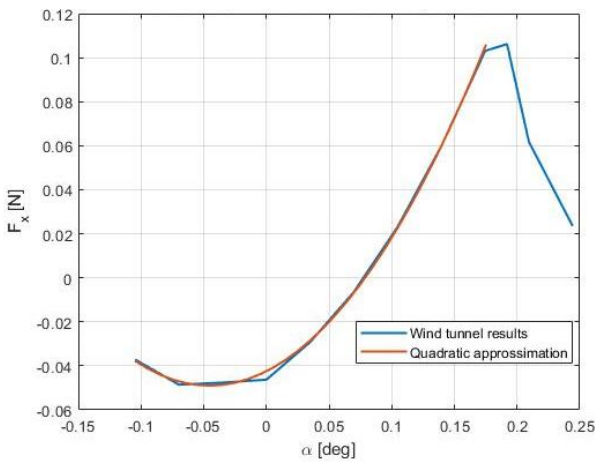
Table 3.2-1: BUUAS geometric dimension, weights and inertia

### 3.3 Aerodynamic Model

For BEAVER aircraft a non-linear aerodynamic model was developed. It is composed of aerodynamic force and moment coefficients, in the body-fixed reference frame, as shown by the Eq. (20) [8]:

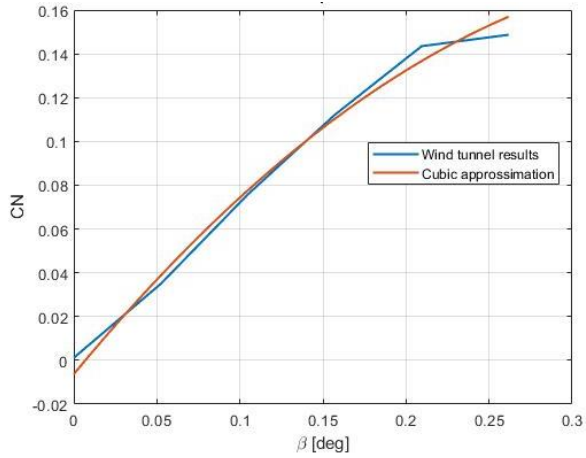
$$\begin{aligned}
 C_{X_a} &= C_{X_0} + C_{X_\alpha} \alpha + C_{X_{\alpha^2}} \alpha^2 + C_{X_{\alpha^3}} \alpha^3 + C_{X_q} \frac{q\bar{c}}{V} + C_{X_{\delta_r}} \delta_r + C_{X_{\delta_f}} \delta_f + C_{X_{\alpha\delta_f}} \alpha \delta_f \\
 C_{Y_a} &= C_{Y_0} + C_{Y_\beta} \beta + C_{Y_p} \frac{pb}{2V} + C_{Y_r} \frac{rb}{2V} + C_{Y_{\delta_a}} \delta_a + C_{Y_{\delta_r}} \delta_r + C_{Y_{\delta_r\alpha}} \delta_r \alpha + C_{Y_{\dot{\beta}}} \frac{\dot{\beta}b}{2V} \\
 C_{Z_a} &= C_{Z_0} + C_{Z_\alpha} \alpha + C_{Z_{\alpha^3}} \alpha^3 + C_{Z_q} \frac{q\bar{c}}{V} + C_{Z_{\delta_e}} \delta_e + C_{Z_{\delta_e\beta^2}} \delta_e \beta^2 + C_{Z_{\delta_f}} \delta_f + C_{Z_{\alpha\delta_f}} \alpha \delta_f \\
 C_{l_a} &= C_{l_0} + C_{l_\beta} \beta + C_{l_p} \frac{pb}{2V} + C_{l_r} \frac{rb}{2V} + C_{l_{\delta_a}} \delta_a + C_{l_{\delta_r}} \delta_r + C_{l_{\delta_a\alpha}} \delta_a \alpha \\
 C_{m_a} &= C_{m_0} + C_{m_\alpha} \alpha + C_{m_{\alpha^2}} \alpha^2 + C_{m_q} \frac{q\bar{c}}{V} + C_{m_{\delta_e}} \delta_e + C_{m_{\beta^2}} \beta^2 + C_{m_r} \frac{rb}{2V} + C_{m_{\delta_f}} \delta_f \\
 C_{n_a} &= C_{n_0} + C_{n_\beta} \beta + C_{n_p} \frac{pb}{2V} + C_{n_r} \frac{rb}{2V} + C_{n_{\delta_a}} \delta_a + C_{n_{\delta_r}} \delta_r + C_{n_q} \frac{q\bar{c}}{V} + C_{n_{\beta^3}} \beta^3
 \end{aligned} \tag{20}$$

BUUAS' aerodynamic model is build considering all the moment and force coefficients that have been deducted by the results of the wind tunnel test. Coefficients have been obtained with an approximation of results of wind tunnel test and, where is possible, follow the formulation reported by the book 'Flight Stability and Automatic Control' of Dr. Robert C. Nelson [9].



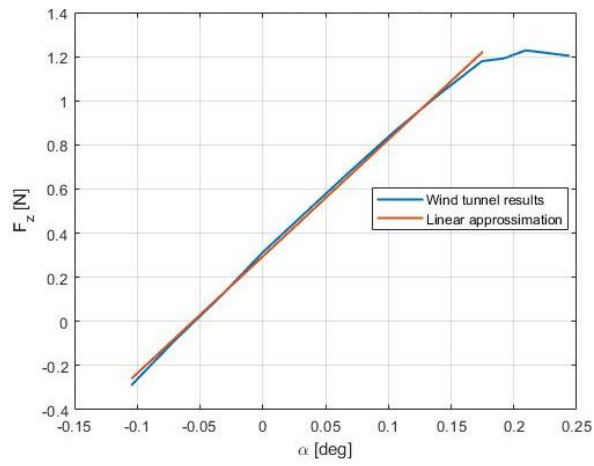
$$C_X = -0,0426 + 0,2887 \alpha + 3,2063 \alpha^2 \tag{21}$$

Figure 3.3-1 X-Force wind tunnel result and approximation



**Figure 3.3-2 Y-Force wind tunnel result and approximation**

$$C_Y = 0,0016 - 0,7587 \beta + 0,2778 \beta^2 \quad (22)$$



**Figure 3.3-3 Z-Force wind tunnel result and approximation**

$$C_Z = +0,2955 + 5,3007 \alpha \quad (23)$$

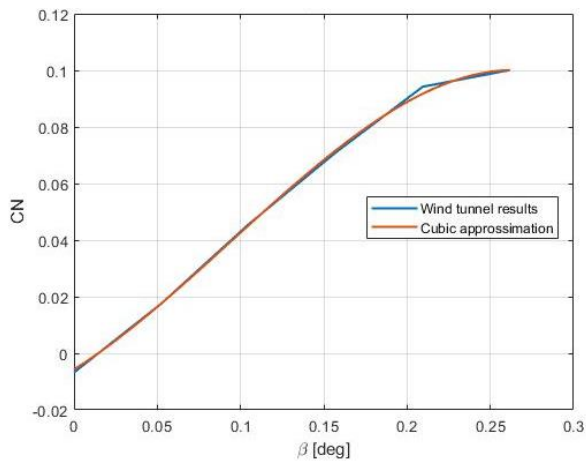


**Figure 3.3-4: Yaw Moment wind tunnel result and approximation**

$$C_n = -0,0071 + 0,4423 \beta + 0,8183 \beta^2 - 3,0648 \beta^3 \quad (24)$$

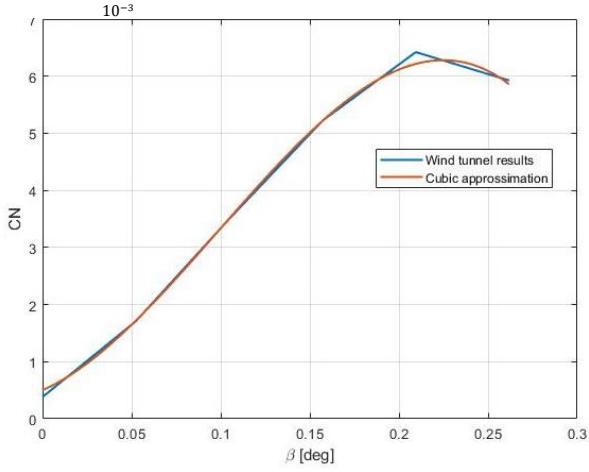


**Figure 3.3-5 Roll Moment wind tunnel and approximation**

$$C_l = -4,2707 \cdot 10^{-4} - 0,0188 \beta - 0,1544 \beta^2 + 0,5190 \beta^3 \quad (25)$$

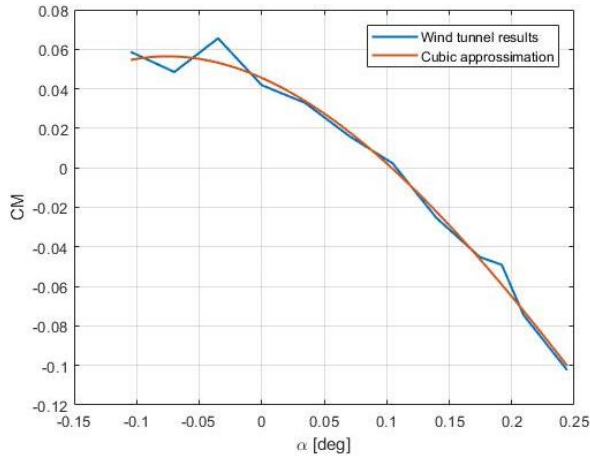


**Figure 3.3-6 Pitch Moment wind tunnel results and approximation**

$$C_m = 0,044 - 0,2744 \alpha - 1,3481 \alpha^2 \quad (26)$$

The aerodynamic model use for the BUUAS aircraft is expressed by the Eq. (27):

$$C_{X_a} = C_{X_0} + C_{X_\alpha} \alpha + C_{X_{\alpha^2}}$$

$$C_{Y_a} = C_{Y_0} + C_{Y_\beta} \beta + C_{Y_{\beta^2}} \beta^2 + C_{Y_p} \frac{pb}{2V} + C_{Y_r} \frac{rb}{2V} + C_{Y_{\delta_r}} \delta_r$$

$$C_{Z_a} = C_{Z_0} + C_{Z_\alpha} \alpha + C_{Z_{\delta_e}} \delta_e$$

$$C_{l_a} = C_{l_0} + C_{l_\beta} \beta + C_{l_{\beta^2}} \beta^2 + C_{l_{\beta^3}} \beta^3 + C_{l_p} \frac{pb}{2V} + C_{l_r} \frac{rb}{2V} + C_{l_{\delta_a}} \delta_a + C_{l_{\delta_r}} \delta_r \quad (27)$$



$$C_{n_a} = C_{n_0} + C_{n_\beta}\beta + C_{n_{\beta^2}}\beta^2 + C_{n_{\beta^3}}\beta^3 + C_{n_p}\frac{pb}{2V} + C_{n_r}\frac{rb}{2V} + C_{n_{\delta_a}}\delta_a + C_{n_{\delta_r}}\delta_r$$

$$C_{m_a} = C_{m_0} + C_{m_\alpha}\alpha + C_{m_{\alpha^2}}\alpha^2 + C_{m_q}\frac{q\bar{c}}{V} + C_{m_{\delta_e}}\delta_e$$

The reference system used in the FDC toolbox is a Body-fixed frame as show in the Figure 3.3-7 (black lines). For the wind tunnel test, volumes of forces and moments are register by a load cell. The reference system of the load cell used is shown in Figure 3.3-7 (red lines). In order to obtain valid results for the simulation, the sign of the coefficients of the approximation are changed for X and Z-force and the Roll moment.

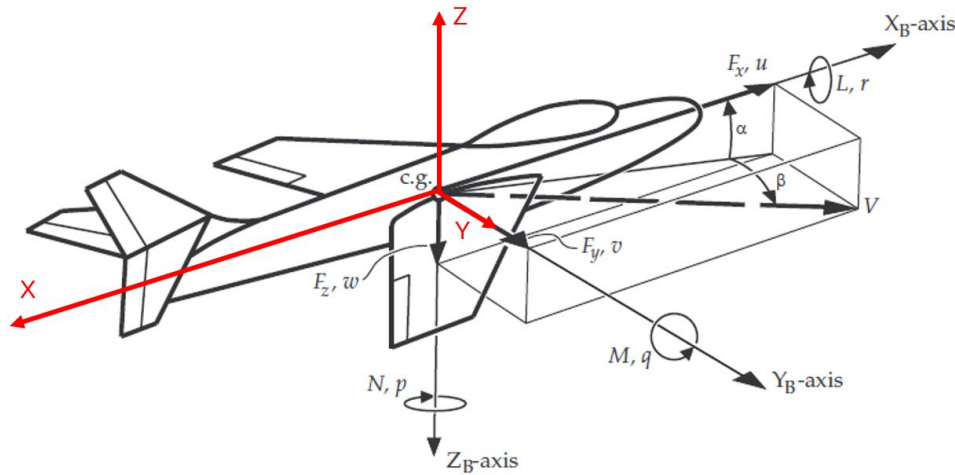


*Figure 3.3-7 Wind tunnel (black lines) and Simulator (red lines) Reference system*

The values of the coefficients write in Eq. (27) are shown in Table 3.3-1 and Table 3.3-2, considering the body-fixed frame reference:

$C_X$		$C_Y$		$C_Z$	
<b>0</b>	−0,0426	<b>0</b>	0,0016	<b>0</b>	−0,2955
$\alpha$	0,2887	$\beta$	−0,7587	$\alpha$	−5,3007
$\alpha^2$	3,2063	$\beta^2$	0,2778	$\delta_e$	<u>−0,6759</u>
		$\frac{pb}{2V}$	0		
		$\frac{rb}{2V}$	0,294		
		$\delta_r$	0,3984		

Table 3.3-1: Force coefficients

$C_l$		$C_n$		$C_m$	
<b>0</b>	$-4,2707 \cdot 10^{-4}$	<b>0</b>	−0,0071	<b>0</b>	0,0419
$\beta$	−0,0188	$\beta$	0,4423	$\alpha$	−0,2744
$\beta^2$	−0,1544	$\beta^2$	0,8183	$\alpha^2$	−1,3481
$\beta^3$	0,5190	$\beta^3$	−3,0648	$\frac{q\bar{c}}{V}$	−2,6412
$\frac{pb}{2V}$	−0,8142	$\frac{pb}{2V}$	−0,0775	$\delta_e$	−0,8159
$\frac{rb}{2V}$	0,1274	$\frac{rb}{2V}$	−0,0528		
$\delta_a$	0,2021	$\delta_a$	−0,0114		
$\delta_r$	0,0033	$\delta_r$	−0,1362		

Table 3.3-2: Moment coefficients

### 3.4 Propulsion System Model

A non-linear polynomial functions have been defined to approximate the force and moments due to the engine model of Beaver aircraft. The propulsion system of BUUAS has been tested only on test bench, so the force and moments generated by the rotor change only with a different RPM. Because, also, theoretically, the rotation axis of the propeller coincides with the X-axis body of the vehicle, it is possible to consider only the force and the moment along the X-axis. The parameter model define for the BUUAS vehicle is explain by Eq. (28):

$$C_{X_p} = C_{X_0} + C_{X_{RPM}} RPM + C_{X_{RPM^2}} RPM^2$$

$$C_{l_p} = C_{l_0} + C_{l_{RPM}} RPM + C_{l_{RPM^2}} RPM^2 \quad (28)$$

The values of the coefficients are shown in Table 3.4-1:

	$C_{X_p}$	$C_{l_p}$
<b>0</b>	0,0809	0,0066
<b><i>RPM</i></b>	$-8,7274 \cdot 10^{-6}$	$1,7320 \cdot 10^{-6}$
<b><i>RPM</i><sup>2</sup></b>	$3,3385 \cdot 10^{-7}$	$2,2815 \cdot 10^{-8}$

*Table 3.4-1: Rotor Coefficients*

Evolution of Thrust and Torque with the curve approximation are show in Figure 3.4-1 and 3.4-2:

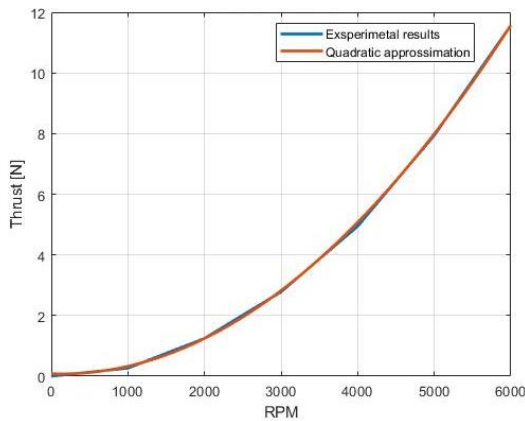


*Figure 3.4-1 Thrust experimental results and approximation*

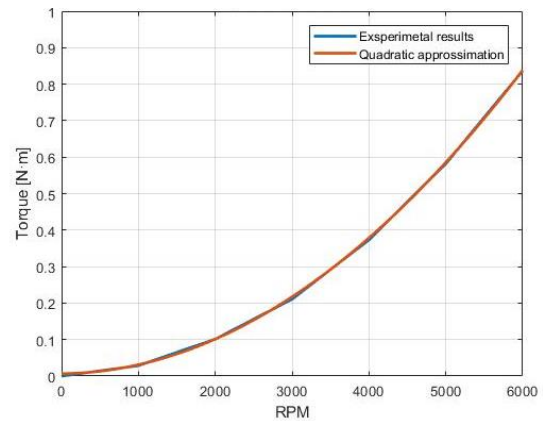


*Figure 3.4-2 Torque experimental results and approximation*

### 3.5 Trimmed Flight Condition

The next step, to build the simulator, is to find the trimmed flight condition. The trimmed conditions are defined as conditions in which the linear and angular velocity are constant in time, therefore the steady-state flight condition is satisfied. The FDC toolbox uses an algorithm to find the trimmed flight condition. This algorithm has been stored in the file ‘actrim.m’ in the folder ‘tools’. The program uses two MATLAB® function: ACCONSTR, which contains the flight-path constraints and kinematic relationships, and ACCOST, which evaluates the cost-function for the minimization algorithm. The cost-function has been modified from the original one used for the Beaver aircraft (Eq. (29)).

$$J = \dot{V}^2 + 2 (\dot{\alpha}^2 + \dot{\beta}^2) + 8 (\dot{p}^2 + \dot{q}^2 + \dot{r}^2) \quad (29)$$

The function ‘actrim.m’ uses a MATLAB® routine FMINS to find the minimum of the cost-function, determining the numerical trimmed flight condition. The trimmed conditions are used as initial values for the integration of the non-linear equation of the motion. The results of the trimmed routine have been stored in four vector: *xinco*, in which there are the initial values of the state vector, *uprop0*, in which there are the initial values of engine control inputs, *uaero0*, in which there are the initial values of aerodynamic control inputs, and *xdot0*, vector with the derivatives in time of the state vector. Below results of trimmed conditions are shown in Table 3.5-1:

<i>xinco</i>		<i>xdot0</i>		<i>uaero0</i>	
<i>V</i> [m/s]	21	$\dot{V}$ [m/s <sup>2</sup> ]	$-7,0015 \cdot 10^{-12}$	<i>d<sub>e</sub></i> [rad]	0,016
<i>α</i> [rad]	0,0462	$\dot{\alpha}$ [rad/s]	$-7,56 \cdot 10^{-12}$	<i>d<sub>a</sub></i> [rad]	0,0168
<i>β</i> [rad]	0,0327	$\dot{\beta}$ [rad/s]	$1,6159 \cdot 10^{-11}$	<i>d<sub>r</sub></i> [rad]	0,0582
<i>p</i> [rad/s]	0	$\dot{p}$ [rad/s <sup>2</sup> ]	$1,281 \cdot 10^{-11}$	<i>d<sub>f</sub></i> [rad]	0
<i>q</i> [rad/s]	0	$\dot{q}$ [rad/s <sup>2</sup> ]	$1,5683 \cdot 10^{-11}$	<i>uprop0</i>	
<i>r</i> [rad/s]	0	$\dot{r}$ [rad/s <sup>2</sup> ]	$6,9482 \cdot 10^{-12}$		
<i>ψ</i> [rad]	0	$\dot{\psi}$ [rad/s]	0	<i>n</i> [RPM]	3250
<i>θ</i> [rad]	0,0535	$\dot{\theta}$ [rad/s]	0	<i>pz</i>	20
<i>φ</i> [rad]	0	$\dot{\phi}$ [rad/s]	0		
<i>x<sub>e</sub></i> [m]	0	$\dot{x}_e$ [m/s]	20,9882		
<i>y<sub>e</sub></i> [m]	0	$\dot{y}_e$ [m/s]	0,6861		
<i>H</i> [m]	0	$\dot{H}$ [m/s]	0,1531		

Table 3.5-1: Trimmed Condition

In order to find if the condition found corresponds a real steady-state condition, a first simulation has been run using the Simulink model 'oloop1.mdl'. This Simulink model is stored in the folder 'examples'. As shown in the Figure 3.5-1, the simulation, at first, has been run without an external input of surface control and as initial condition has been considered the trimmed condition before found.

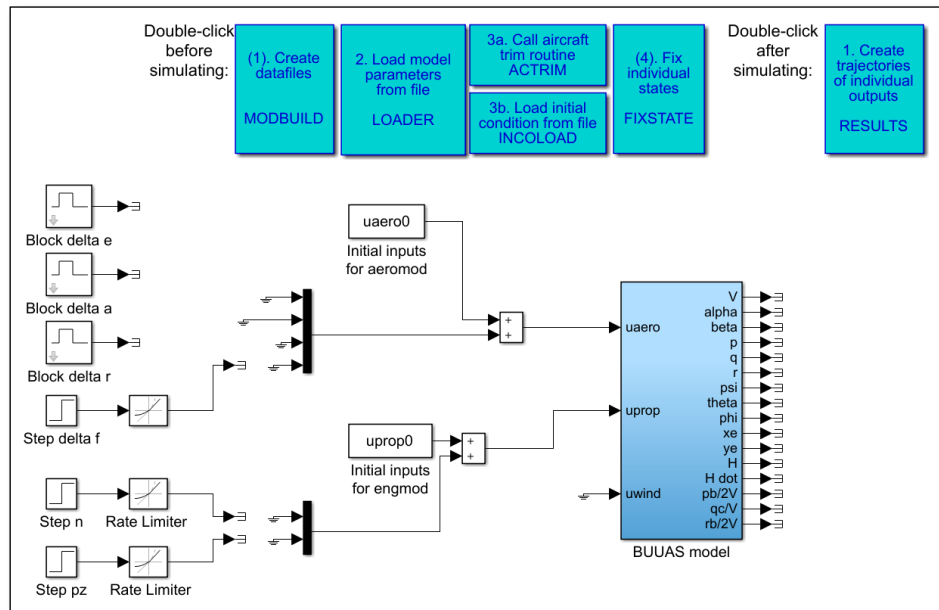


**Figure 3.5-1 Simulink Model BUUAS Dynamic**

The results of the simulation are shown in Figure 3.5-2 - 3.5-9:

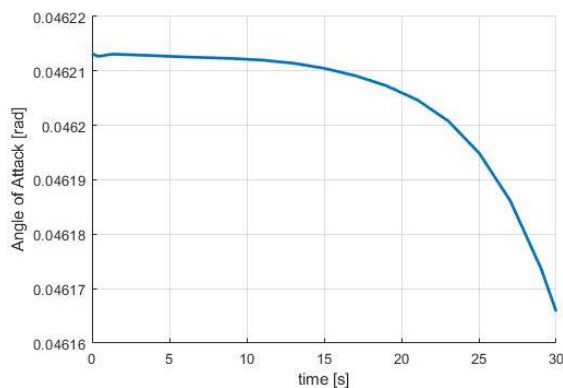


**Figure 3.5-2 Trimmed Condition: Angle of attack**

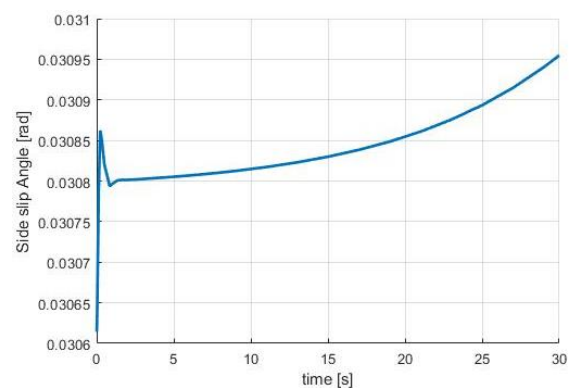


**Figure 3.5-3 Trimmed Condition: Side Slip Angle**

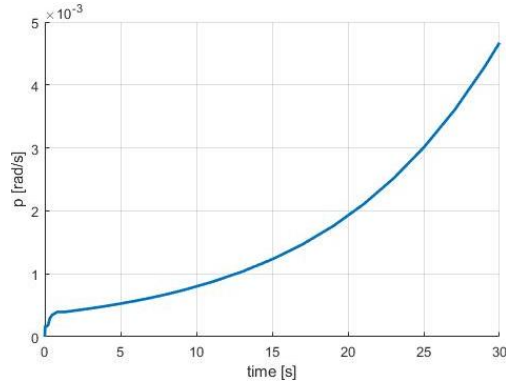


**Figure 3.5-4 Trimmed Condition: Angular Velocity  $p$**

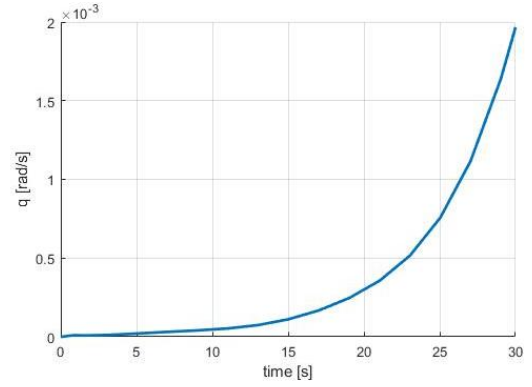


**Figure 3.5-5: Trimmed Condition: Angular Velocity  $q$**

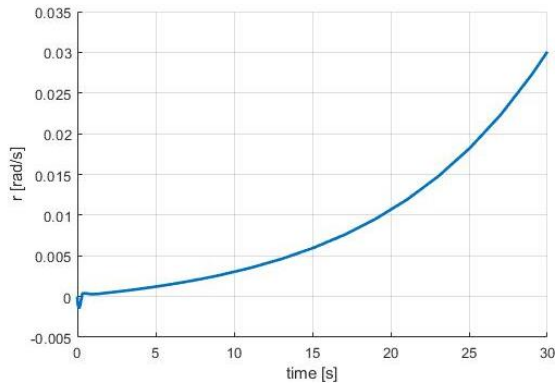


**Figure 3.5-6: Trimmed Condition: Angular Velocity  $r$**

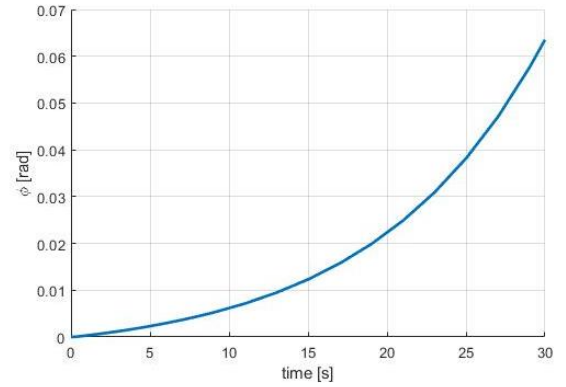


**Figure 3.5-7 Trimmed Condition: Bank Angle**

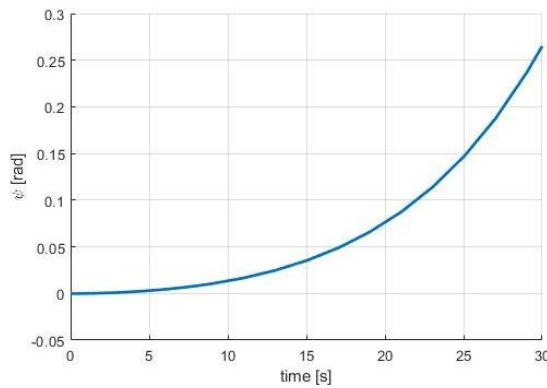


**Figure 3.5-8: Trimmed Condition: Yaw Angle**

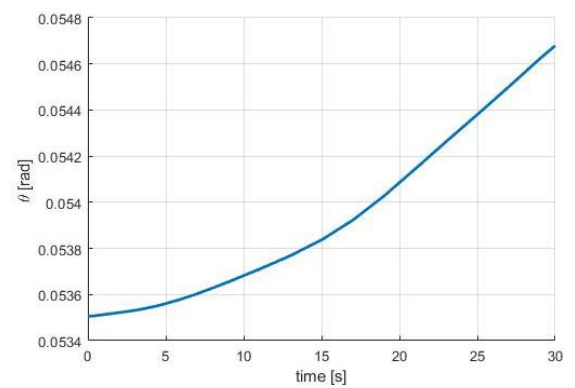


**Figure 3.5-9 Trimmed Condition: Pitch Angle**

The trimmed condition is satisfied because the variation of all volumes in 30 second is of the order of  $10^{-4}$  compared to the initial condition, so it is possible to considering constant the linear and angular velocity in time. The evolution for angular velocities, roll and yaw angles (Figure 3.15,3.16,3.17) shows the presence of an instability: even if the change is very small, they have a

non-convergent evolution. This behavior is due to the instability of the spiral mode, that is presents on the lateral direction dynamic. Around the trimmed conditions this effect is not very evident, but in a normal dynamic it could bring the vehicle to a no-stable dynamic.

### 3.6 Model Validation

Found the trimmed condition, it's able to validate the non-linear aerodynamic comparing the linearized dynamic obtained with the wind tunnel tests and the non-linear aerodynamic model used in the simulator. The MATLAB® function 'ACLIN' extracts the linearized aircraft models from the non-linear Simulink model, using as initial point the trimmed condition. The ACLIN routine uses a MATLAB® function LINMOD, to linearize the aircraft non-linear aerodynamic model. A comparison between linearized model found with the wind tunnel results and form the non-linear model of the simulator is done in the Figure 3.18. In Table 8 it is possible to see the difference of eigenvalues.

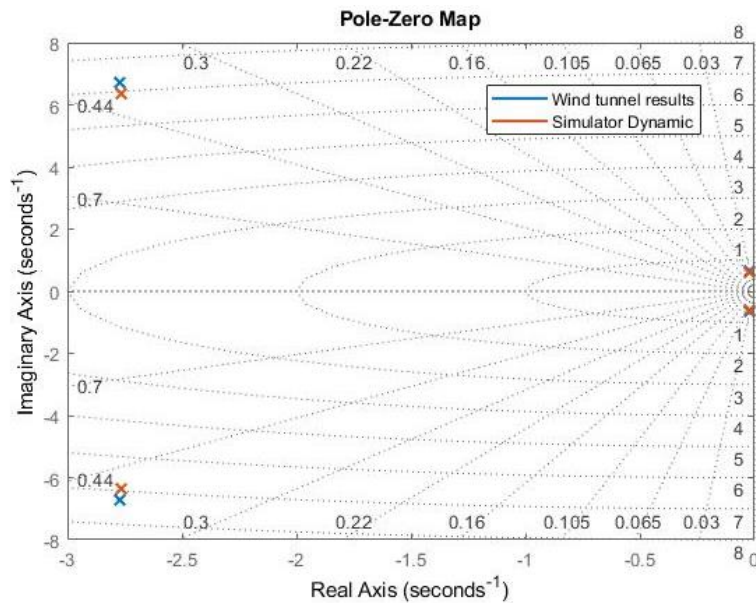


Figure 3.6-1 Root Loci Longitudinal dynamic: Wind tunnel and Simulator dynamic

	<b>WIND TUNNEL RESULTS</b>	<b>SIMULATOR AERODYNAMIC</b>
$\lambda_{1,2}$	$-2,7727 \pm i 6,70$	$-2,7635 \pm 6,3772i$
$\lambda_{3,4}$	$-0,021 \pm i 0,6677$	$-0,019 \pm 0,6278i$

Table 3.6-1 Wind tunnel and Simulator eigenvalues

The non-linear aerodynamic model, built for the simulator, gives similar results to the wind tunnel model, as it is possible to see in the Figure 3.18 and 3.19. Reference to Figure 3.19, it is possible to see that the eigenvalues of Dutch Roll and Roll mode are different for aerodynamic model used in the simulator. They give a faster and damper dynamic in the lateral directional motion.

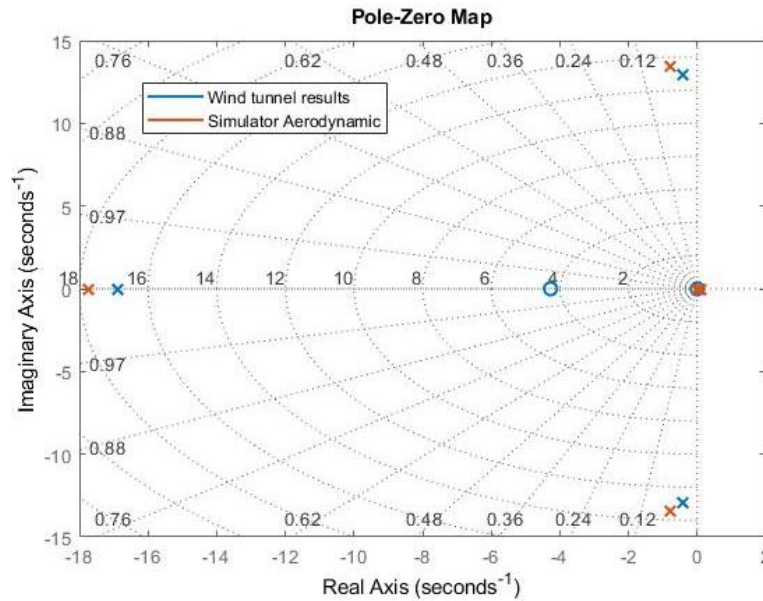


Figure 3.6-2 Root Loci Lateral-Directional dynamic: Wind tunnel and Simulator dynamic

	WIND TUNNEL RESULTS	SIMULATOR AERODYNAMIC
$\lambda_1$	-16,8708	-17,7453
$\lambda_2$	0,0787	0,0965
$\lambda_{3,4}$	$-0,4051 \pm 12,9478i$	$-0,7679 \pm 13,4422i$

Table 3.6-2 Wind tunnel and Simulator eigenvalues

Because in the trimmed condition variation of angles is very small, a confront between forces and moments obtain during a simulation and came from the wind tunnel results is done in a different simulation.



# Chapter 4: Autopilot

---

## 4.1 Flying Qualities

The BUUAS is a military-unmanned vehicle, so it is necessary to provide the essential autopilots to complete its mission profile safely. In order to define an analytical specification for the autopilots to follow, the MIL-HDBK-1797 is taken in consideration. In the MIL-HDBK-1797 [10], a division of a different airplane, different flight phases and flying-qualities levels are made and follow presented in Table 4.1-1. It is possible to see that the BUUAS cannot be ascribed to any of the classes described to the MIL-HDBK-1797, because they are referred to a piloted vehicle. For these reasons, a new specification is formulated for each autopilot, starting from the military regulations, but relaxing specifications where possible. The mission completed and the structural safety of the vehicle are the most important objective for the new specification.

<i>Airplane Classes</i>	<i>Definitions</i>
CLASS I	Small, light airplanes
CLASS II	Medium weight, low-to-medium-maneuverability airplanes
CLASS III	Large, heavy, low to medium maneuverability airplanes
CLASS IV	High maneuverability airplanes
<i>Flight Phases</i>	<i>Definitions</i>
CATEGORY A	Nonterminal flight phases generally requiring rapid maneuvering
CATEGORY B	Nonterminal flight phases normally accomplished using gradual maneuvers without

	precision tracking, although accurate flight-path control may be required
CATEGORY C	Terminal flight phases normally accomplished using gradual maneuvers and usually requiring accurate flight path control
<b><i>Flying qualities levels</i></b>	<b><i>Definitions</i></b>
LEVEL 1	Flying qualities adequate for the mission flight phase
LEVEL 2	Flying qualities adequate to accomplish the mission flight phase, but some increase in pilot workload or degradation in mission effectiveness exists
LEVEL 3	Flying qualities such that the airplane can be controlled safely, but pilot workload is excessive, or mission effectiveness is inadequate or both

*Table 4.1-1: Class, Category and Phase definition MIL-HDBK-1797*

As done in the previous chapter for the analysis of the dynamic, also for the study of the autopilots a separation between the longitudinal and lateral-directional motion is done. For the longitudinal motion the requirements are specified in terms of time to rise (Eq. (30)) and peak of overshoot (Eq. (31)); for these two constants the value is obtained by the follow formula.

$$t_r = \frac{1 + 1,1 \zeta + 0,15 \zeta^2}{\omega_n} \quad (30)$$

$$M_p = 100 e^{-\frac{\pi \zeta}{\sqrt{1-\zeta^2}}} \quad (31)$$

For the lateral direction motions the requirements are specified by the Time constant for the Roll mode, the minimum doubling time for the Spiral mode, for the Dutch Rolle mode the time delay and

the time to peak. For the BUUAS vehicle only the Time constant for the Roll mode is taken in consideration and chose properly.

Most of the flying qualities specifications do not apply directly to autopilot design. Autopilots are been designed to follow specification on steady-state error and disturbance rejection. Important is also the way in which the autopilot is engaged and disengaged to not produce an uncomfortable or dangerous transient motion.

In the simulator the follow autopilots have been implemented:

- Pitch Attitude Hold (PAH)
- Roll Attitude Hold (RAH)
- Mach Hold (MH)
- Altitude Select (AS)
- Altitude Hold (AH)

All autopilots are implemented with the a PID (Proportional-Integral-Derivative) controller methodology. A tuning of all gains has been done in order to follow the new specifications chosen. The linear approximation of longitudinal and lateral-directional aerodynamic has been used for a first tuning of PAH and RAH autopilots. After find values of gains for these two autopilots a non-linear dynamic has been used to tuning the other autopilots.

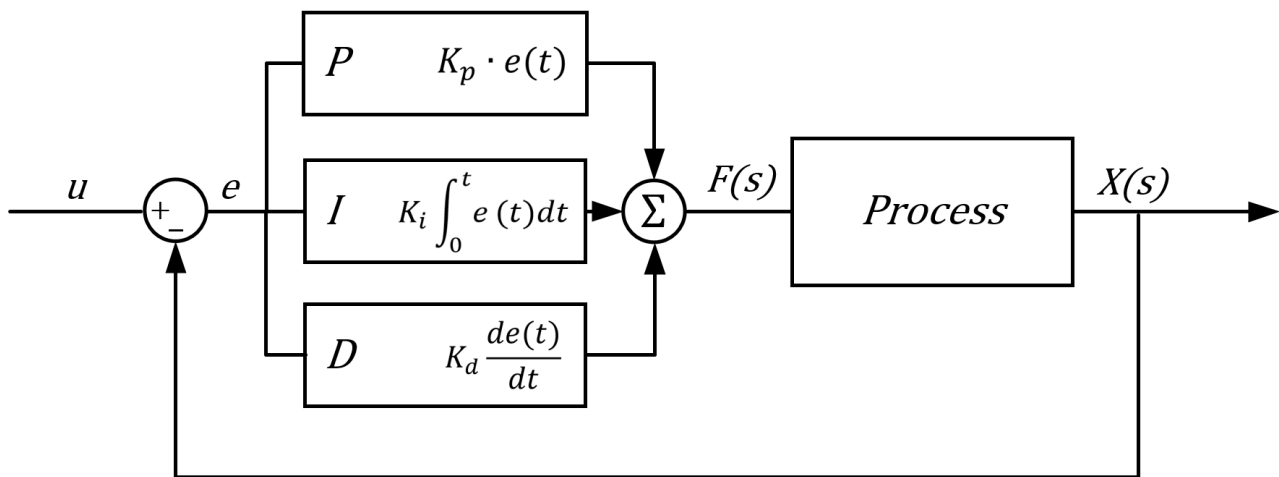


*Figure 4.1-1: PID controller representation*

## 4.2 Actuator

Dynamic of actuators has been approximated using a first order transfer function in which the time response of actuators mounted on the aircrafts has been used. For aileron, rudder and tail different servos are been used (see Table 4.2-1) [11] [12]. The transfer functions that have been found for each actuator are reported below (Eq. (32)).

Specification	Aileron servo	Tail servo
		
<b>Model</b>	Corona 919MG	Spektrum A3030
<b>Dimension</b>	22.5×11.5×24.6 mm	23.6×11.5×25.5 mm
<b>Torque</b>	1.5 kg·cm	1.66 kg·cm
<b>Weight</b>	12.5 g	8.6 g
<b>Operating Speed</b>	0.07 sec / 60°	0.12 sec / 60°

Table 4.2-1: Specification Aileron and Tail servo

$$TF_{Tail} = \frac{8,33}{s - 8,33}$$

$$TF_{Rudder} = \frac{8,33}{s - 8,33} \quad (32)$$

$$TF_{Aileron} = \frac{14,3}{s - 14,3}$$

## 4.3 Motor Dynamic

The presence of the electric motor has been considered with a Simulink subsystem show in Figure 4.3-1. The number of revolutions per minutes' results shows that the delay dues to the motor could be considered negligible. This is due to the small dimension of the motor and the low RPM used during the simulation.

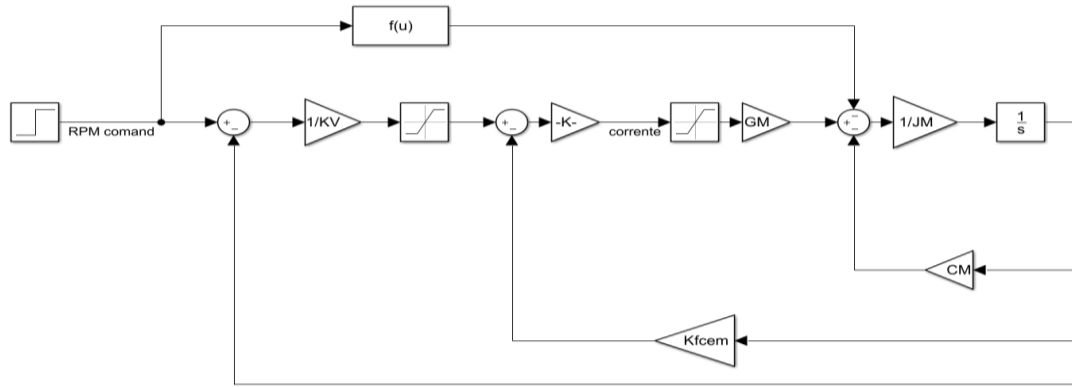


Figure 4.3-1: Scheme of Rotor

#### 4.4 Roll Attitude Hold (RAH)

An important consideration is given on the Spiral mode instability. Because of this instability, at first, a Roll Attitude Hold [13] autopilots have been designed. For this autopilot a PI (Proportional-Integrator) controller has been implemented. Variables controlled are the angular velocities,  $p$  and  $r$ . This autopilot is used as the inner feedback loop for other autopilots. As reference signal has been used two different double steps with different duration: one of  $t = 2,5 \text{ sec}$  and one of  $t = 5 \text{ sec}$ . The reference signal is filtered with transfer function that follow the specification before reported. For the Roll Attitude Hold a transfer function of the first order is used with the constant time of  $t = 4,5 \text{ sec}$ . For the study of this autopilot the longitudinal states are fixed in order to investigate only the motion in the lateral-directional dynamic.

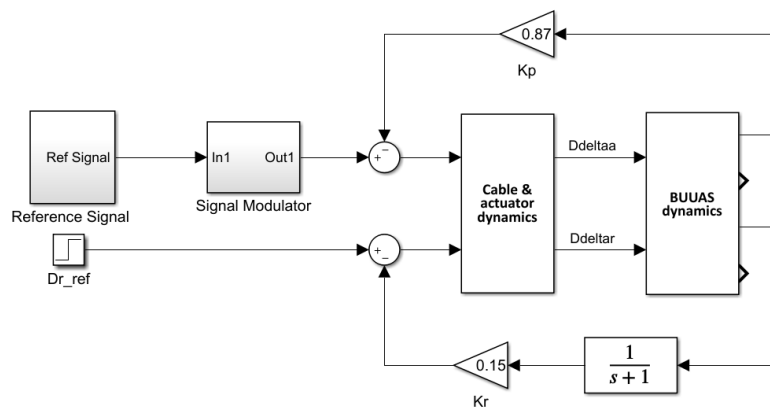


Figure 4.4-1: Model of the Roll Attitude Hold

RAH PROPORTIONAL GAIN	
$K_p$	0,87
$K_r$	0,15

*Table 4.4-1: Gain values of Roll Attitude Hold*

In the inner-feedback of the yaw-velocity there is a Washout filter that prevent the action of the control system at low frequencies, and so it allows the development of the spiral dynamic of the system.

The response of the lateral-directional system at an input signal (double steps) of bank angle  $p_{ref} = \pm 1 \text{ deg/s}$  is show in the Figure 4.4-2 and Figure 4.4-3.

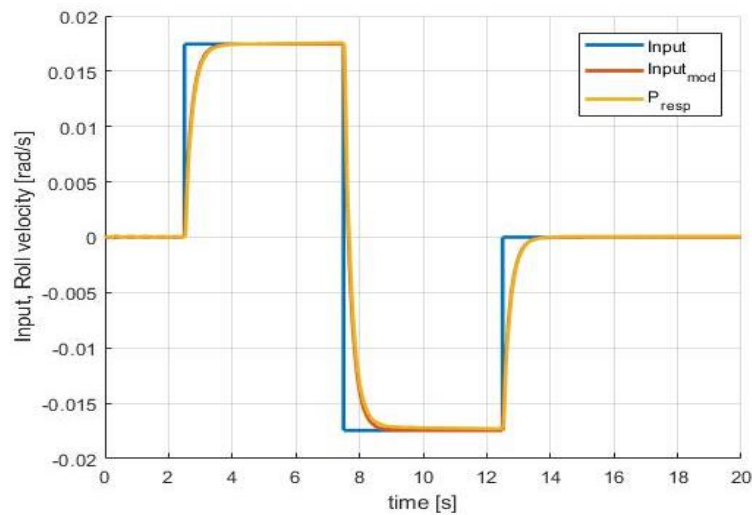


*Figure 4.4-2: Roll Attitude Hold: input ( $t = 5 \text{ sec}$ ) and response of the system*

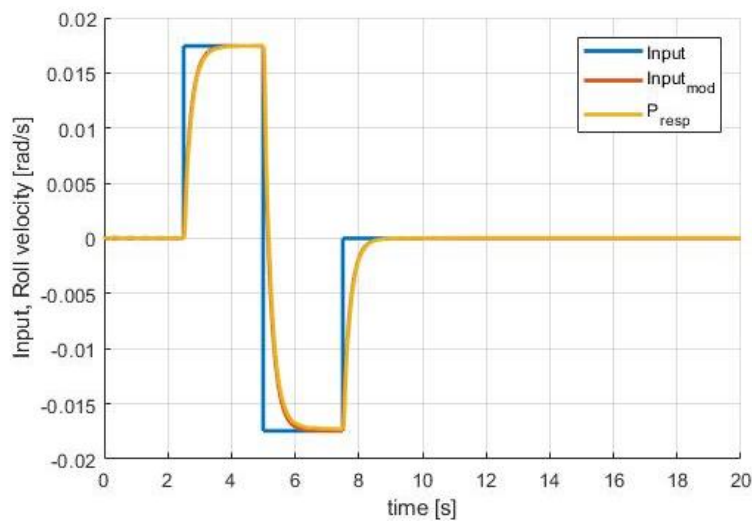


*Figure 4.4-3: Roll Attitude Hold: input ( $t = 2,5 \text{ sec}$ ) and response of the system*

## 4.5 Pitch Attitude Hold (PAH)

The PAH [14] is used to be an internal loop for other autopilot like AH (Altitude Hold) or AS (Altitude Select), that provide the pitch angle to follow. In this autopilot, the controlled variable is the pitch angle  $\theta$ . The block diagram of pitch attitude-hold autopilot is shown in Figure. A PI controller is implemented for this autopilot. For this controller the input signal is a simple step that is modulated by a second order transfer function. The transfer function (Eq. (33)) is been found considering the follow specification regarding the Time to rise  $t_r$  and the Peak of Overshoot  $M_p$  (Eq. (30) and Eq. (31)). These specifications in the time domain give specifications in the frequency domain that are possible to find with the formula before reported.

$$\begin{aligned}
 M_p = 5 \% & \rightarrow \zeta = 0,86 \\
 t_r = 2 \text{ sec} & \rightarrow \omega = 1,49 \\
 TF_{PAH} &= \frac{2,22}{s^2 + 2,563 s + 2,22}
 \end{aligned} \tag{33}$$

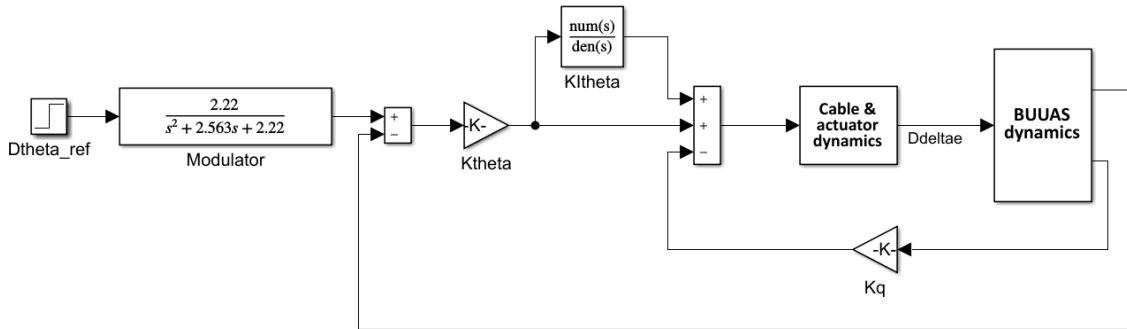


Figure 4.5-1: Pitch Attitude Hold: scheme of autopilot

PAH PROPORTIONAL GAIN	
$K_q$	-0,4
$K_\theta$	-0,85
PAH INTEGRATOR GAIN	
$K_{I\theta}$	1,2

Table 4.5-1: Pitch Attitude Hold: Gain values

For this analysis the lateral directional states have been fixed in order to investigate only the longitudinal dynamic and because the spiral instability could give some instability if it is not

controlled with the appropriate controller. The response of the longitudinal system at an input signal of pitch angle of  $\theta_{ref} = 1 \text{ deg}$  is shown in Figure 4.5-2.

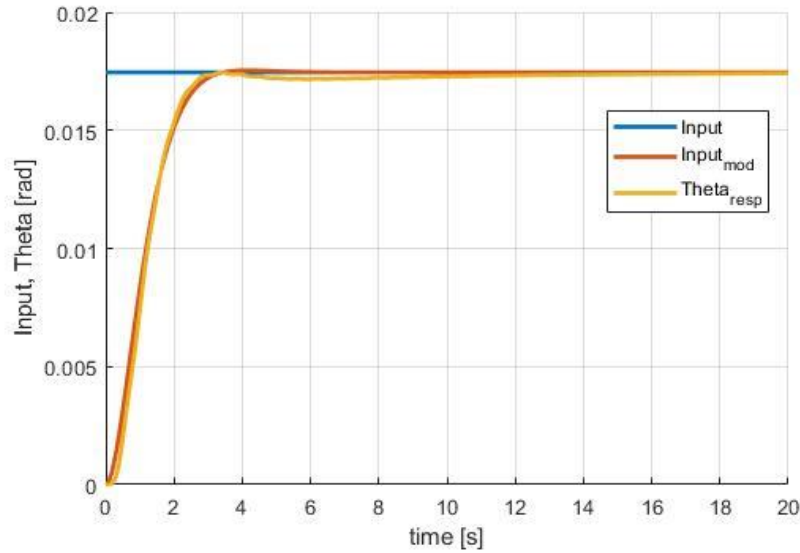
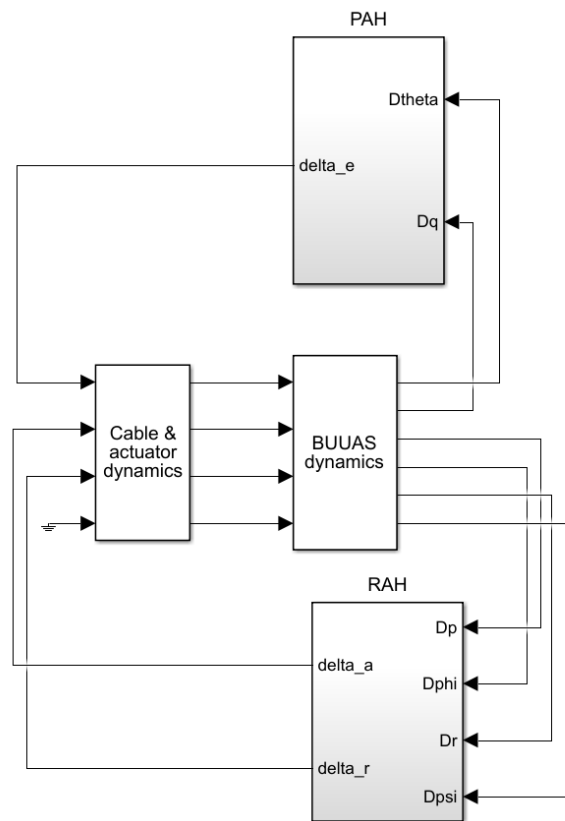


*Figure 4.5-2 Pitch Attitude Hold: input and response*

## 4.6 Non-Linear Simulation

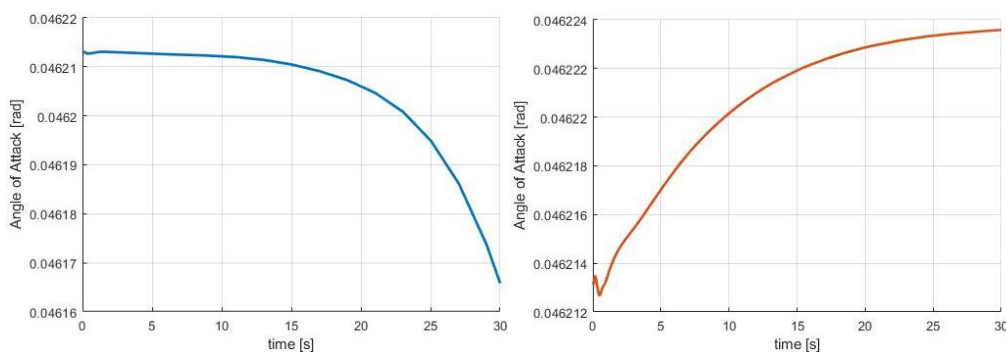
Found values of gains for PAH and RAH autopilots, the second stage of the control system is to evaluate the same autopilot with a nonlinear model of the aircraft aerodynamic, so with all states not fixed in order to show possible connection between the longitudinal and the later-directional dynamic. It is also possible to test the autopilots with larger amplitude maneuvers. So, the nonlinear model of the aircraft is used in place of the linear model. At first the nonlinear model is tested with a singular command of each controlled variables.

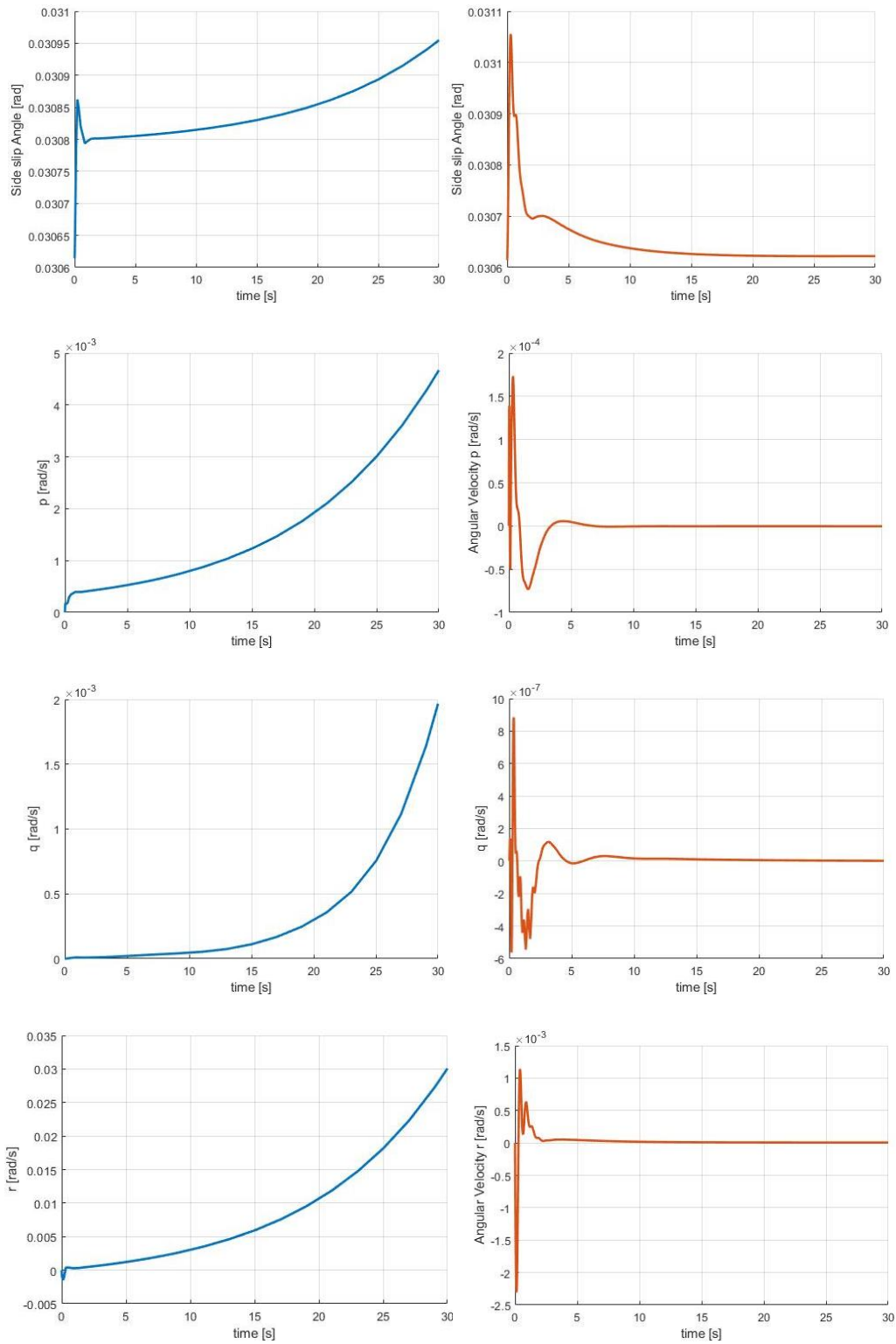




**Figure 4.6-1: PAH and RAH model**

The results of the different input for PAH and RAH autopilots are shown below. At first a confront of the trimmed condition is done between the model with and without autopilots. Particular attention is put on the graphics of roll and yaw velocity: in the simulation without autopilots, the variation of these variables is very slow, but the evolution is not convergent as in results with the autopilots.





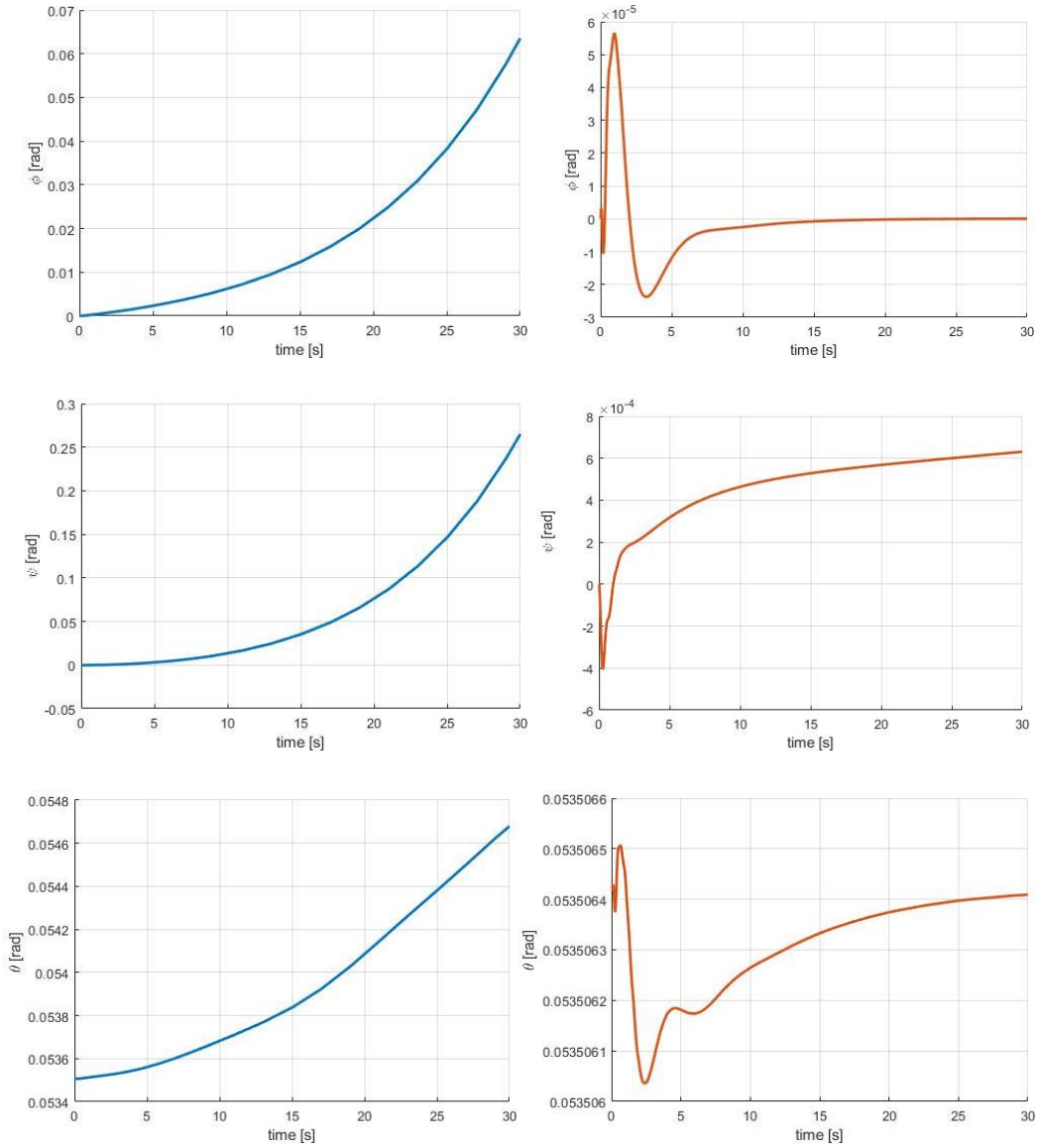


**Figure 4.6-2: Trim Condition: results comparison between simulation with(right) and without(left) autopilots**

The PAH is tested with a reference signal of  $\theta_{ref} = 1 \text{ deg}$ , and the RAH is tested with a double steps input of amplitude  $p = \pm 1 \text{ deg/s}$  and duration of  $t = 5 \text{ sec}$ . Below, results for the different input are presented, making a comparison with results obtained before when the longitudinal or the lateral-directional dynamic have been fixed in the different autopilots. Because all states are not fixed a new tuning of gains for each autopilot have been done. New gains for the PAH and RAH are presented in the Table 4.6-1.

RAH PROPORTIONAL GAIN	
$K_p$	0,87
$K_r$	0,95

PAH PROPORTIONAL GAIN	
$K_q$	-0,5
$K_\theta$	-0,85
PAH INTEGRATOR GAIN	
$K_{I\theta}$	1,35

*Table 4.6-1: Non-linear simulation: RAH and PAH gains*

In Figure 4.6-3 and Figure 4.6-4 the results for test of RAH and PAH are presented.

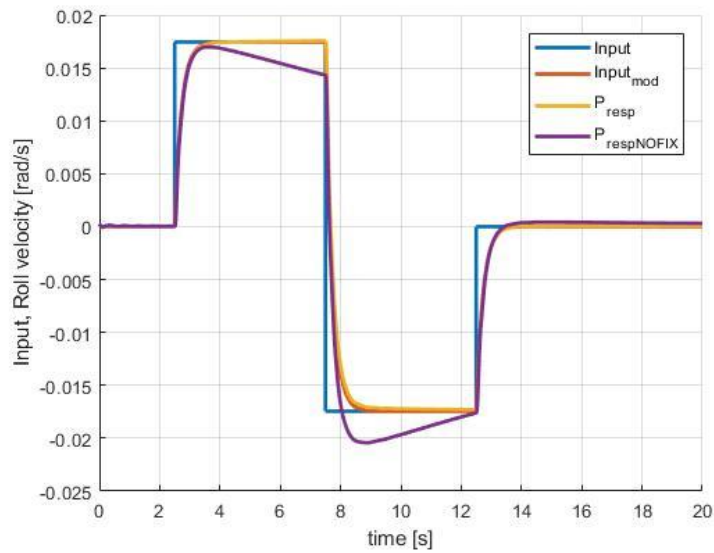


*Figure 4.6-3: Non-linear simulation: Roll velocity response*

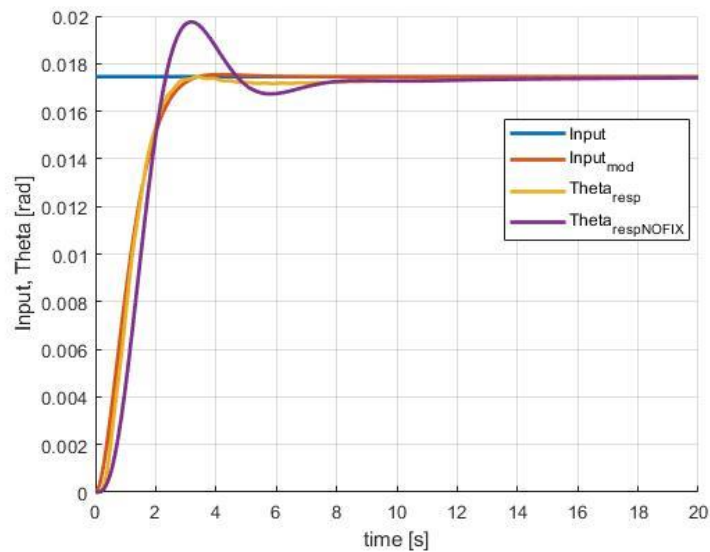


*Figure 4.6-4: Non-linear simulation: Theta response*

It is possible to observe that, because all the states are not fixed and both the autopilots are active, the response of the system is different and less exact. For this reason, a new tuning of gains of the autopilots are necessary when more than one is active.

Other autopilots like AH (Altitude Hold autopilot), AS (Altitude Select autopilot), IAH (Mach Attitude Hold autopilot) and Heading-angle-Hold system are implemented and tested with the nonlinear model of the aircraft's dynamic. These autopilots represented the outer-loop of the previous controller (PAH and RAH).

#### 4.7 Altitude Hold/Altitude Select

Important autopilots, for the longitudinal motion control, are AH (Altitude Hold) and AS (Altitude Select). They can not be used together, so when once is active the other must to be off. Emphasis is on the switch of these two autopilots because they use different variables: during the switch, if the elevator deflection command from an autopilot is very different, a perturbation can bring the vehicle in an instable condition.

The Altitude Hold uses as variables the altitude and the derivation of the altitude (climb velocity). The output is a reference pitch angle that will be used by the Pitch Attitude Hold autopilot. Below, in Figure 4.7-1, Simulink diagram of this autopilot is shown.

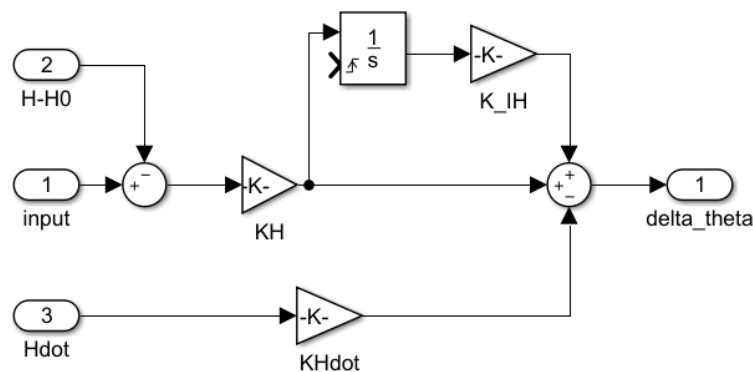


Figure 4.7-1: Altitude Hold's Simulink scheme

Values of gains for this autopilot are shown in Table 4.7-1:

AH PROPORTIONAL GAIN	
$K_{h\dot{}}$	0,15
$K_h$	0,045
AH INTEGRATOR GAIN	
$K_{Ih}$	0,09

*Table 4.7-1: Altitude Hold's gain*

In the Figure 4.7-2 are presented the results for an input of  $\Delta H = 1 \text{ m}$ . In this case, also, the input signal is filter with a modulator that is characterized by a time constant of  $t = 5,5 \text{ sec}$ .

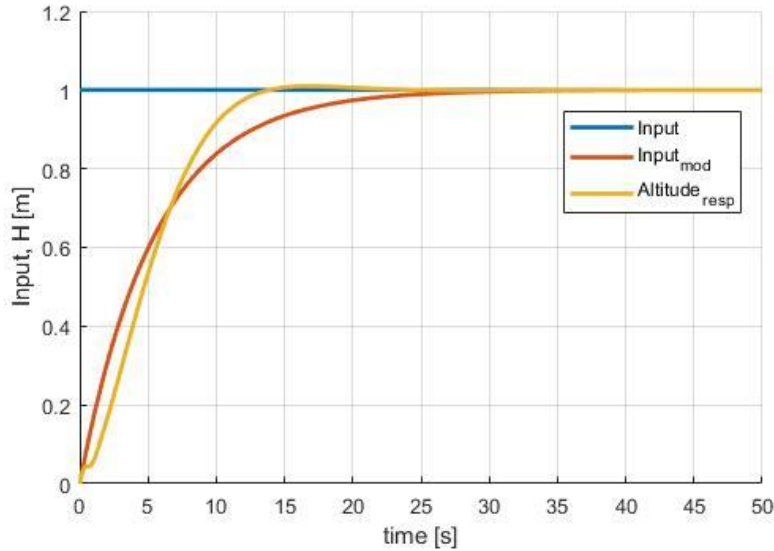


*Figure 4.7-2: Altitude Hold response*

For the Altitude Select autopilot (AS), variables are the flight path  $\gamma$  and the angle of attack  $\alpha$ . This autopilot provides as output a reference pitch angle  $\theta$  that will be used by the PAH autopilot.

Below, in the Figure 4.7-3, the Simulink diagram of this autopilot is shown. For the Altitude Select autopilots a first order transfer function is been introduced in order to carry out a modulation of the input signal. The time constant of this transfer function (Eq. (34)) is  $t = 5,5 \text{ sec}$ .

$$TF_{AS} = \frac{1}{5,5 s + 1} \quad (34)$$

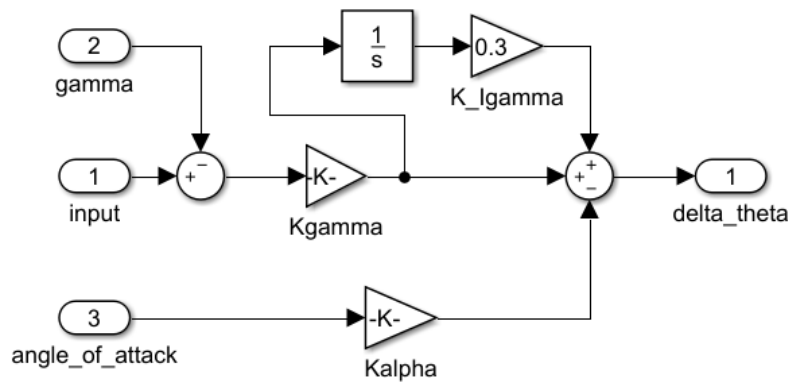


Figure 4.7-3: Altitude Select's Simulink scheme

Values of gains for this autopilot are shown in Table 4.7-2:

AS PROPORTIONAL GAIN	
$K_{\gamma}$	0,95
$K_{\alpha}$	0,35
AS INTEGRATOR GAIN	
$K_{I\gamma}$	0,3

Table 4.7-2: Altitude Select gain

The results for this autopilot to a input of  $\gamma = 1 \text{ deg}$  are presented in Figure 4.7-4.

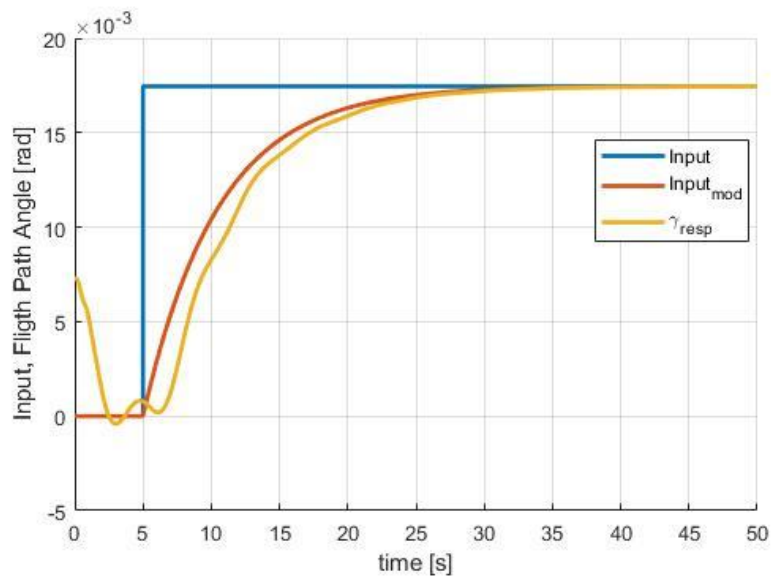


Figure 4.7-4: Altitude Select response

When these autopilots, AS and AH, are active also the IAS hold must be active because the change of the pitch angle should take the aircraft at a different acceleration, so to change the velocity. For this reason, a controller for the velocity is necessary to allow the correct operation of the autopilots.

## 4.8 IAS Hold

The Indicated Airspeed Hold autopilot is used when the AH (Altitude Hold) or the AS (Altitude Select) are active. For most of the vehicle the Mach Hold autopilot is used of this controller, because the BUUAS is a small vehicle and the maximum Mach number that is possible to realized is  $M = 0,08$ , the variation of the Mach number could be not very significant, so another autopilots it is necessary to implement. Moreover, sensor used to calculate the Mach number, like the pitot tube, could not be used for the BUUAS vehicle because of the underwater phase. The IAS Hold is used to control the velocity of the vehicle and this volume should be take by the signal of the differential GPS that is mounted on the vehicle. The output of this autopilot is the different number of revolutions per minutes that will be commanded to the electric motor block. It will provide a constant velocity.

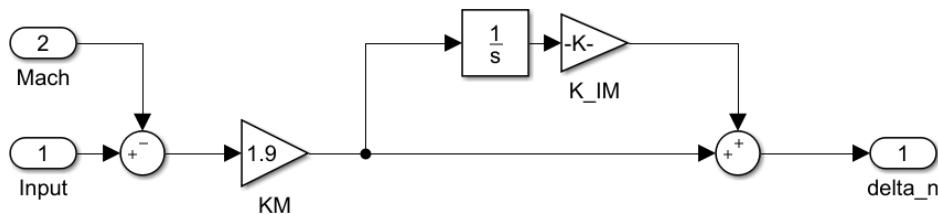


Figure 4.8-1: Speed Hold's Simulink scheme

Values of gains for this autopilot are shown in Table 4.8-1:

MACH HOLD GAIN	
$K_S$	0,5
MH INTEGRATOR GAIN	
$K_{IS}$	0,9

Table 4.8-1: Speed Hold gain



For this autopilot, results of a simulation with an input of constant speed of  $V = 24 \text{ m/s}$  are presented in Figure 4.8-2.

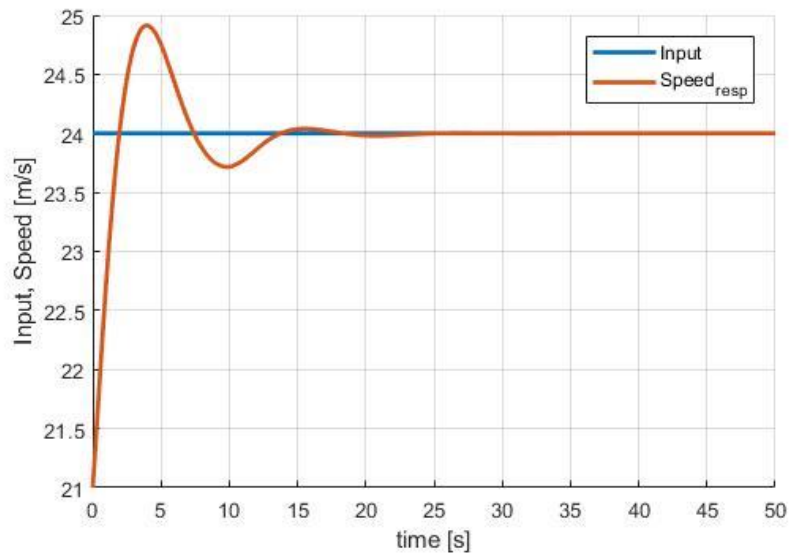


**Figure 4.8-2: IAS-Hold results**

## 4.9 Heading Angle Hold System

The heading-angle-hold system is used to implemented autopilots like the VOR-hold, so it is very important for the navigational modes. Like input, it receives a heading angle to follow and with the turn compensation conditions it is confronted with the roll angle; it is processed finally by the PAH and it gives an input deflection for ailerons and rudder. The scheme of the autopilot is show in Figure 4.9-1.

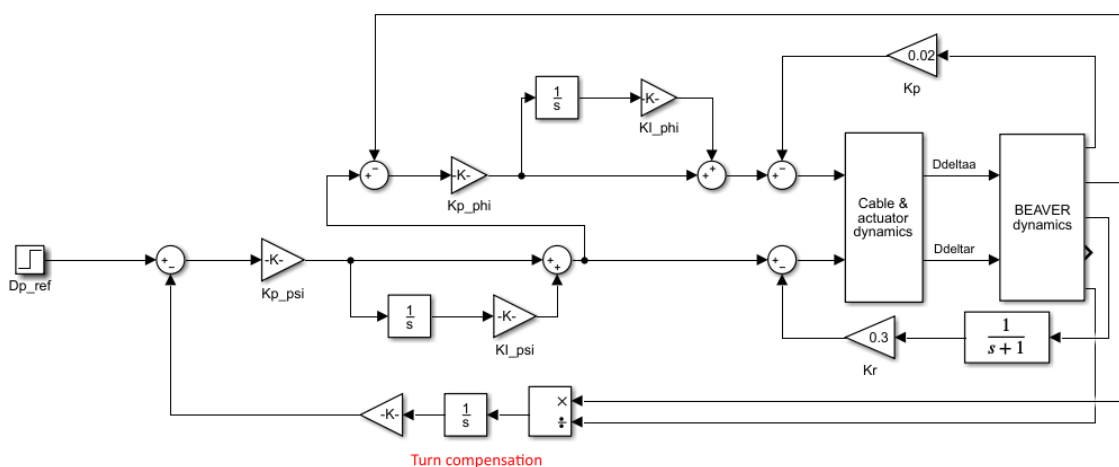


**Figure 4.9-1: Heading Hold System's Simulink scheme**

Values of gains for this autopilot are shown in Table 4.9-1:

HEADING ANGLE HOLD GAIN	
$K_{P\phi}$	1,2
$K_{I\phi}$	0,8
$K_{P\psi}$	1,25
$K_{I\psi}$	-0,01

*Table 4.9-1: Heading Angle Hold gain*

The result for an input of  $\psi = 1 \text{ deg}$  is presented in Figure 4.9-2 and Figure 4.9-3.

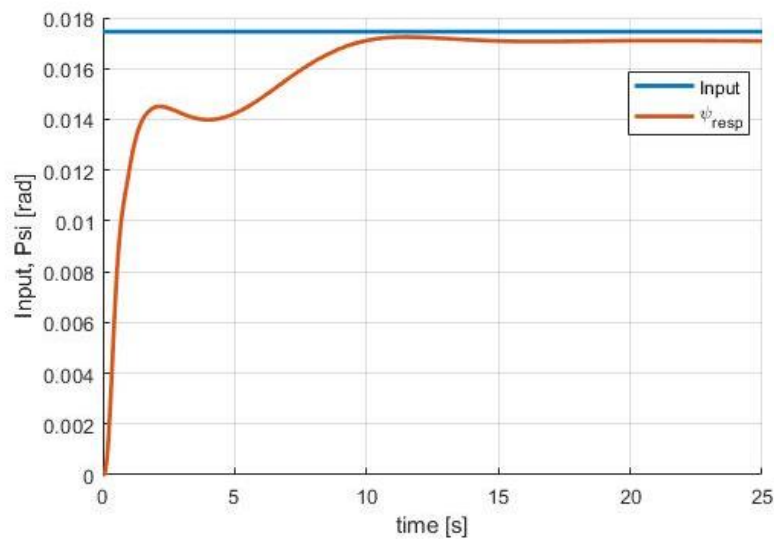


*Figure 4.9-2: Heading Angle Hold response:  $\psi$*

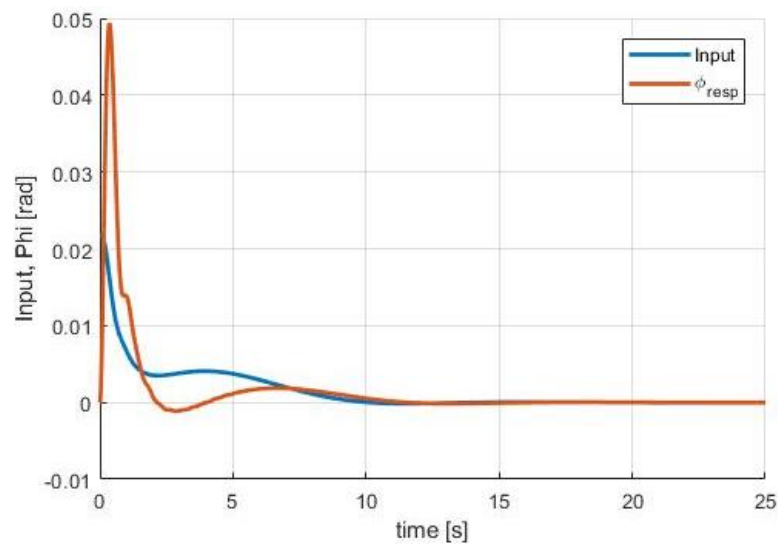


*Figure 4.9-3: Heading Angle Hold:  $\phi$*

# Chapter 5: Tail Issue

---

During the first experimental test in the wind tunnel test, the vehicle has been tested with a fixed tail, so the derivatives respect to the tail have been calculated with formulas, considering geometry dimensions. New experimental tests have been done with a moving tail in order to obtain the right derivatives.

## 5.1 Geometric Derivatives

The dihedral angle of the wing conditions the lateral force and so also the Rolling and Yaw moment [15] when a side-slip angle  $\beta$  is present. If the tail has a dihedral or anhedral (negative dihedral) angle, this will influence the derivatives of  $C_Y$ ,  $C_l$  and  $C_n$ . In fact, due to the substantial anhedral angle for the horizontal tail, a non-negligible lateral force will be generated by the lateral flow on the horizontal tail. This effect is possible to see on the Figure 5.1-1. At first, these derivatives ( $C_{Y\beta_H}$ ,  $C_{l\beta_H}$  and  $C_{n\beta_H}$ ) are been obtain follow the formulation presented by the theoretical 'Aircraft Dynamic From Modelling to Simulation of Marcello R. Napolitano [16].

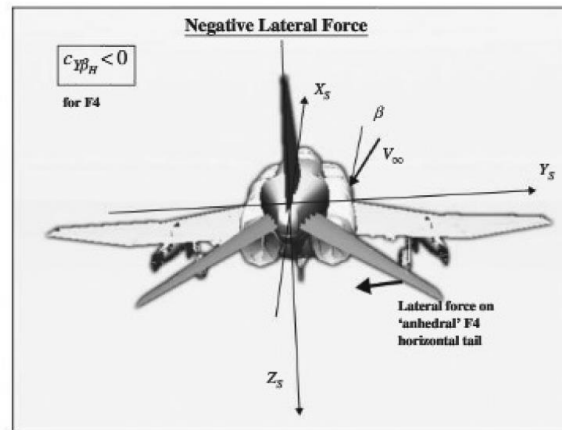


Figure 5.1-1: Lateral Force on the Horizontal Tail of the F-4 associated with  $\beta$  [17]

The derivatives are founded with the Eq. (35):

$$C_{Y\beta_H} \approx -0,0001 |\Gamma_H| 57,3 \eta_H \left(1 + \frac{d\sigma}{d\beta}\right) \frac{S_H}{S} [rad^{-1}] \quad (35)$$

Where:

- $\Gamma_H$  is the anhedral angle of the tail
- $\eta_H \left(1 + \frac{d\sigma}{d\beta}\right)$  follow the empirical relationship (Eq. (36))
- $S_H$  is the surface of the tail
- $S$  is the reference surface of the wing

$$\eta_H \left(1 + \frac{d\sigma}{d\beta}\right) = 0,724 + 3,06 \frac{\frac{S_H}{S}}{1 + \cos\left(\frac{\Lambda_c}{4}\right)} + 0,4 \frac{Z_W}{d} + 0,009 AR \quad (36)$$

The final result of this derivate is:

$$C_{Y\beta_H} = -6,0346 \cdot 10^{-4} [rad^{-1}] \quad (37)$$

Regarding to the Rolling moment, the anhedral angle generates a substantial positive  $C_{l\beta_H}$  effect, which compensates for the excessively large negative value for the  $C_{l\beta_{WB}}$  coefficient.

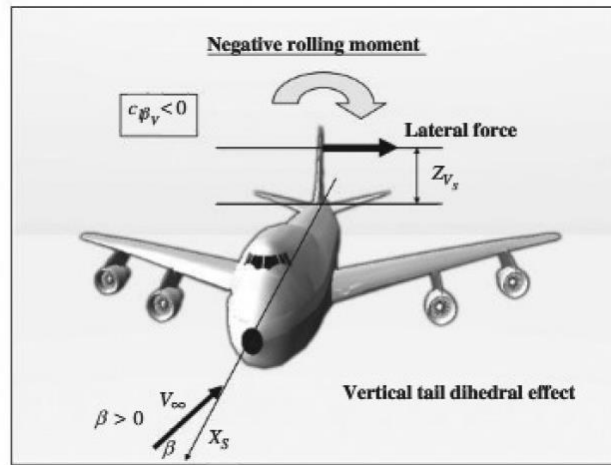


Figure 5.1-2: dihedral Effect for the Vertical Tail [18]

To find the coefficient  $C_{l\beta_H}$  the Eq. (38) is used:

$$C_{l\beta_H} = C_{l\beta_{WB}}|_H \eta_H \frac{S_H}{S} \frac{b_H}{b} \quad (38)$$

Where  $C_{l\beta_{WB}}$  is

$$C_{l\beta_{WB}} = 57,3 C_{L1} \left[ \left( \frac{C_{l\beta}}{C_{L1}} \right) K_{M\Lambda} K_f + \left( \frac{C_{l\beta}}{C_{L1}} \right)_{AR} \right] + 57,3 \left\{ \Gamma_W \left[ \frac{C_{l\beta}}{\Gamma_W} K_{M\Gamma} + \frac{\Delta C_{l\beta}}{\Gamma_W} \right] + (\Delta C_{l\beta})_{ZW} + \epsilon_W \tan \Lambda_{\frac{c}{4}} \left( \frac{\Delta C_{l\beta}}{\epsilon_W \tan \Lambda_{\frac{c}{4}}} \right) \right\} \quad (39)$$

Where:

- $\left( \frac{C_{l\beta}}{C_{L1}} \right)$  represent contribution associated with the wing sweep angle;
- $K_{M\Lambda}$  is a correction factor associated with the Mach number and the wing sweep angle;
- $K_f$  is a correction factor associated with the length of the forward portion of the fuselage;
- $\left( \frac{C_{l\beta}}{C_{L1}} \right)_{AR}$  represents the contribution associated with the wing aspect ratio;
- $\frac{C_{l\beta}}{\Gamma_W}$  represents the contribution associated with the wing dihedral angle;
- $K_{M\Gamma}$  is a correction factor associated with the Mach number and the wing dihedral angle;
- $\frac{\Delta C_{l\beta}}{\Gamma_W}$  is a correction factor associated with the size of the fuselage modeled using Eq. (40).

$$\frac{\Delta C_{l\beta}}{\Gamma_W} = -0,0005 AR \left( \frac{d_B}{b} \right)^2 \quad (40)$$

All these coefficients are diagrammed in a different graphic reported in appendix A.

Returning to the coefficient  $C_{l\beta_H}$ , the coefficient  $C_{l\beta_{WB}}|_H$  is the previously introduced for the wing, evaluated with the geometric parameters of the horizontal tail.

The final result of this derivate is:

$$C_{l\beta_H} = 0,0077 \left[ \frac{1}{rad} \right] \quad (41)$$

## 5.2 Wind Tunnel Test

In order to obtain coefficients relative to the influence of the anhedral angle of the tail on forces and moments for the longitudinal and lateral directional motion of the vehicle, wind tunnel test has been done. The full-scaled vehicle has been tested in the wind tunnel using a movable tail and rudder. The test has been done for different pitch angles and sweep angles for three different angles of the equilibrator. For the test, the RMIT industrial wind tunnel and JR3 400N load cell have been used. Below, in Figure 5.2-1, shows the set-up of the vehicle and the load cell.

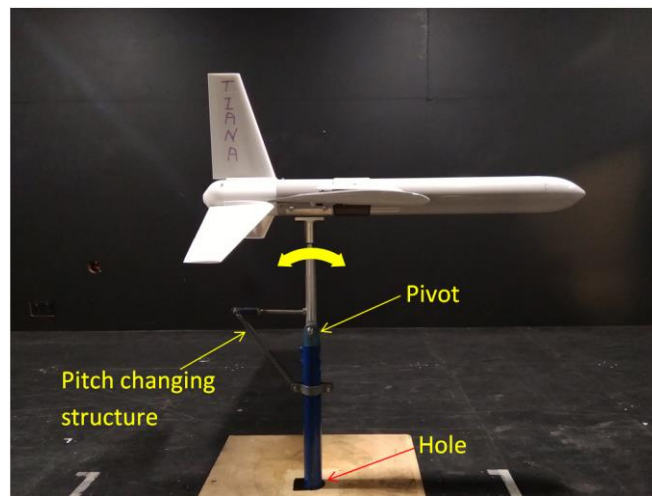


*Figure 5.2-1: Wind Tunnel set up [19]*

The vehicle has been fixed on the top of the sting, while the bottom of the sting has been fixed on the load cell under the wind tunnel floor. The load cell, as illustrated in Figure 5.2-2, has been mounted on a steel plate, which has been placed on the basement and fixed rigidly by the clamps. The pitch angle has been modified through a hinge and a triangular rod supporting structure on the sting above the wind tunnel floor. The yaw angle has been set beside the floor, aligning the sting with the protractor.



*Figure 5.2-2: Detail of Wind tunnel set up [20]*

The vehicle has been fixed with the sting using an aluminium cylinder put into the fuselage and clamped in the middle tightly by the cylinder, curved plate and flange mount, which have been fixed using screws (see Figure 5.2-3).

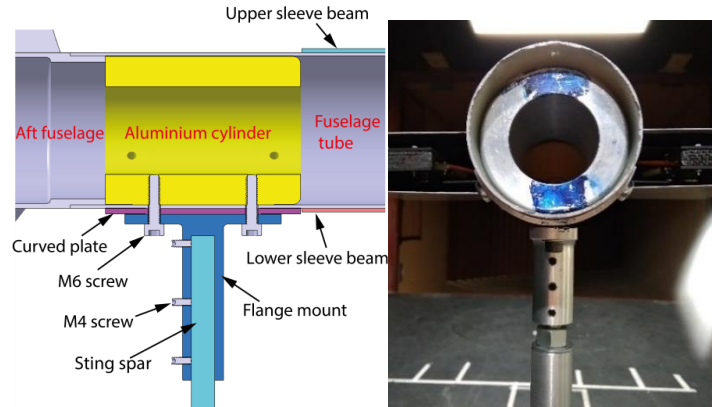


Figure 5.2-3: Wind tunnel set up: cylinder inside the fuselage [21]

Angles of the equilibrator have been measured with a protractor, positioned on the tail and moving the tail with a controller, in order to obtain the right angles. Angles tested were:  $\Delta d_e = \pm 5^\circ, \pm 10^\circ, \pm 15^\circ$ . These angles of equilibrator have been tested for different configuration of pitch angle and sweep angle and for four different wind velocity that it's possible to see in Table 5.2-1. The wind velocity is modified acting on a knob of the revolution per minutes of the fan of the wind tunnel.

VELOCITY						
$V = 10 \text{ [m/s]}$		$V = 15 \text{ [m/s]}$		$V = 20 \text{ [m/s]}$		$V = 25 \text{ [m/s]}$
ANGLE OF ATTACK						
$\alpha = -6^\circ$	$\alpha = -3^\circ$	$\alpha = 0^\circ$	$\alpha = 3^\circ$	$\alpha = 6^\circ$	$\alpha = 9^\circ$	$\alpha = 11^\circ$
SWEEP ANGLE						
$\beta = 0^\circ$	$\beta = 3^\circ$	$\beta = 6^\circ$	$\beta = 9^\circ$	$\beta = 12^\circ$	$\beta = 15^\circ$	

Table 5.2-1: Velocity, Pitch Angle and Sweep Angle tested during the wind tunnel tests

The load cell gives a measurement of the loads and the moments for three axes. They are positioned in the way show in the Figure 3.3-7. Because the load cell has not been placed in the same position of the center of gravity of the vehicle, a correction of the results it is necessary.

### 5.3 Results of the Wind Tunnel Test

Results of the wind tunnel test have been analyzed in order to obtain the right derivatives of loads and moments reference to a different angle of the equilibrator. The analysis has been done considering the separation of the longitudinal and lateral direction motion. Because the trimmed condition is found for a velocity of  $V = 21 [m/s]$ , the derivates have been also found for this velocity. Coefficients of all the loads and moments have been found for different angle of equilibrator. Then all these coefficients have been put in a graphic in order to put in evidence the variation of the coefficient for different equilibrator angles. Below the results are shown in Figure 5.3-1 – 5.3-2 – 5.3-3.

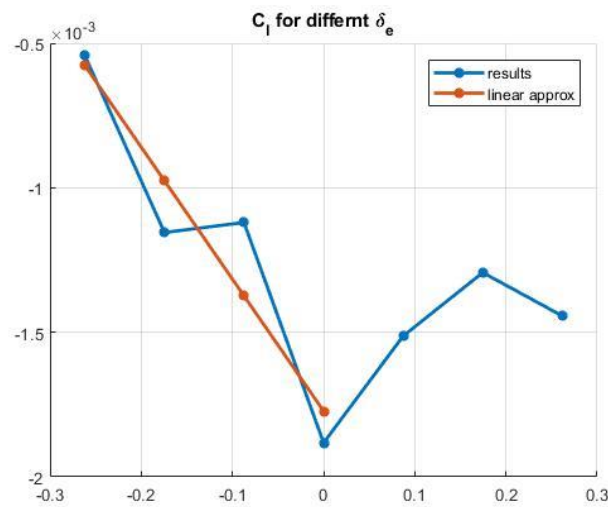


Figure 5.3-1: Distribution and Approximation of  $C_l$  for different Equilibrator's angles

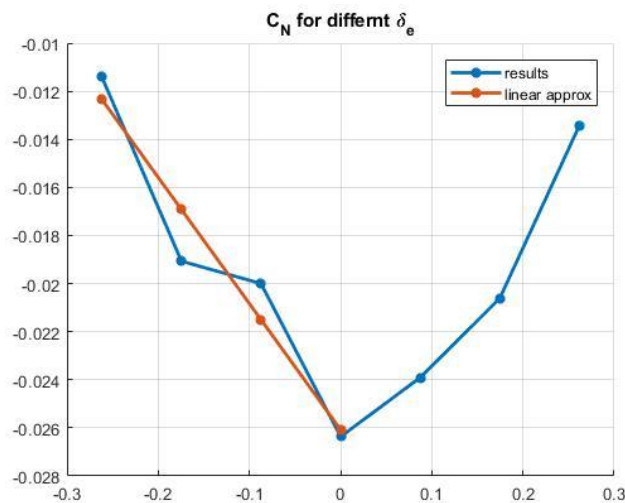
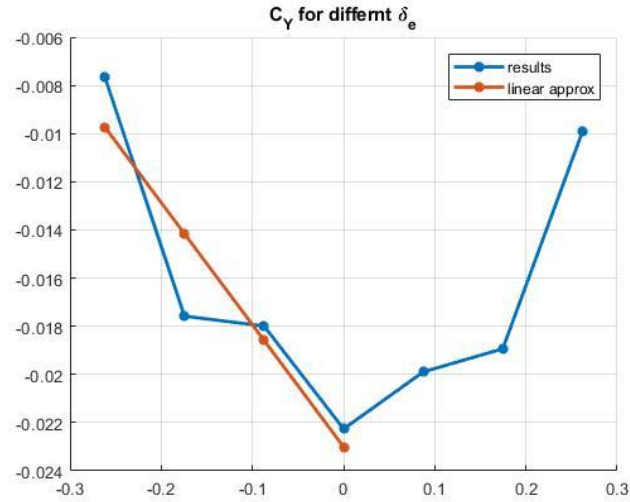


Figure 5.3-2: Distribution and Approximation of  $C_N$  for different Equilibrator's angles





*Figure 5.3-3: Distribution and Approximation of  $C_Y$  for different Equilibrator's angles*

As it's possible to see, in Figure 5.3-1 – 5.3-2 – 5.3-3, is represented the evolution of the coefficient  $C_l$ ,  $C_n$  and  $C_Y$  for different equilibrator angles. In the figure there are also the linear approximation of the curve that it's considered as input for the aerodynamic model for the simulator.

Values of the coefficients are below presented:

$$C_{l_{\delta_e}} = 0,0046$$

$$C_{n_{\delta_e}} = -0,0525$$

$$C_{Y_{\delta_e}} = 0,0525$$

In Figure 5.3-4 – 5.3-5 – 5.3-6, the evolution of the coefficients  $C_{l_{\beta}}$ ,  $C_{n_{\beta}}$  and  $C_{Y_{\beta}}$  are represented for different angle of equilibrator.

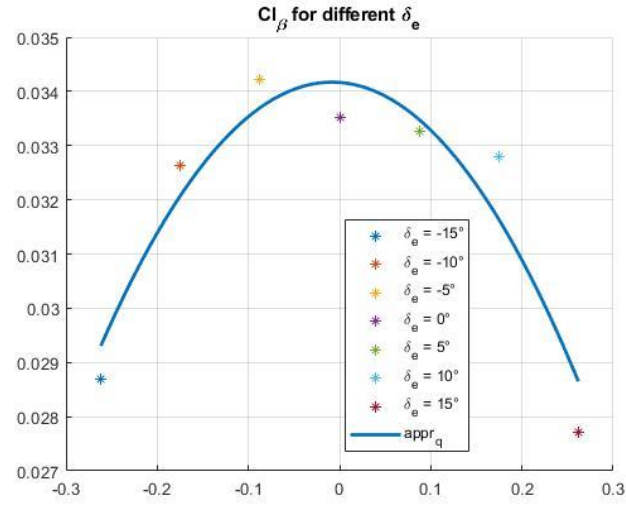


Figure 5.3-4: Distribution and Approximation of  $C_{l_{\beta}}$  for different Equilibrator's angles

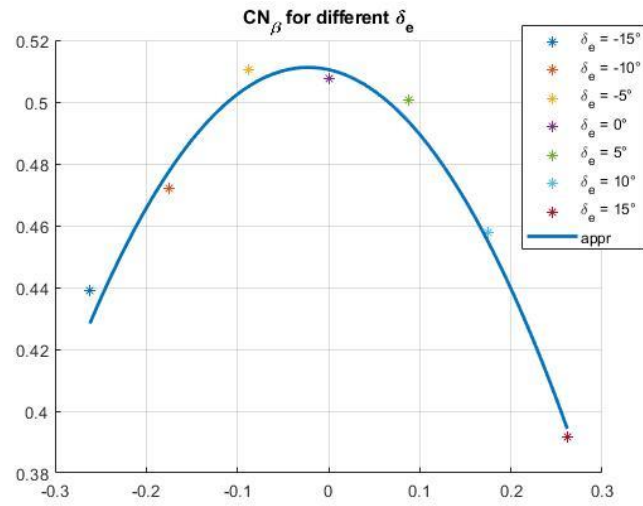
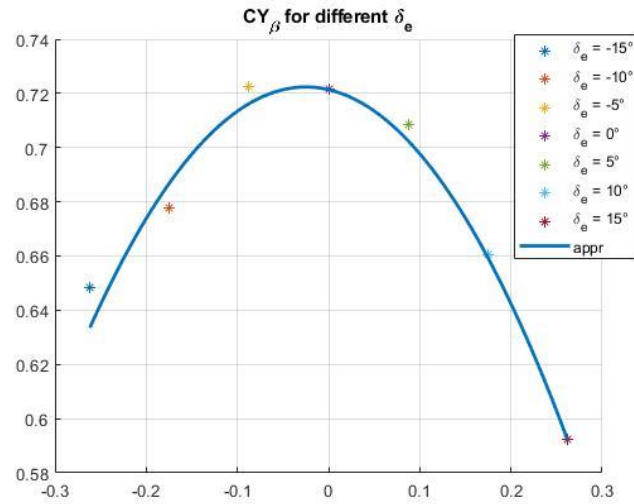


Figure 5.3-5: Distribution and Approximation of  $C_{N_{\beta}}$  for different Equilibrator's angles



**Figure 5.3-6: Distribution and Approximation of  $C_{Y\beta}$  for different Equilibrator's angles**

Also for this coefficients an approximation is founded and follow presented:

$$C_{l\beta_{\delta_e}} = -0,0316$$

$$C_{n\beta_{\delta_e}} = 0,5175$$

$$C_{Y\beta_{\delta_e}} = -0,545$$

# Chapter 6: Deploying of wings

## 6.1 Dynamic of Deploying

A crucial phase of the mission profile is when the aircraft jump out of the water in order to start the air-phase. In this phase there are two issues: the transition propulsion system, used to jump out of the water, is composed with a high pressure gas of CO<sub>2</sub> that push out water from the water chamber; the transition between the water and air configuration of the aircraft is made with the deploying of the wing as shown in the first Chapter. The first issue has been studied by Dian Guo [22] in order to define if the dimension of the transition propulsion is correct. In order to study the dynamic of the deploying a wind tunnel test has been done. Different pitch and of side-slip angles have been tested to find the dynamic of longitudinal and lateral direction motion for different angle of opening of the wing. The angle of opening of the wing are shown in the Figure 2.1-2.

Below the root loci of the longitudinal and lateral-directional dynamic for the different sweep angle of the wing are shown in Figure 6.1-1 and Figure 6.1-2.

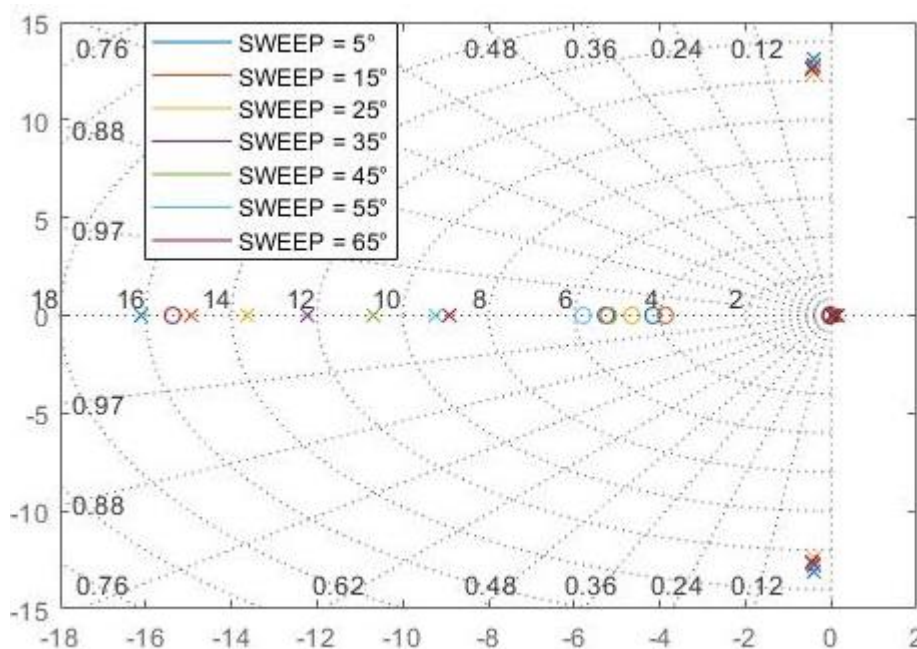


*Figure 6.1-1: Root Loci Longitudinal dynamic for different sweep angle*

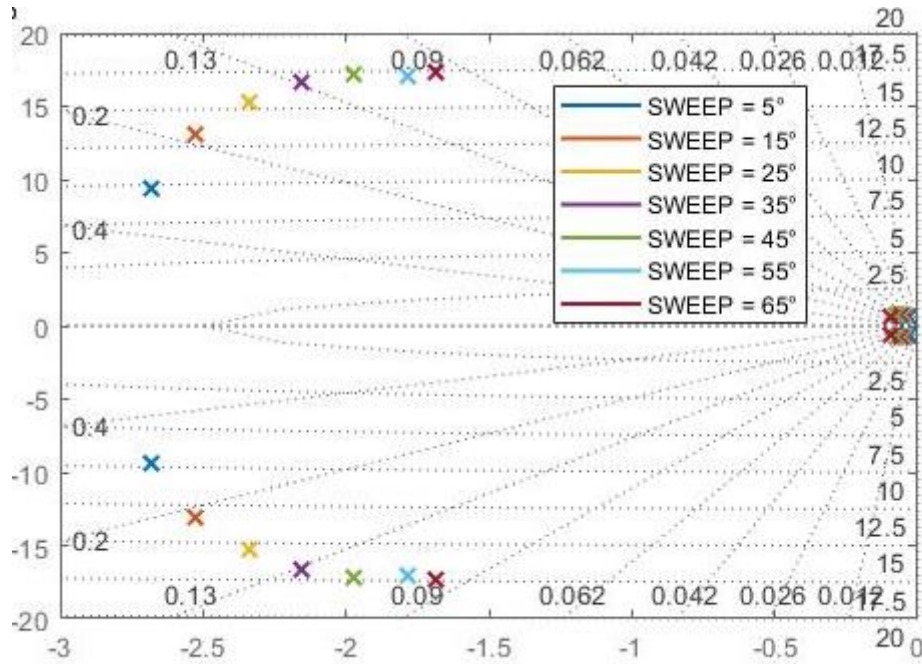


*Figure 6.1-2: Root Loci Longitudinal dynamic for different sweep angle*

It is possible to see that for the lateral direction dynamic, for the maximum angle of opening of the wing (water configuration of the aircraft), the dynamic is more unstable and slower than the full opening configuration (air configuration). For the longitudinal dynamic is possible to see that also for the water configuration the longitudinal motion is stable but slower and the less damping in reference to the aircraft configuration.

To test the dynamic of the deploying of the wing a dynamic model for each angle of wing's opening has been built with the results of the wind tunnel tests. In the simulation a MATLAB® function is used to change the different dynamic according to different time of the opening. For this reason, a test of the deploying has been done in order to establish the time of the opening: as result the time of full deploy is around  $t = 1,2 \text{ s}$ . Because there are seven different sweep angles tested in the wind tunnel, the change of the dynamic for the simulation is done each  $\Delta t = 0,1784 \text{ s}$ . The Figure 6.1-3 show the Simulink diagram for the change of the dynamic model used during the simulation. Because of the interesting dynamic is of the first seconds of the simulation, the duration of the simulation is of the  $T = 10 \text{ s}$ , and as solver a Fixed-step based on the ode4 (Runge-Kutta) with a sample time of  $\Delta t = 10^{-4} \text{ s}$ .

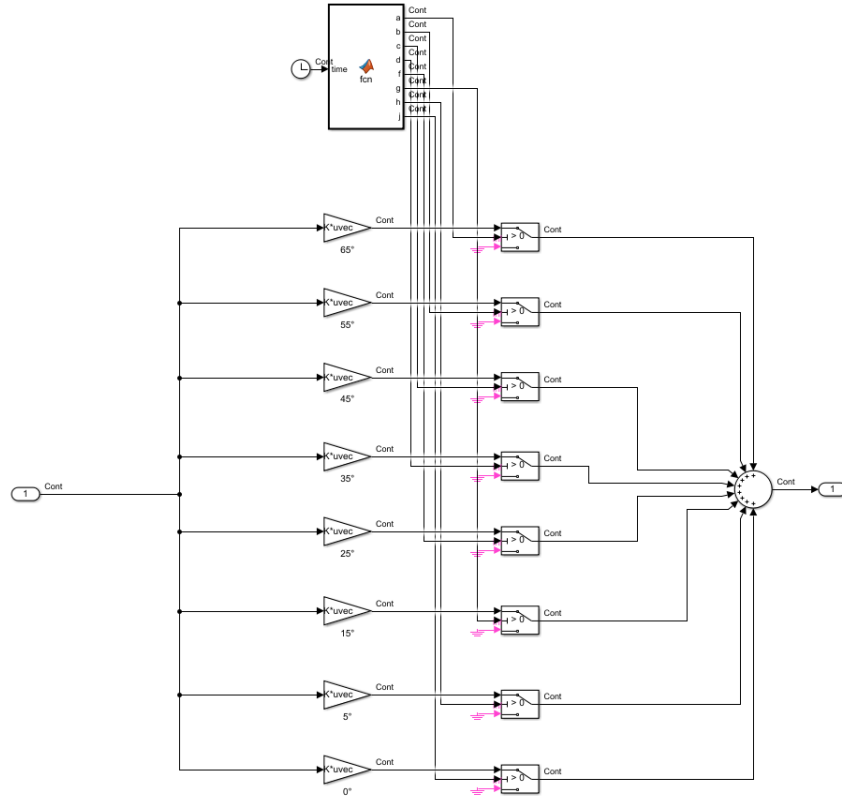
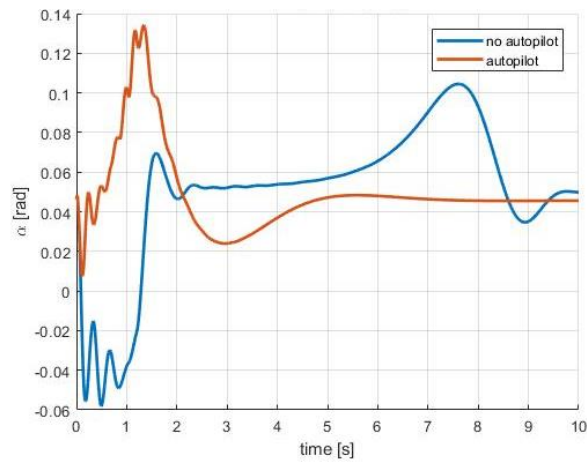


**Figure 6.1-3: Simulink scheme to change dynamic for different sweep angle**

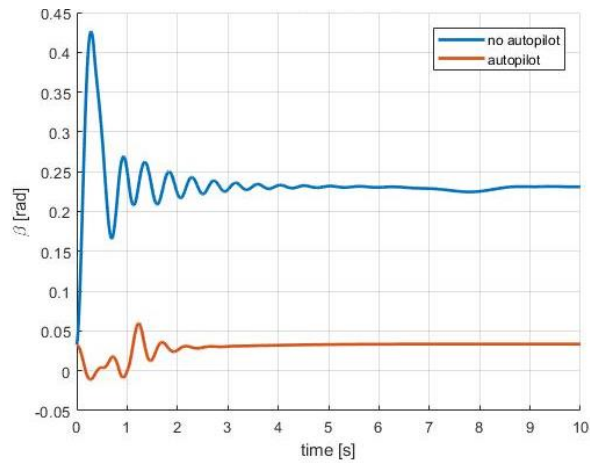
The model is tested without and with the autopilot in order to know if gains of the autopilot give a stable dynamic. The Figure 6.1-4 to Figure 6.1-12 show the different variables for the two different simulation. The simulation has been done with the follow initial condition:

$$V = 21 \text{ m/s}$$

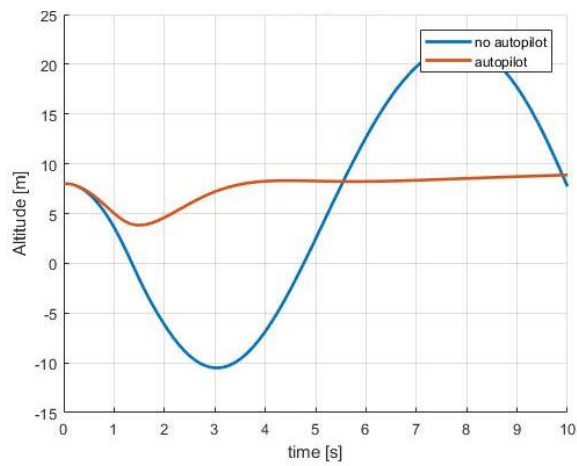
$$H = 8 \text{ m}$$



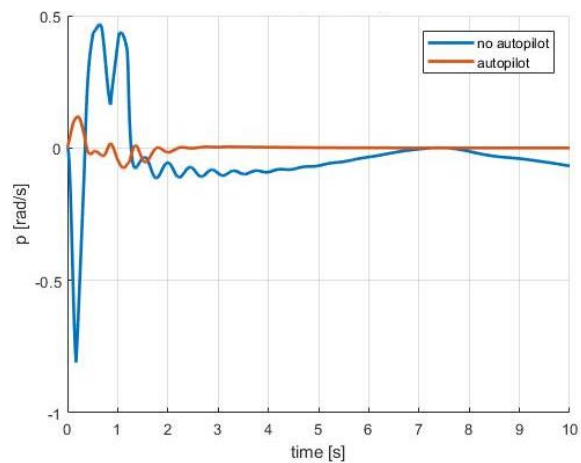
**Figure 6.1-4: Deploying of the wing: Angle of attack with and without autopilots**



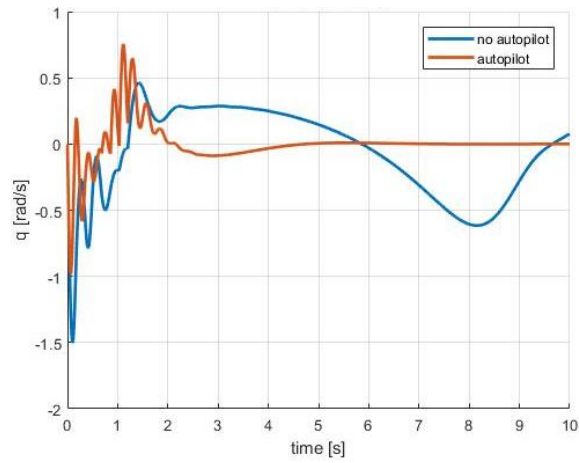
**Figure 6.1-5: Deploying of the wing: Side Slip Angle with and without autopilots**



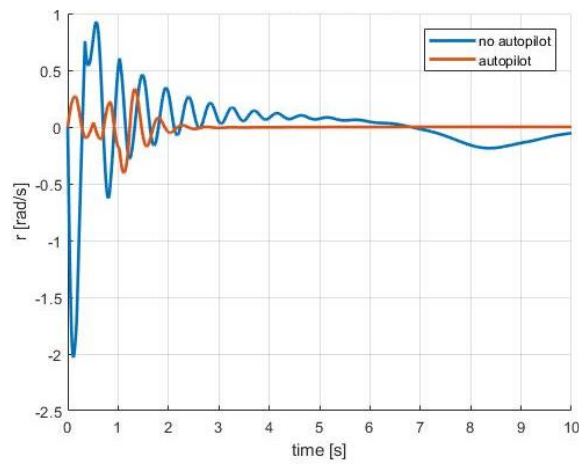
**Figure 6.1-6: Deploying of the wing: Altitude with and without autopilots**



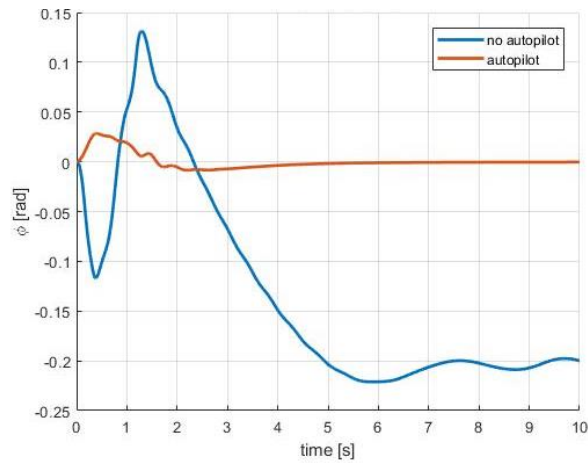
**Figure 6.1-7: Deploying of the wing: Roll velocity with and without autopilots**



**Figure 6.1-8:Deploying of the wing: Pitch velocity with and without autopilots**

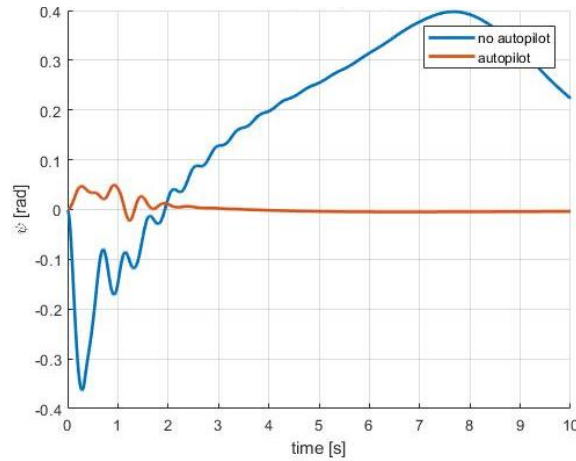


**Figure 6.1-9:Deploying of the wing: Yaw velocity with and without autopilots**

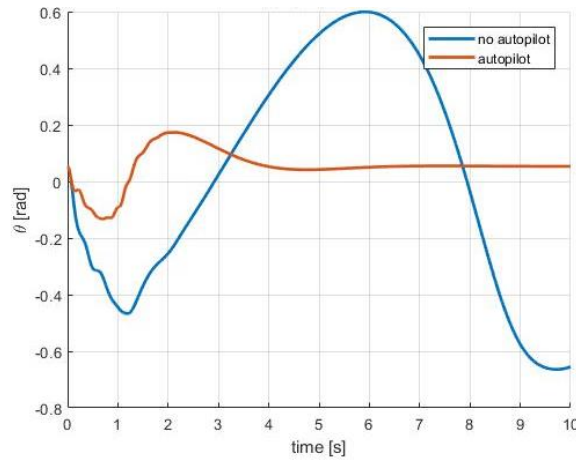


**Figure 6.1-10: Deploying of the wing:  $\phi$  Angle with and without autopilots**





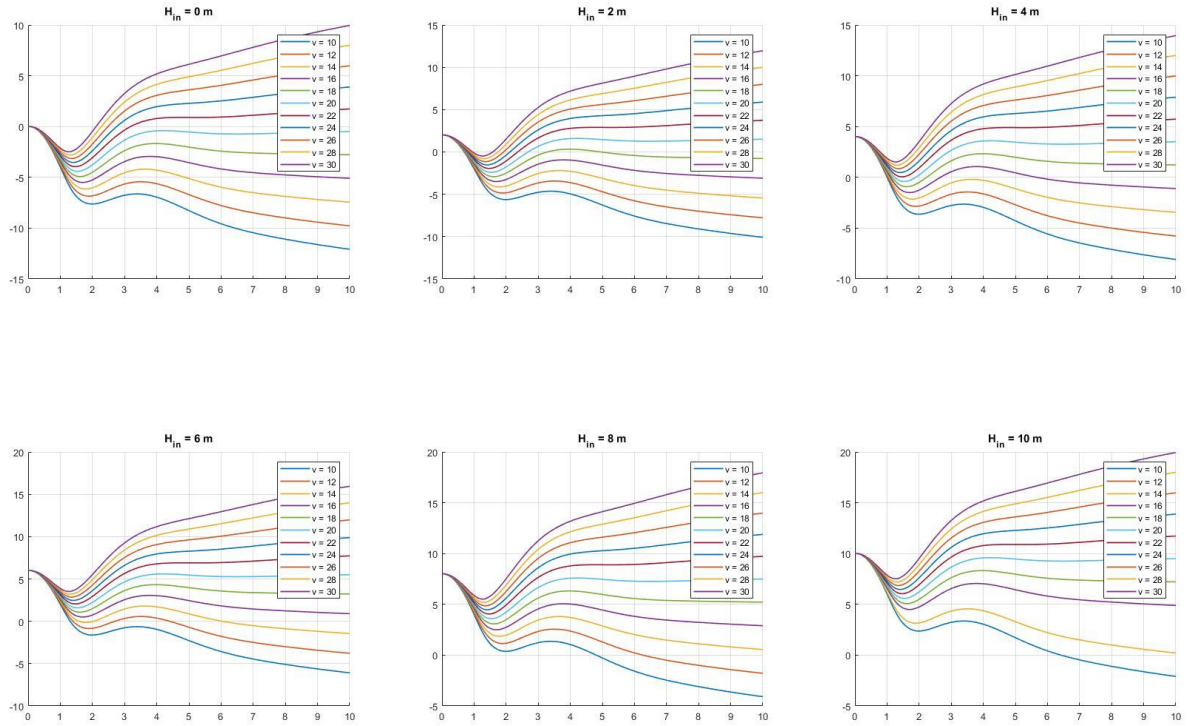
**Figure 6.1-11: Deploying of the wing:  $\psi$  Angle with and without autopilots**



**Figure 6.1-12: Deploying of the wing:  $\theta$  Angle with and without autopilots**

How is possible to see, also in this case with the autopilot the dynamic is more stable in particular, for the variables concerning the lateral directional dynamic.

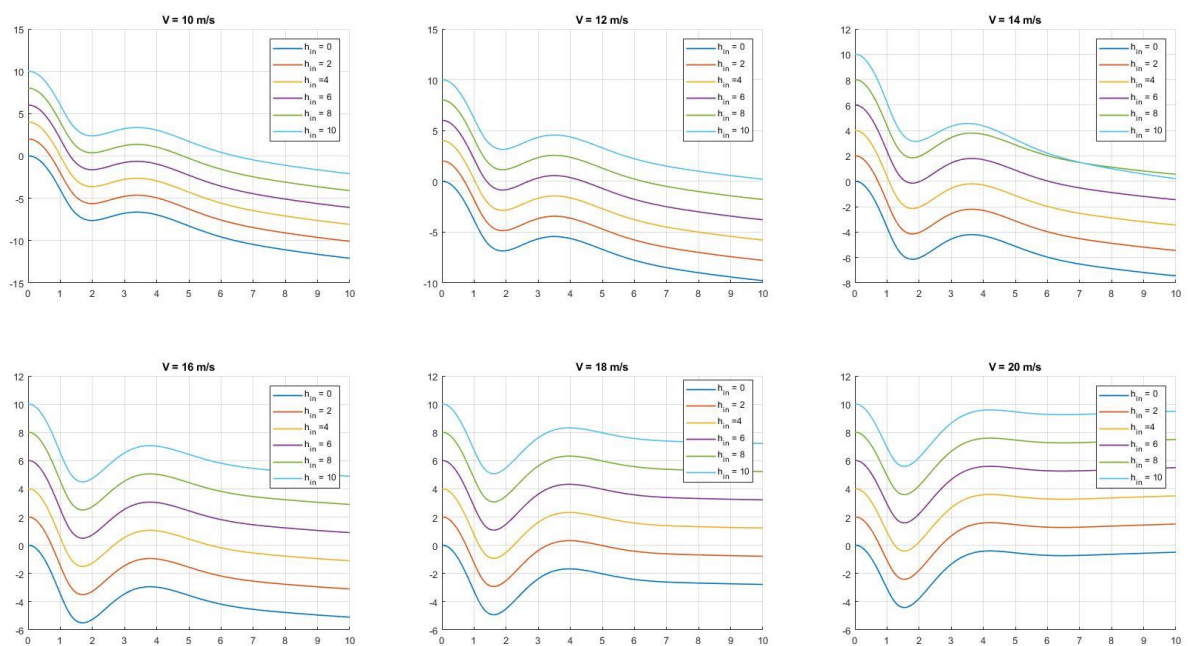
From Figure 6.1-6 and Figure 6.1-12, it is possible to see that the change of the dynamic for different sweep angle, give an unstable dynamic for the vehicle. This dynamic is tested with the autopilots, RAH and PAH, in order to see if with them the dynamic is more stable. Because the dynamic of the jump is influenced by different variables, a study for different initial condition has been done. In particular, different velocity and different altitude have been considered in order to define a minimum altitude and velocity that make sure that, after the jump out of the water, the aircraft is able to continue the mission profile. In particular it is considered an initial velocity between  $V = 10 \text{ m/s}$  and  $V = 30 \text{ m/s}$ , and a initial altitude between  $H = 0 \text{ m}$  and  $H = 10 \text{ m}$ . Results for different initial condition are shown in Figure 6.1-13 and Figure 6.1-14.



**Figure 6.1-13: Deploying of the wing: Simulation for different initial altitude**

It is possible to see in the Figure that the minimum altitude from where the aircraft is able to continue the mission is  $H = 6 \text{ m}$  with an initial velocity of  $V = 22 \text{ m/s}$ .

For different initial velocity the Figures:



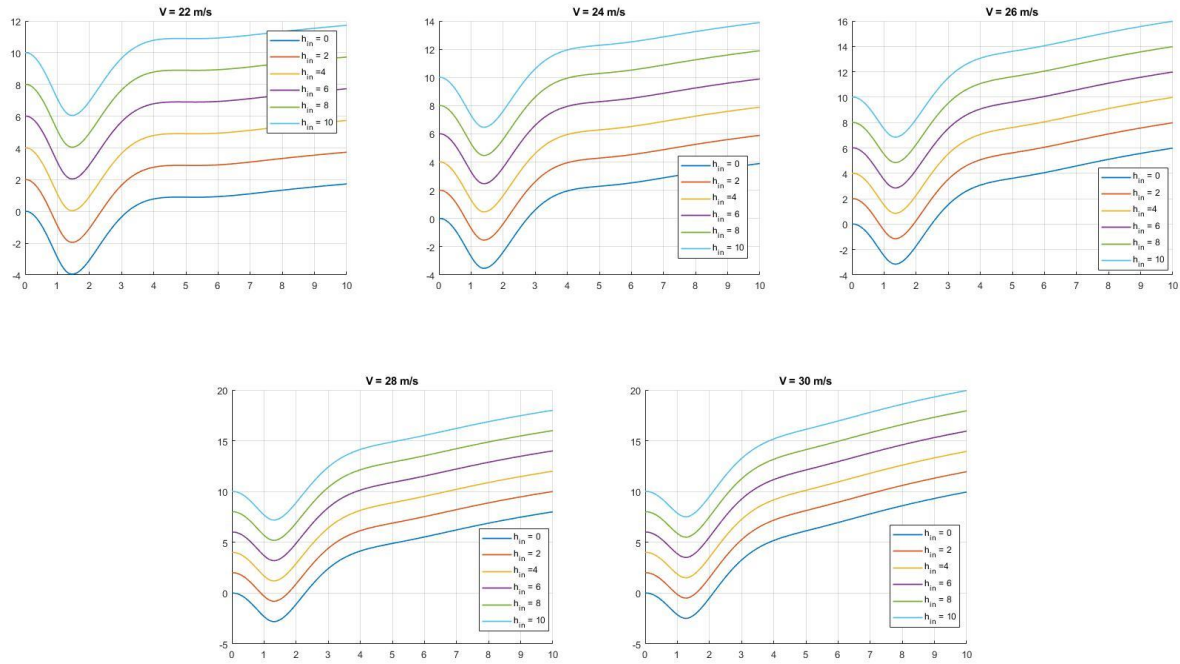


**Figure 6.1-14: Deploying of the wing: Simulation for different initial velocity**

The minimum velocity, reason why the direction of the trajectory is ascendant, is  $V = 20 \text{ m/s}$ . In conclusion the deploying of the wing should start when the aircraft is up of 6 metres and not under a velocity of 20 m/s. Because the dynamic of the jump is not very clear these conclusions are just preliminary, cause the variables that could influence the dynamic are more.

# Chapter 7: Results of Simulation for different aerodynamic model

---

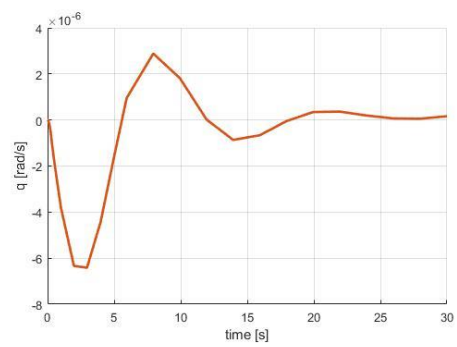
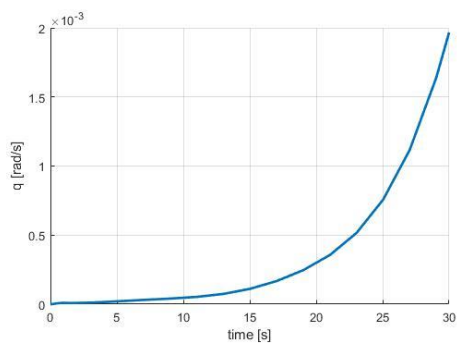
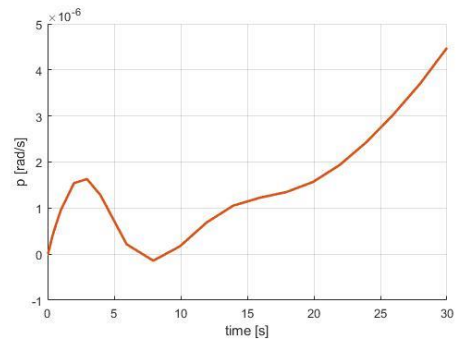
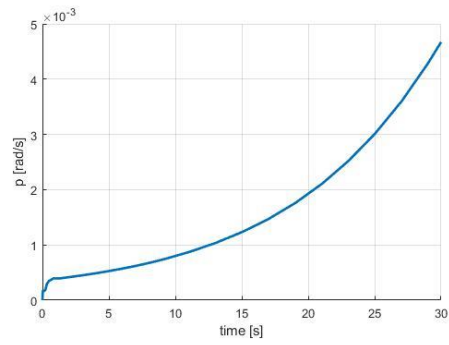
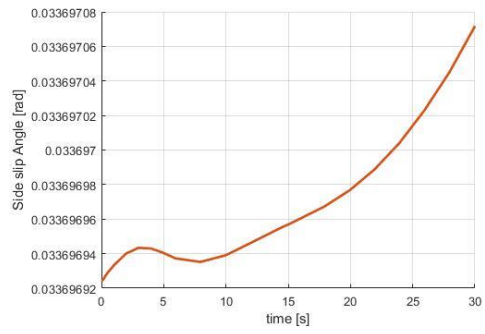
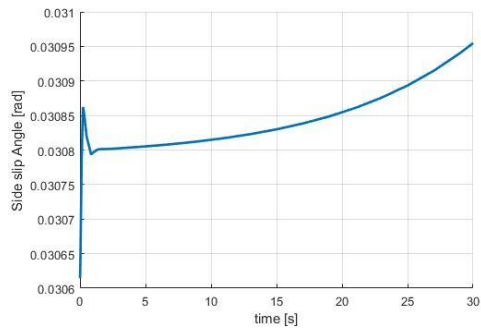
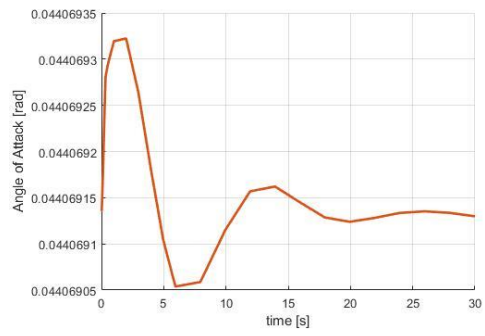
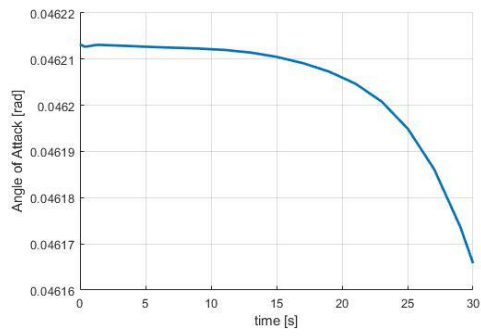
## 7.1 New aerodynamic model

After find the new coefficients by the wind tunnel test a new aerodynamic model has been implemented and tested. New trimmed conditions have been found, and results have been written in Table 7.1-1.

<i>xinco</i>		<i>xdot0</i>		<i>uaero0</i>	
$V [m/s]$	21	$\dot{V} [m/s^2]$	$-2,0643 \cdot 10^{-12}$	$d_e [rad]$	0,0264
$\alpha [rad]$	0,0441	$\dot{\alpha} [rad/s]$	$-6,9648 \cdot 10^{-13}$	$d_a [rad]$	0,0173
$\beta [rad]$	0,0353	$\dot{\beta} [rad/s]$	$5,3266 \cdot 10^{-15}$	$d_r [rad]$	0,0611
$p [rad/s]$	0	$\dot{p} [rad/s^2]$	$-4,8576 \cdot 10^{-12}$	$d_f [rad]$	0
$q [rad/s]$	0	$\dot{q} [rad/s^2]$	$1,2706 \cdot 10^{-12}$	<i>uprop0</i>	
$r [rad/s]$	0	$\dot{r} [rad/s^2]$	$1,2133 \cdot 10^{-12}$		
$\psi [rad]$	0	$\dot{\psi} [rad/s]$	0	$n [RPM]$	3250
$\theta [rad]$	0,0512	$\dot{\theta} [rad/s]$	0	$pz$	20
$\phi [rad]$	0	$\dot{\phi} [rad/s]$	0		
$x_e [m]$	0	$\dot{x}_e [m/s]$	20,9863		
$y_e [m]$	0	$\dot{y}_e [m/s]$	0,7421		
$H [m]$	0	$\dot{H} [m/s]$	0,1505		

Table 7.1-1: New Aerodynamic Model Trimmed condition

Results of the trimmed condition are presented in follow figures (see Figure 7.1-1) where a comparison is done with results founded with the previous dynamic model.



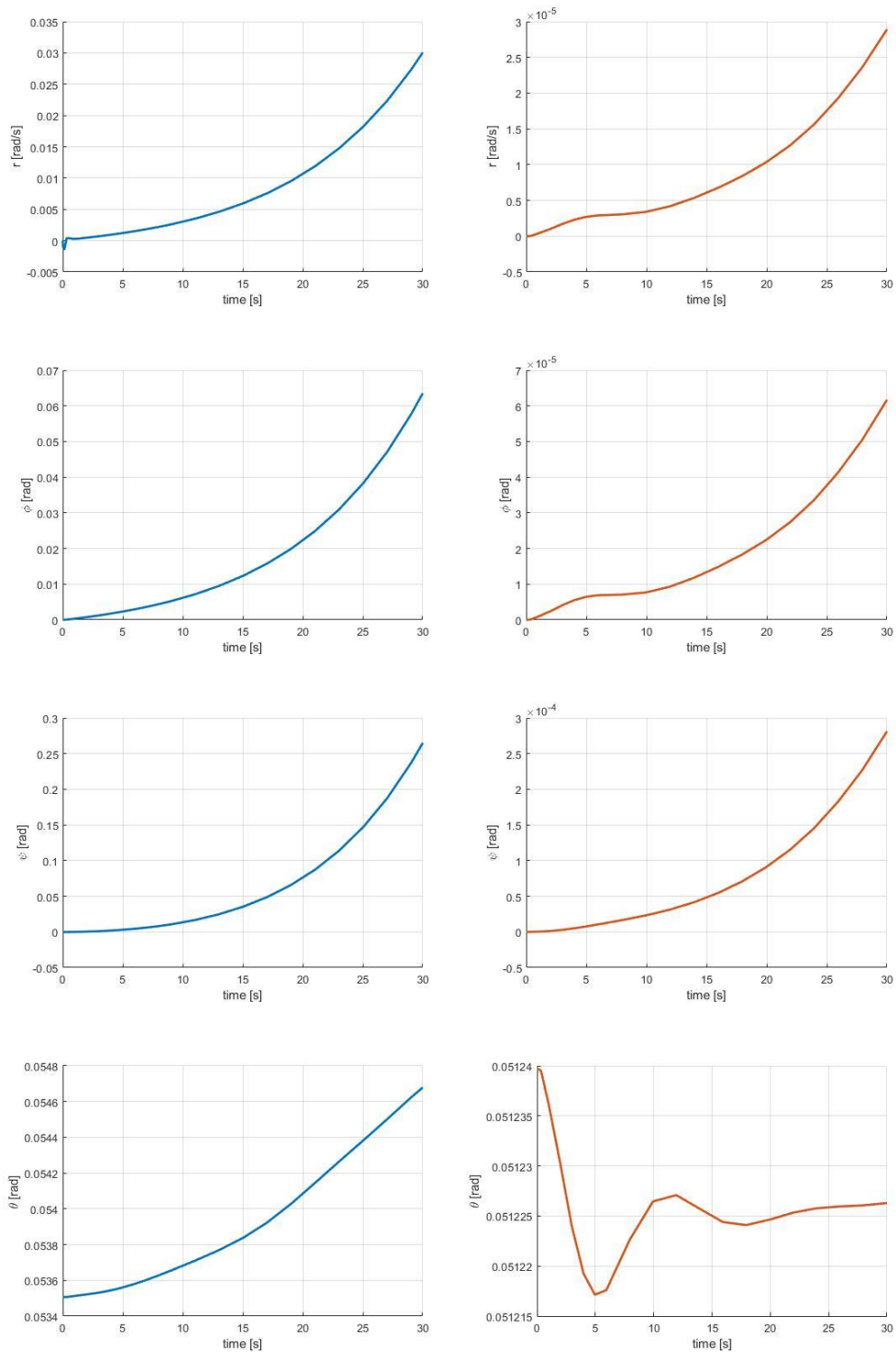


**Figure 7.1-1: Trimmed Condition: Comparison between Old(left) and New(right) aerodynamic model**

In Figure 7.1-2, Figure 7.1-3 and Figure 7.1-4 the root loci of the longitudinal and lateral directional motion are shown. In these figures a confront between the wind tunnel results, the previous dynamic and the new dynamic results has been done.

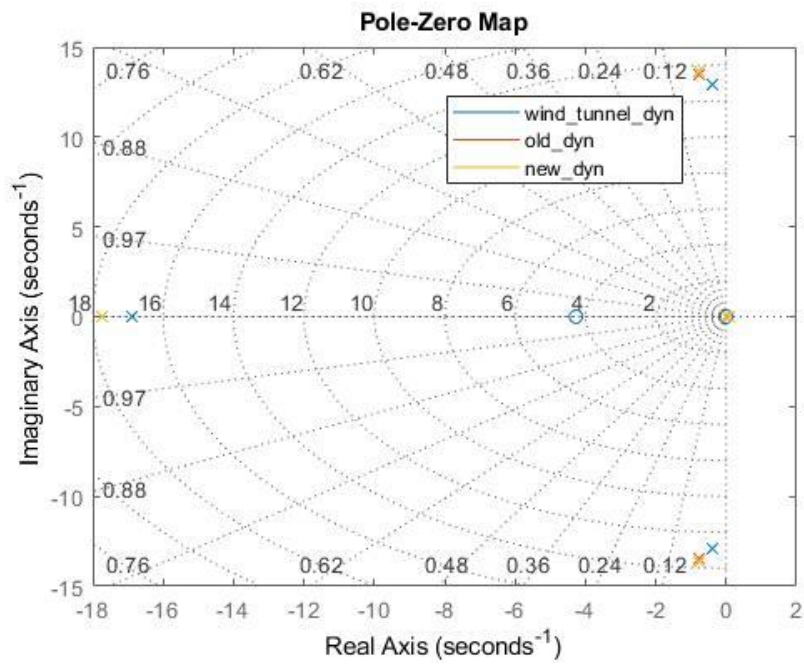


*Figure 7.1-2: Later-Directional root loci: comparison between results of different aerodynamic model*

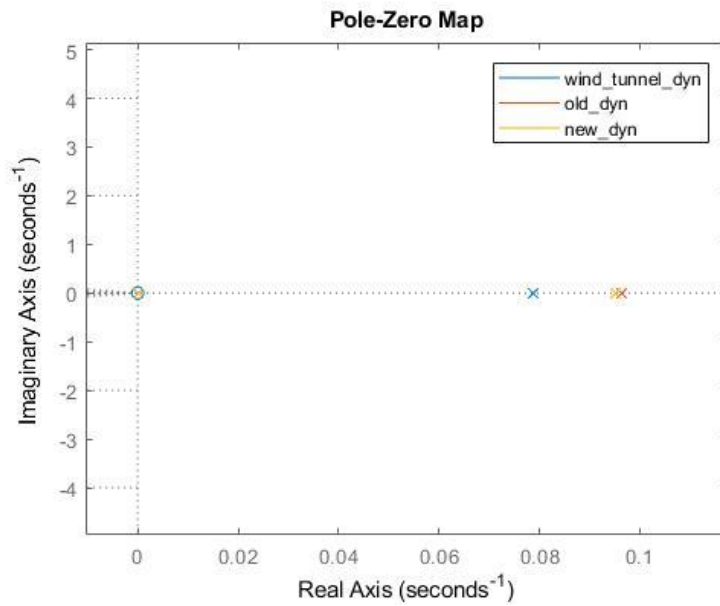


*Figure 7.1-3: Detail of root loci for lateral directional motion*



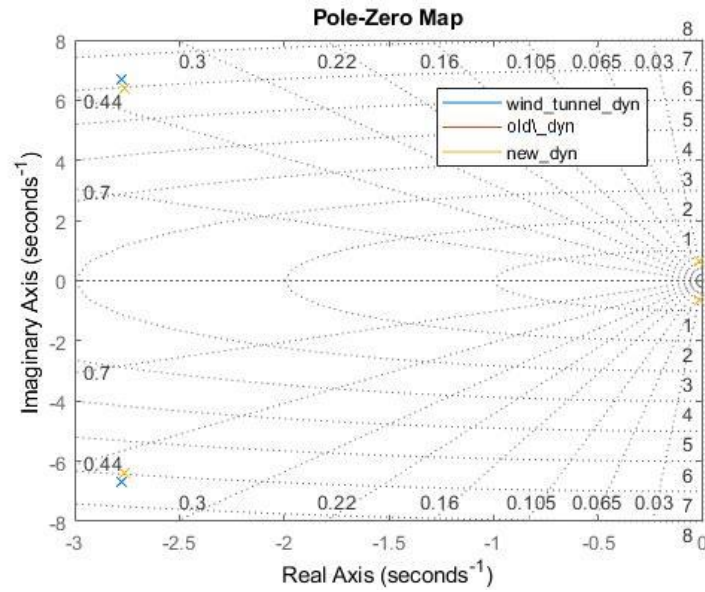


*Figure 7.1-4: Longitudinal root loci: comparison between results of different aerodynamic model*

How is possible to see in the figures regarding the trimmed condition and the root loci, and from the value of the eigenvalues, the instability of the spiral mode is still present. For these reasons the new aerodynamic model is tested with the RAH and PAH autopilot in order to see if is possible to use the same gain founded before for the previous dynamic model. The linearized model, divided in longitudinal and lateral-directional motion, has been used to test the two autopilots.

## 7.2 Results RAH Autopilots

Below the results of the autopilot RAH. In Figure 7.2-1 and Figure 7.2-2 a confront between the previous dynamic and new dynamic has been done. As done before for the previous aerodynamic model, also this time the autopilot is tested for two different reference signal duration of  $t = 5 \text{ sec}$  and  $t = 2,5 \text{ sec}$ .



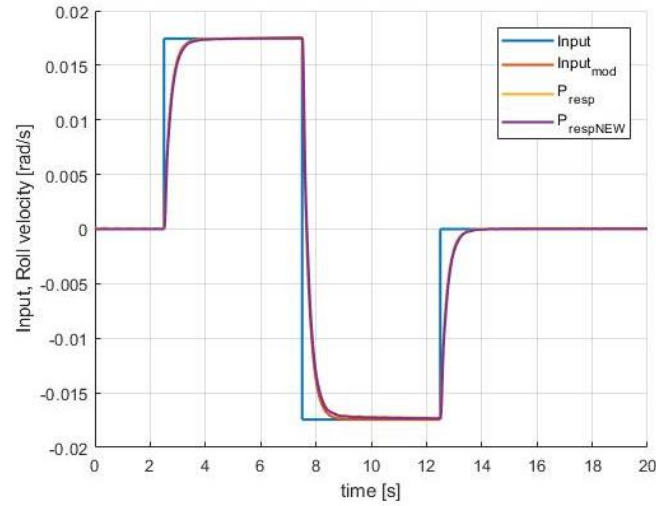


*Figure 7.2-1: Roll Attitude Hold: input ( $t = 2,5$  sec) and response of the system: comparison two aerodynamic model*

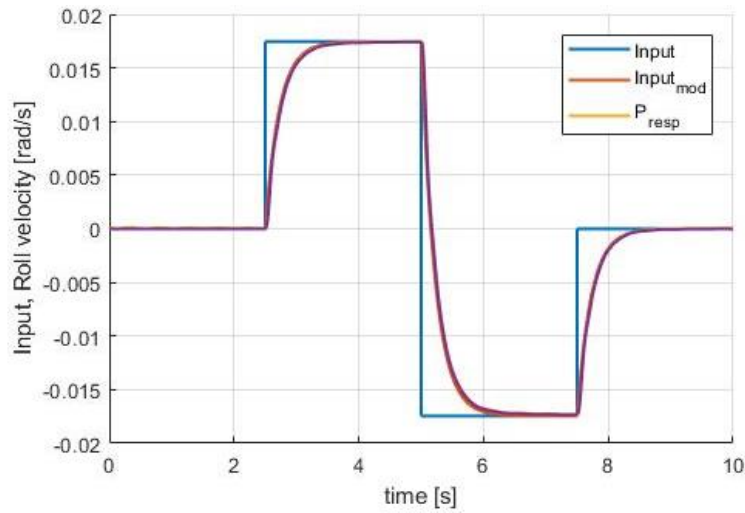


*Figure 7.2-2: Roll Attitude Hold: input ( $t = 5$  sec) and response of the system: comparison between two aerodynamic model*

It is possible to see that the difference between two aerodynamic is not really evidence.

### 7.3 Results PAH Autopilot

Below the results of the autopilot PAH. In Figure 7.3-1, a confront between the previous dynamic and new dynamic has been done.

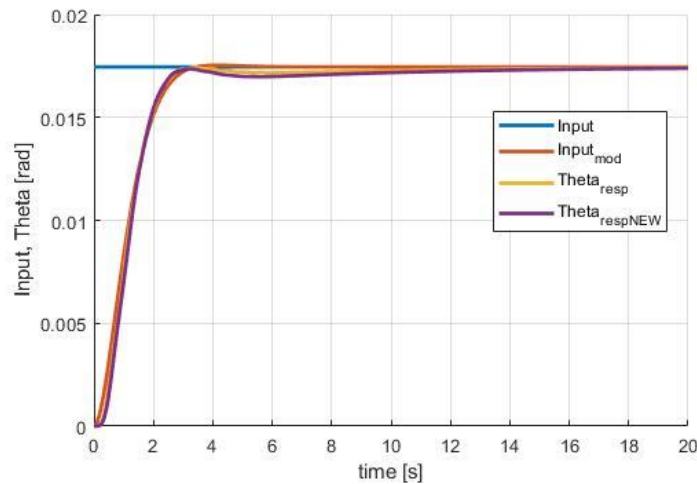


*Figure 7.3-1: Pitch Attitude Hold input and response: comparison between two aerodynamic model*

In this case the difference between the new and the previous dynamic are more evidence, and it is possible to see that the new aerodynamic is slower and the steady state error is more, but the specification are still respect.

## 7.4 Flight Control-Waypoint-Results

To test all the dynamic, except for the deploying of the wing, a mission profile with a several numbers of waypoints has been built and tested with both the aerodynamic model used during the study.

For this reason, in the Simulink scheme of the PAH and RAH autopilot (see Figure 4.6-1) is implemented the wind, the delay of the sensor and simple scheme of flight management computer to switch mode between all autopilots (see Figure 7.4-1).

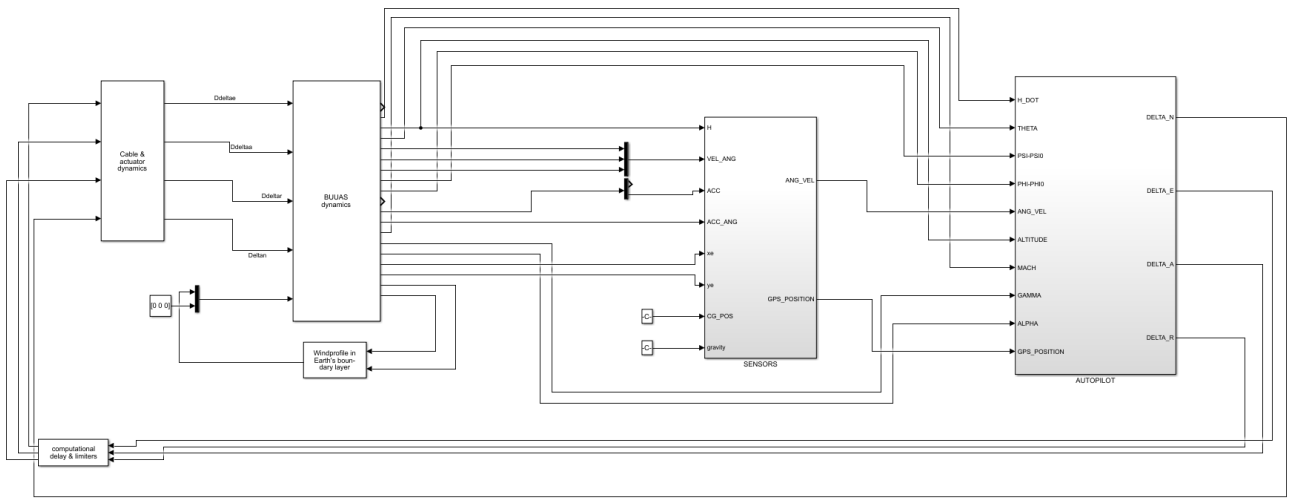


**Figure 7.4-1: Simulink model of BUUAS' Simulator**

### 7.4.1 Wind Simulation

A wind profile in Earth's boundary layer has been considered. For the simulation of the wind, a block set coming from the FDC Toolbox [23] has been used (see Figure 7.4-2). It specifies the magnitude and the direction of the wind velocity as a function of altitude. It converts, also, the wind velocity from Earth to Body-axes. It takes as inputs the altitude ( $H$  [m]) and the Yaw angle  $\psi$  [rad] and it gives a output vector with the component in different direction of the wind [ $uw$   $vw$   $ww$ ]. Below, in Figure 7.4-3, the structure of the wind block is shown.

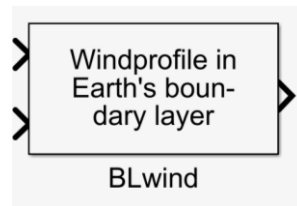


**Figure 7.4-2: Simulink model of wind profile take by FDC-toolbox**

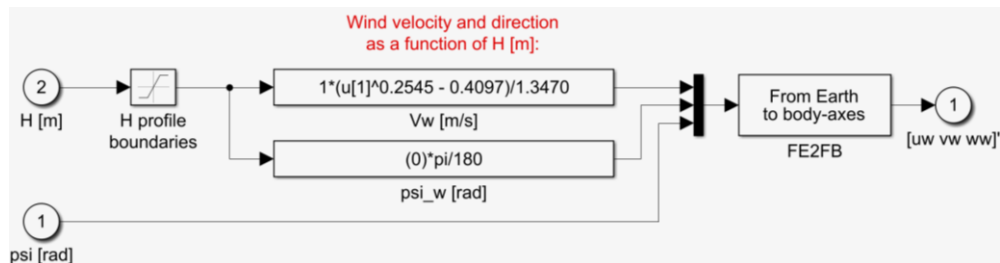


**Figure 7.4-3: Inside wind profile mask**

## 7.5 Sensor

The sensor implemented in the simulation are:

- Three-axis Inertial Measurement Unit (IMU)
- Global Position System (GPS)

These two sensors have been chosen because it is possible to have all necessary measurements of volumes required to the control system [24].

### 7.5.1 Inertial Measurement Unit

A block, came from the Aerospace toolbox of Simulink, has been used for the Inertial Measurement Unit. It needs, as input, the follow variables:

- Acceleration Vector (Body frame);
- Angular Velocity Vector (Body frame);
- Angular Acceleration Vector (Body frame);
- Position of the Center of Gravity (CG);
- Gravity Magnitude

Acceleration, Angular Velocity and Angular Acceleration vectors, are come from the block BUUAS dynamic; for the position of the Center of Gravity, it is considered that the IMU is positioned just in correspondence of the CG. Finally, the magnitude of the force of gravity is considered constant with the altitude because the mission profile shows altitude very low, and it is equal to  $g = 9,81 \text{ m/s}^2$ .

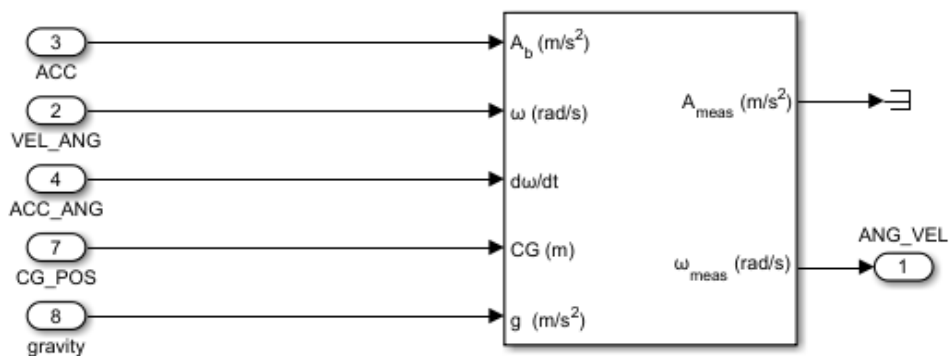


Figure 7.5-1: Simulink scheme of IMU took by Aerospace toolbox

The IMU is composed by the Accelerometer and the Gyroscope. Because these sensors are not already present on the vehicle, a typical sensor is evaluated. The value asked from the Block are shown in Figure 7.5-2 – 7.5-3 – 7.5-4:

Block Parameters: Three-axis Inertial Measurement Unit

Three-axis Inertial Measurement Unit (mask) (link)

Implement a three-axis inertial measurement unit (IMU).

Main Accelerometer Gyroscope Noise

☐ Second-order dynamics for accelerometer

Accelerometer natural frequency (rad/sec): 190

Accelerometer damping ratio: 0.707

Accelerometer scale factor and cross-coupling: 0; 0 1.0038 0; 0 0 0.9945

Accelerometer measurement bias: 0.09 -0.06 0.337

Accelerometer upper and lower limits: -50 -50 -50 50 50 50

**Figure 7.5-2: Detail of IMU parameters: Accelerometer**

Block Parameters: Three-axis Inertial Measurement Unit

Three-axis Inertial Measurement Unit (mask) (link)

Implement a three-axis inertial measurement unit (IMU).

Main Accelerometer Gyroscope Noise

☐ Second-order dynamics for gyro

Gyro natural frequency (rad/sec): 190

Gyro damping ratio: 0.707

Gyro scale factors and cross-coupling: 0.9986 0 0; 0 1.0064 0; 0 0 1

Gyro measurement bias: -0.0095 -0.0075 0.0015

G-sensitive bias: 0 0 0

Gyro upper and lower limits: -10 -10 -10 10 10 10

**Figure 7.5-3: Detail of IMU parameters: Gyroscope**

Block Parameters: Three-axis Inertial Measurement Unit

Three-axis Inertial Measurement Unit (mask) (link)

Implement a three-axis inertial measurement unit (IMU).

Main Accelerometer Gyroscope Noise

☒ Noise on

Noise seeds: 41 41 41 41 41 41

Noise power: 3e-4 1.8641e-4 3.7251e-4 1.0652e-8 1.3021e-8 1.1929e-8

**Figure 7.5-4: Detail of IMU parameters: Noise**

## 7.5.2 Global Position System

A block, come from the Aerospace toolbox of Simulink, has been used also for the Global Position System (GPS). In particular, this block has been used just to convert the local position in Earth axis to geodetic Latitude, Longitude and Altitude. Inputs of the block are the position  $x_e$ ,  $y_e$  and the altitude calculate from the BUUAS dynamic block. As outputs it gives the geodetic coordinates that will be used by the flight management computer to switch autopilots and waypoint.

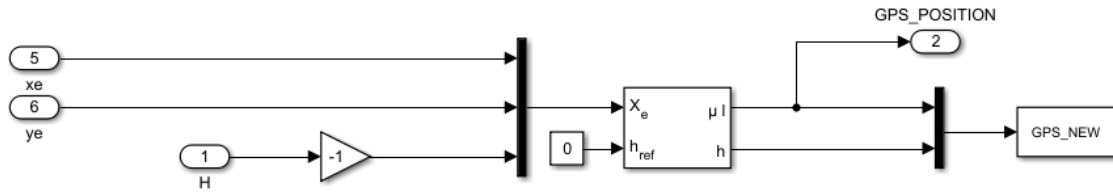


Figure 7.5-5: GPS' Simulink Model

## 7.6 Waypoint Definition

The trajectory is designed with link of different waypoints. The coordinates of the waypoints have been found with the follow formulas [25].

$$\begin{aligned} Latitude &= \text{asin} \left( \sin(lat_{in}) \cos \left( \frac{d}{R} \right) + \cos(lat_{in}) \sin \left( \frac{d}{R} \right) \cos(\theta) \right) \\ Longitude &= long_{in} + \text{atan2} \left( \sin(\theta) \sin \left( \frac{d}{R} \right) \cos(lat_{in}), \cos \left( \frac{d}{R} \right) - \sin(lat_{in}) \sin(lat_{new}) \right) \end{aligned} \quad (42)$$

Where:

- $lat_{in}$  is the latitude of the waypoint before;
- $d$  is the distance between the waypoint ([km]);
- $R$  is the radius of the Earth;
- $\theta$  is the direction to follow to arrive to next waypoint;
- $long_{in}$  is the longitude of the waypoint before;

The initial latitude and longitude considered are:

$$LAT_{in} = 47,33219^\circ$$

$$LONG_{in} = -122,2268^\circ$$

It is possible to change the initial position of the aircraft and to define the trajectory adding waypoint, but it necessary to calculate latitude and longitude of all the waypoint before starting the simulation. For this reason, a call back button has been positioned on the simulator: with a double click on the button ‘Select Trajectory & reference signals’, a menu will appear where is possible to chose four different trajectories already calculate, or to define new waypoints. After calculated the position of the waypoint, the latitude and longitude of them, will be memorize in the MATLAB® workspace to be use during the simulation.

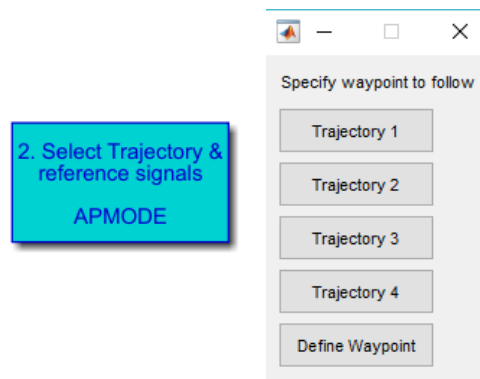


*Figure 7.6-1: Detail of callback button to chose Waypoints of trajectory*

### 7.6.1 Waypoint Switch

Definition of the waypoint is important to figure out the trajectory before the simulation starts, but also because, during the simulation, the position of the vehicle is confronted with the coordinate of the waypoint, in order to define in which segment of the trajectory is the vehicle. For each waypoint reference variables, as example the heading, altitude, flight path and Mach, are provide to the autopilots. It's important to be sure that the simulator will change the waypoint. A radius of 1 meter is designed around all waypoints. If the aircraft is inside the radius of the waypoint, the simulator will change waypoint using the follow structure shown in Figure 7.6-2:

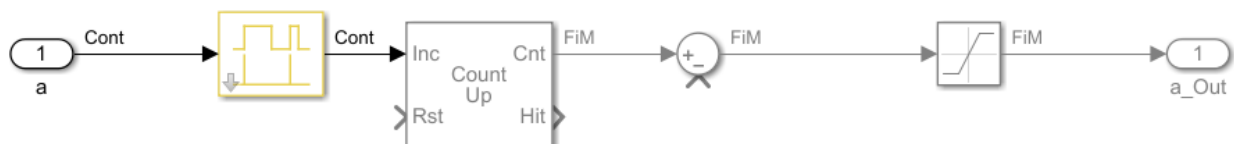


*Figure 7.6-2: Detail of scheme for the switch of waypoint*

When the position of the vehicle is inside the radius the variable  $a$ , that before was equal to zero, will be equal to 1; in this way the block 'count up' will count 1 and the waypoint will switch.

## 7.7 Autopilot Switch

In the different phase of the mission profile it is necessary to use different autopilots. For example, during the phase of climb or descent the Altitude Select is active, while during the cruise the Altitude Hold is active. How explain in the Chapter 4, because these two autopilots use different variables, the angle  $\theta$  commanded should be different and that should give an unstable dynamic. For this reason, a switch criterion is formulated: if the position of the vehicle is included in a range of  $\Delta H = \pm 5 [m]$  to the altitude reference, the autopilot mode change from altitude select to altitude hold. The Simulink structure of this criterion is represented in the Figure 7.7-1.

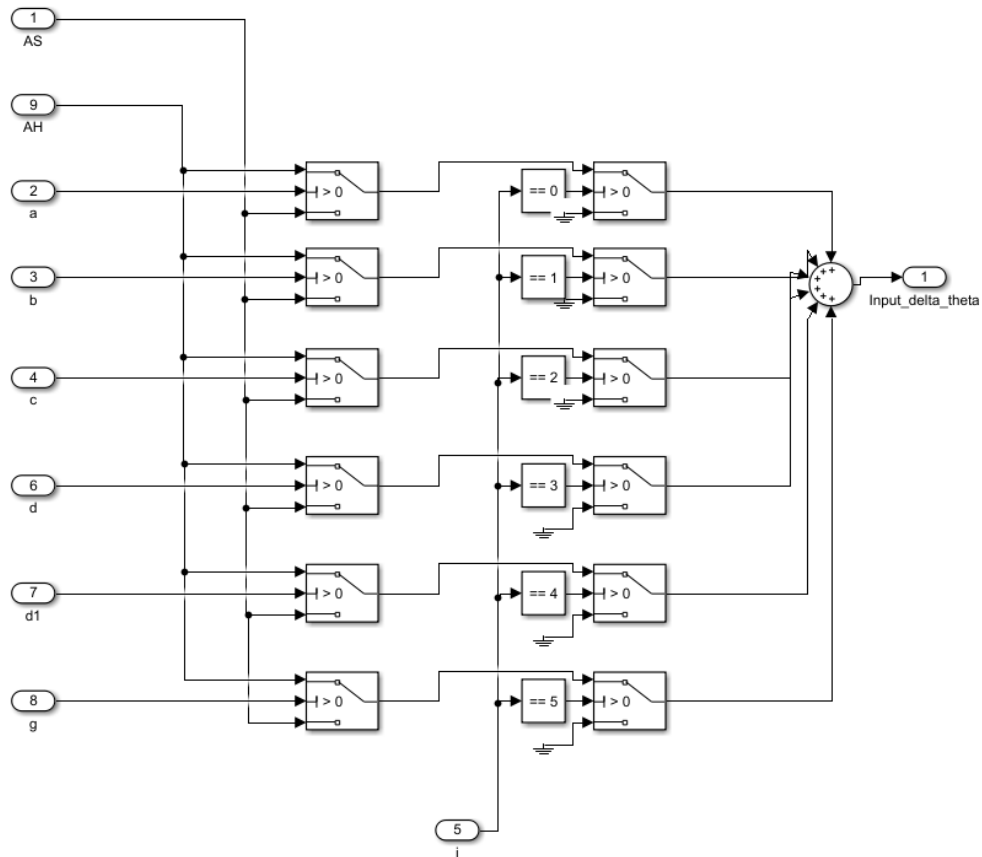


Figure 7.7-1: Detail of autopilots' switch



To be sure that the difference between the angle provide by autopilots, AH and AS, is similar when a switch is necessary, an external initial condition and an external rising is provided at the integrator of both autopilots.

## 7.8 Guidance Control

Regarding to the guidance control a simple algorithm is implemented. When the position of the aircraft is in a passageway of length 1 meter, the reference heading is the same decided with the definition of the waypoint. If the aircraft go out of the passageway, a new reference heading is calculated with the follow formula (Eq. (43)):

$$Heading_{correct} = atan2(|long_{arr} - long_{att}|, \Delta\phi) \quad (43)$$

Where:

- $long_{arr}$  is the longitude of destination;
- $long_{att}$  is the longitude of the actual position;
- $\Delta\phi$  is define by the follow formula:

$$\Delta\phi = \log\left(\frac{\tan\left(lat_{arr} + \frac{\pi}{4}\right)}{\tan\left(lat_{att} + \frac{\pi}{4}\right)}\right) \quad (44)$$

Where:

- $lat_{arr}$  is the latitude of destination point;
- $lat_{att}$  is the latitude of the actual position.

Because the heading is an angle included  $\psi_{min} = 0 [deg]$ , and  $\psi_{max} = 360 [deg]$ , but the function  $arctan$  is included in a range of  $\psi = \pm 180 [deg]$ , it is necessary to apply the follow criteria [26]:

if  $\psi_d > \psi$

$$\epsilon_{r-turn} = (\psi_d - \psi) \quad (45)$$

$$\epsilon_{l-turn} = (\psi_d - \psi) - 360^\circ$$

if  $\psi_d < \psi$

$$\epsilon_{r-turn} = (\psi_d - \psi) + 360^\circ \quad (46)$$

$$\epsilon_{l-turn} = (\psi_d - \psi)$$

Where:

- $\psi_d$  is the desired heading
- $\psi$  is the actual heading
- $\epsilon_{r-turn}$  is the value of the angle if a right turn is necessary
- $\epsilon_{l-turn}$  is the value of the angle if a left turn is necessary

## 7.9 Results

Different trajectories are tested in order to know the response of the vehicle to a different input of climb and turn. Below the result for the second trajectory is shown. The two aerodynamic model are taken in consideration and a confront between the result is done. In the Table 7.9-1 there are the data of different waypoint refer to the second trajectory.

	<b><i>H</i></b>	<b><i>longitude</i></b> [°]	<b><i>latitude</i></b> [°]	<b><i>θ<sub>ref</sub></i></b> [°]	<b><i>distance</i></b> [km]
<b>WAY 1</b>	0	−122,2268	47,3321	180	0
<b>WAY 2</b>	200	−122,2268	47,2872	180	5
<b>WAY 3</b>	200	−122,2268	47,2783	180	1
<b>WAY 4</b>	200	−122,2268	47,2513	180	3
<b>WAY 5</b>	200	−122,1982	47,2400	120	2,5

*Table 7.9-1: Tracjetory 2 data*

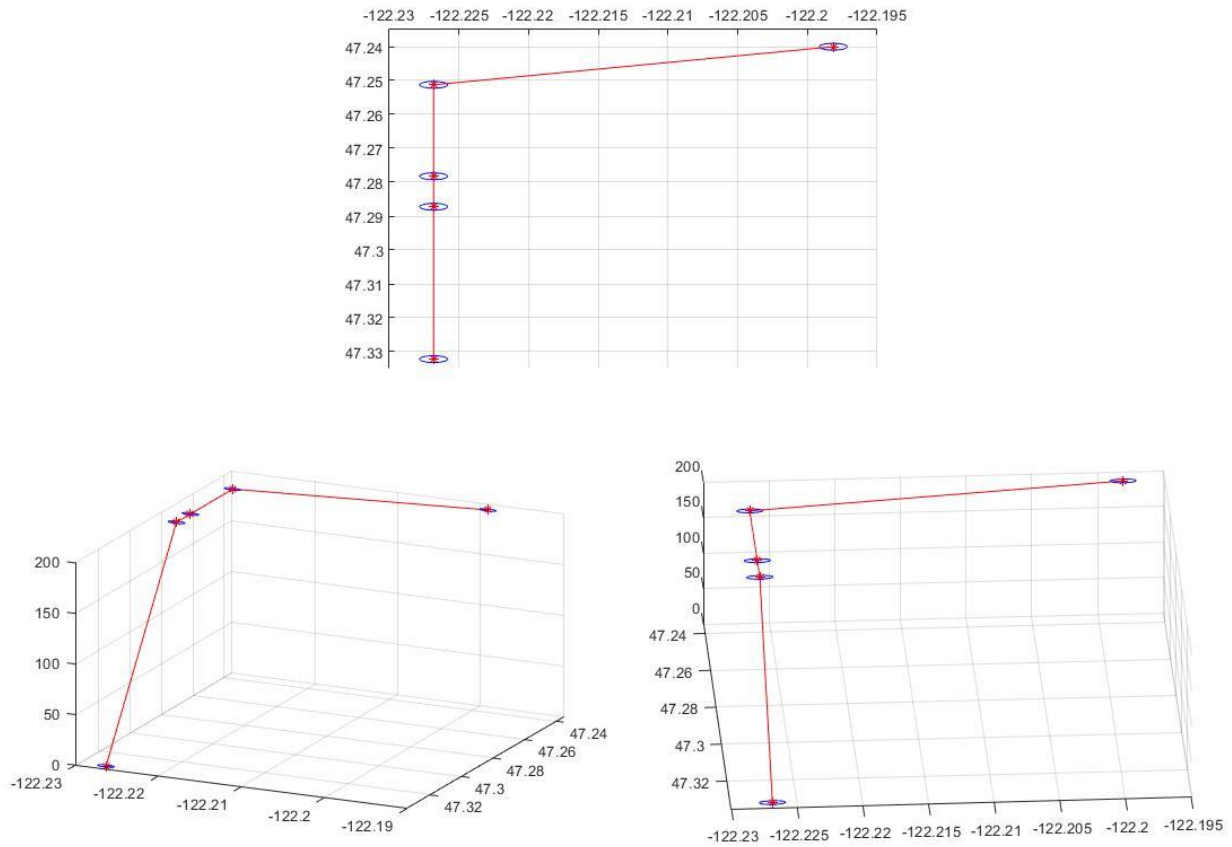
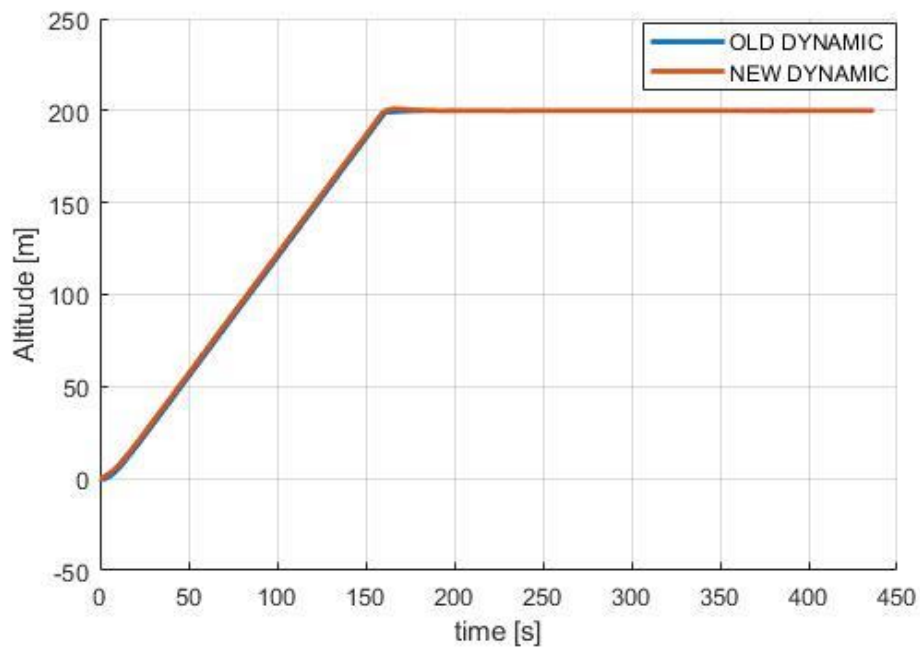
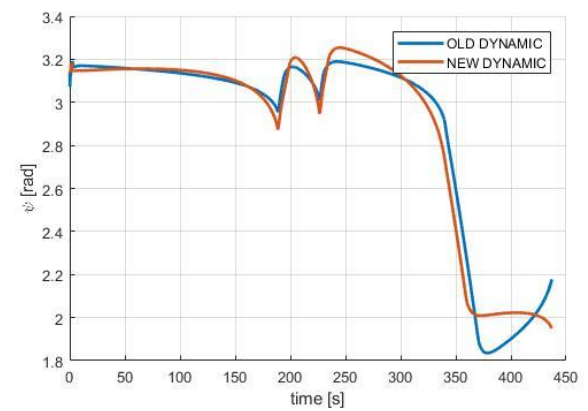
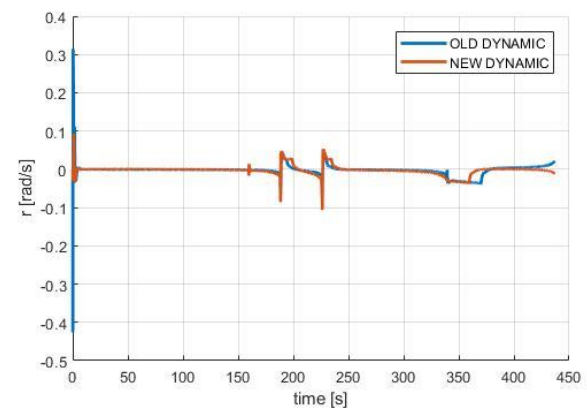
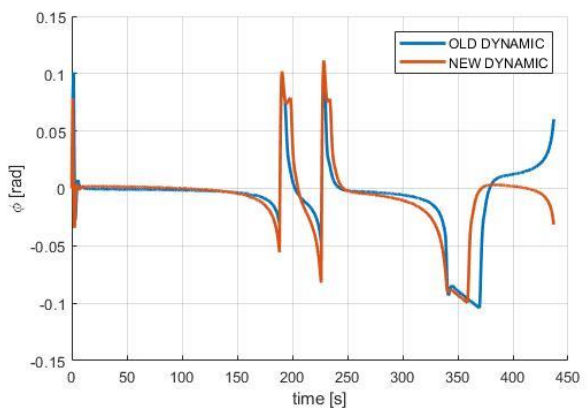
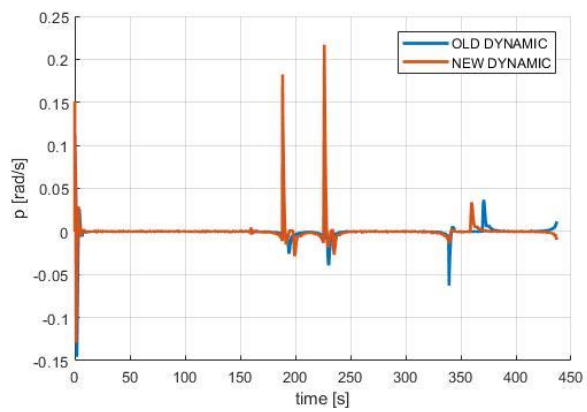
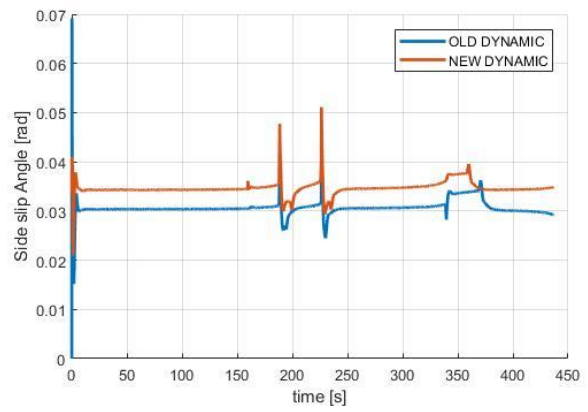
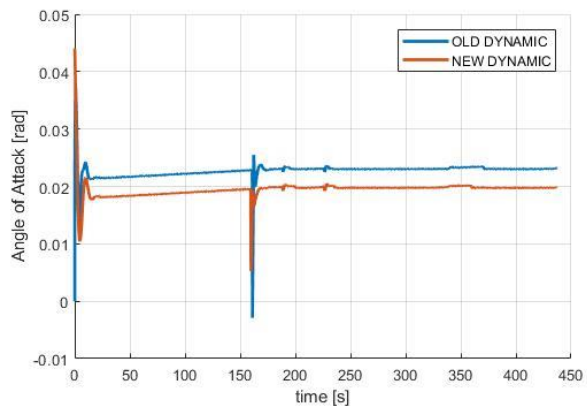
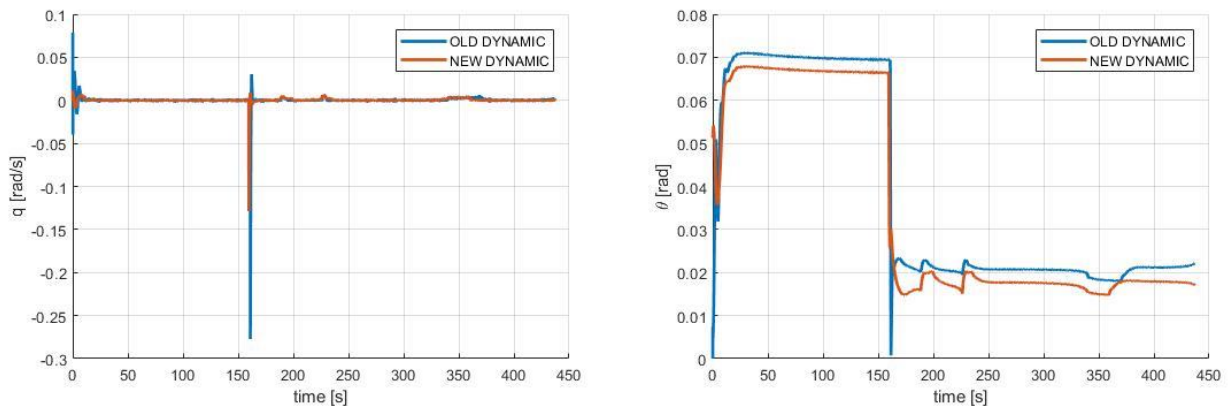


Figure 7.9-1: Trajectory 2 3D graphics: details of waypoints







**Figure 7.9-2: Trajectory example: comparison between two aerodynamic model**

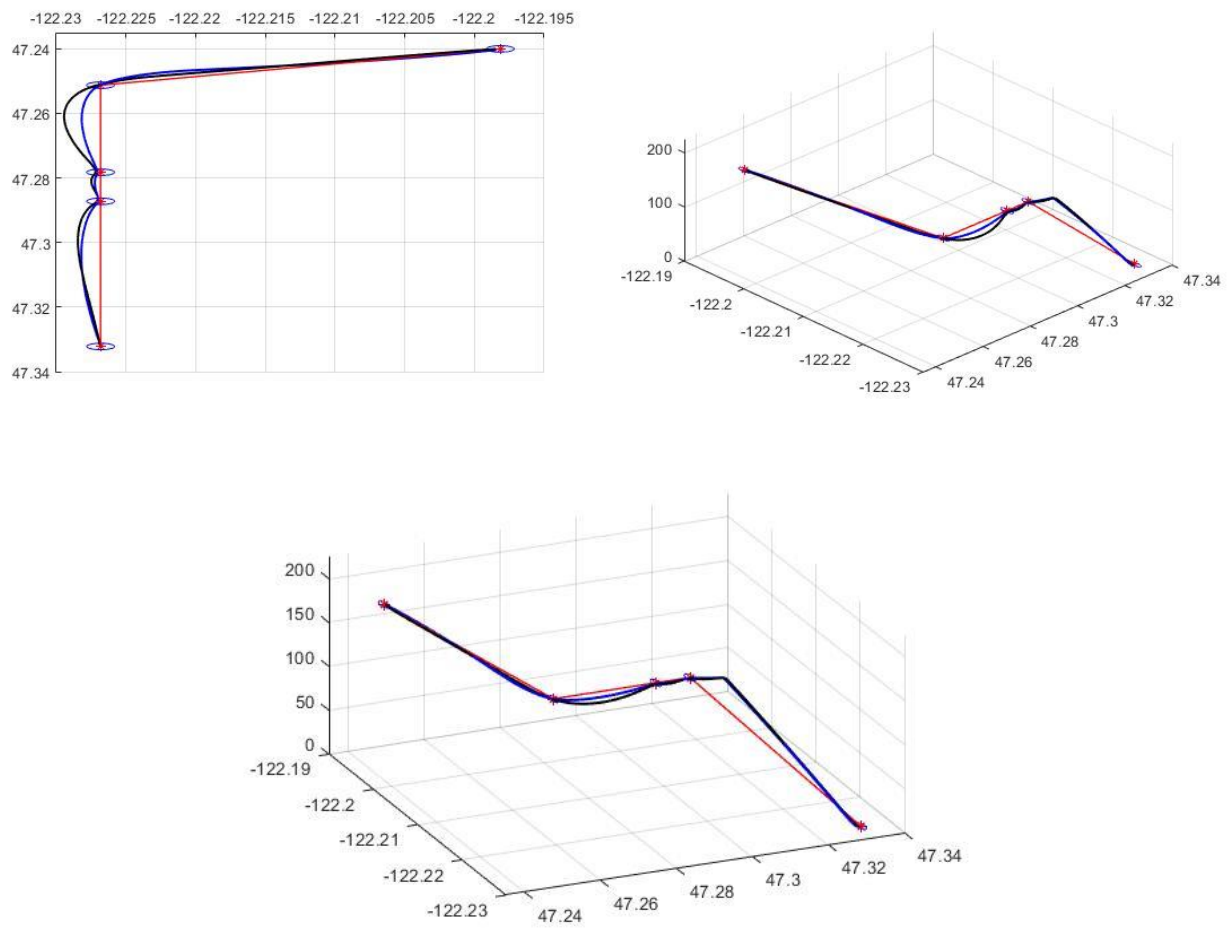


**Figure 7.9-3: Trajectory 2: 3D graphics**

## Chapter 8: Conclusion and Future Work

---

This thesis is insert in a project of RMIT University on the development of a new vehicle with a specific mission profile: BUUAS, bi-modal unmanned underwater/air system. It focuses on three main topics:

- ❖ Implementation of a simulator for the BUUAS;
- ❖ Study of the tail configuration;
- ❖ Study of a critical phase of mission profile of BUUAS vehicle: deploying of wings.

The mission profile of BUUAS vehicle provides two main phases: an underwater and an air cruise. This thesis concerns only the air phase, because of the presence of few data relative to the underwater configuration and aerodynamic. A first aerodynamic model has been implemented with data came from a previous wind tunnel test. Dynamic analysis of the model reveals an instability of the spiral mode. For this reason, different controller has been implemented and test during the simulation. Due to the nature of the vehicle, it is an UAV, so unmanned, and because there is not an official specification for these vehicles, a new specification has been considered by reference to the MIL-HDBK-1797.

The vehicle built is only demonstrative and it has no sensors installed. For this reason, it has been decided to implement only two sensors for the simulation: a GPS and an IMU. They are two sensors that could give all the necessary variables for the control and they work in the air as well as in the water. Generic sensors have been taken in consideration, because they are not installed yet.

The aerodynamic model founded with a first wind tunnel test does not take care about the specific configuration of the tail. The tail has been built with an anhedral angle. Due to this particular configuration, a study of the influence of the tail on forces and moments has been done. New wind tunnel test has been done using a moved tail and tested the vehicle in different configuration: different angle of attack, side-slip angle and finally different velocity. Results of the wind tunnel test show that there is a connection between the longitudinal and lateral directional dynamic: different angle of deflection of the tail give a component of the roll and yaw moment with and without the presence of a side-slip angle. For this reason, a new aerodynamic model has been implemented and tested. The results show a different between the two aerodynamic model, so the new model is more accurate then the previous.

The most critical phase of the mission profile is the transition phase, when the vehicle jumps out of the water and change the aerodynamic configuration opening the wing. For this reason, a simulation for this exact phase has been done, in order to demonstrate that the vehicle complete this phase successfully and that the presence of autopilots it is necessary. A wind tunnel test has been done to create a correct aerodynamic model for this phase: the vehicle has been tested for seven different sweep angles and in different conditions. Since the phase depends on several factors, simulations have been done with different initial velocity and altitude: results show that the presence of the autopilots is fundamental to the success of the mission at the minimum altitude where the vehicle have to start the deploying is around 6 [m], at a minimum velocity of 20 [ms<sup>-1</sup>].

For a future work, several aspects of the simulation can be improved. At first, in order to obtain an aerodynamic model more accurate, a new wind tunnel test should be done also with the rotor active and with a different pitch, side-slip angles and velocities.

In the simulator a flight management system (FMS) has been built to switch autopilots and to follow the trajectory correcting the heading of the vehicle and switching the waypoint. The FMS is built with a series of MATLAB® functions and the simulation results very slow. The stateflow, a particular programming tool for finite state machine, could be used in order to make the simulation faster.

Moreover, results obtained by the simulation show that an optimization of the trajectory is necessary considering an important aspect that has been neglected in this thesis: the vehicle has as only energy source a battery pack, so limited energy that must be optimized. Finally, for a good optimization of the trajectory, different tests should be done in order to define the limit of the vehicle.

An optimization it is necessary also for the critical phase of transition between water and air. Different initial conditions have to be tested in order to determine the optimum angle and velocity to jump out of the water and to link the water to the air simulation.

Another Simulator has been developed linking the X-plane® simulator whit the Simulink scheme of autopilots. It is possible, how reported in a paper of M.K. Yalcin and Erhan Ersoy [27], receive several variables' volumes to the X-plane simulator and send inputs for the surface control of the vehicle. The X-plane 10 has been utilized. A model of the BUUAS vehicle has been implemented with the X-plane aircraft maker and, with the Airfoil maker, wings profiles have been reproduced more similar to the original vehicle as much as possible. Same autopilots have been implemented and tested in the trajectory of the simulator built with the aerodynamic model came from wind tunnel tests. Results of aerodynamic and control, show in Appendix B, are very close. In conclusion it is possible to use X-

plane like graphic interface. The X-plane simulator has some limits: it is not possible to teste the deploying of the wing and the underwater cruise. It is necessary to use a different graphic interface to have a complete simulator.



# References

---

1. Bacciaglia, A., et al., *BIMODAL UNMANNED VEHICLE: PROPULSION SYSTEM INTEGRATION AND WATER/AIR INTERFACE TESTING*.
2. D. Guo, *Modelling and experimental investigation of a Bi-modal Unmanned Underwater/Air System*, RMIT University: Melbourne, Australia, 2019, chapter 5, pag 131.
3. Dr. Robert C. Nelson, *Flight Stability and Automatic Control*, II ed., University of Notre Dame: McGraw-Hill International Edition, 1998
4. Brian L. Stevens, Frank L. Lewis, Eric N. Johnson, *Aircraft Control and Simulation dynamics, controls design and autonomous system*, III ed., United States of America, Wiley, 2016, pag 207.
5. Bacciaglia, A., *Design and Development of a Propulsion System for a Water/Air Unmanned Vehicle*. 2017, University of Bologna: Bologna.
6. M. O. Rauw, “FDC1.2 - A SIMULINK Toolbox for Flight Dynamics and Control Analysis”, II ed., May 10, 2001
7. D. Guo, *Modelling and experimental investigation of a Bi-modal Unmanned Underwater/Air System*, RMIT University: Melbourne, Australia, 2019, chapter 2, pag 45.
8. M. O. Rauw, “FDC1.2 - A SIMULINK Toolbox for Flight Dynamics and Control Analysis”, II ed., May 10, 2001, Chapter 3, pag 22.
9. Dr. Robert C. Nelson, *Flight Stability and Automatic Control*, II ed., University of Notre Dame: McGraw-Hill International Edition, 1998
10. MIL-HDBK\_1797, “Department Of Defense Handbook, Flying Qualities of Piloted Aircraft”, United States of America, 19 December 1997
11. Corona, *Corona, 191MG Metal Gear Servo 1.7kg/0.06sec/12.5g*. 2019; Available from: [https://hobbyking.com/en\\_us/corona-919mg-digital-metal-gear-servo-1-7kg-0-06sec-12g/](https://hobbyking.com/en_us/corona-919mg-digital-metal-gear-servo-1-7kg-0-06sec-12g/)
12. Spektrum, *A3030 Mid Torque High Speed SubMicro Plastic Servo*. 2019. Available from: <https://www.spektrumrc.com/Products/Default.aspx?ProdID=SPMSA3030>

13. Brian L. Stevens, Frank L. Lewis, Eric N. Johnson, *Aircraft Control and Simulation dynamics, controls design and autonomous system*, III ed., United States of America, Wiley, 2016, pag 295.
14. Brian L. Stevens, Frank L. Lewis, Eric N. Johnson, *Aircraft Control and Simulation dynamics, controls design and autonomous system*, III ed., United States of America, Wiley, 2016, pag 304
15. N. A. Musa, “Effects of Aircraft Tail Configuration on Sensitivity to Yaw Disturbances”, in Reserchgate.net, October 2014
16. Marcello R. Napolitano, *Aircraft Dynamics: From modeling to Simulation*, United States of America, Wiley, 2012
17. Marcello R. Napolitano, *Aircraft Dynamics: From modeling to Simulation*, United States of America, Wiley, 2012, Picture, pag 154
18. Marcello R. Napolitano, *Aircraft Dynamics: From modeling to Simulation*, United States of America, Wiley, 2012, Picture, pag 155
19. D. Guo, *Modelling and experimental investigation of a Bi-modal Unmanned Underwater/Air System*, RMIT University: Melbourne, Australia, 2019, Picture, pag 84.
20. D. Guo, *Modelling and experimental investigation of a Bi-modal Unmanned Underwater/Air System*, RMIT University: Melbourne, Australia, 2019, Picture, pag 84.
21. D. Guo, *Modelling and experimental investigation of a Bi-modal Unmanned Underwater/Air System*, RMIT University: Melbourne, Australia, 2019, Picture, pag 85.
22. D. Guo, *Modelling and experimental investigation of a Bi-modal Unmanned Underwater/Air System*, RMIT University: Melbourne, Australia, 2019.
23. M. O. Rauw, “FDC1.2 - A SIMULINK Toolbox for Flight Dynamics and Control Analysis”, II ed., May 10, 2001.
24. Feffrey D. Barton, “Fundamentals of Small Unmanned Aircraft Flight”, Johns Hopkins APL techinacal Digest, Volume 31, Number 2, 2012
25. ©SunEarthTools.com. 2009-2019. Available from:  
<https://www.sunearthtools.com/it/tools/distance.php#top>

26. D.G. Mazzotta, “*4-Dimensional Lateral-Directional Trajectory Optimization Satisfying Waypoint and No-Fly Zone Constraints*”, Politecnico di Torino, October 2011
27. M. K. Yalcin, Erhan Ersoy, “Designing Autopilot System for Fixed-Wing Flight Mode of a Tilt-Rotor UAV in a Virtual Environment: X-Plane”, in Researchgate.net, Aprile 2018

# Appendices

---